

# **Studies of Neutron-Rich Nuclei Using Deep Inelastic Collisions**

**By**

**Jose Javier Valiente-Dobón**

Doctor of Philosophy

Department of Physics,  
School of Electronics and Physical Sciences,  
University of Surrey.

Supervisor

Dr. P.H. Regan

October 9, 2003

---

## Abstract

A deep inelastic reaction between a thin self-supporting  $^{198}_{78}\text{Pt}$  target and an 850 MeV  $^{136}_{54}\text{Xe}$  beam has been used to populate and study both neutron-rich nuclei around the beam and target masses and the reaction mechanism. An  $I^\pi = 10^+$  isomeric state has been found in the  $N = 80$  isotope  $^{136}_{56}\text{Ba}$  with a measured half-life of  $91 \pm 2\text{ns}$ . The structure of the predominantly  $(\nu h_{\frac{11}{2}})_{10+}^{-2}$  isomer is discussed in terms of shell model and pair-truncated shell model calculations and compared to the even-Z,  $N = 80$  isotones ranging from  $^{130}_{50}\text{Sn}$  to  $^{148}_{68}\text{Er}$ . A qualitative explanation of the observed dramatic decrease in the  $B(E2 : 10^+ \rightarrow 8^+)$  value for the  $N = 80$  isotones at  $^{136}\text{Ba}$  is given in terms of the increasing single-particle energy of the  $h_{\frac{11}{2}}$  neutron configuration as the proton sub-shell is filled. A 4-quasiparticle isomer has been observed in  $^{184}_{74}\text{W}$  with a half-life of  $188 \pm 38\text{ns}$ . The results are compared with blocked BCS Nilsson calculations which favour the  $K^\pi = 15^-$  interpretation. This isomer completes the even-A tungsten, 4-quasiparticle isomer systematics from  $A = 176$  to 186. A high spin isomeric state has been found in the near spherical nucleus  $^{198}\text{Pt}$  with a half-life of  $36 \pm 2\text{ns}$ . The nature of this isomer has been interpreted from an examination of the systematics of platinum isotopes and neighbouring nuclei as a tentative  $I^\pi = 12^+$  state from rotation-aligned, two neutron ( $i_{\frac{13}{2}}^1$ )<sup>2</sup> configuration. Using prompt-delayed  $\gamma$ -ray correlations, the complementary fragments of the reaction have been studied and used to identify new states in  $^{194}_{76}\text{Os}$ . The angular momentum transfer to the binary fragments in the reaction has been investigated in terms of the average total  $\gamma$ -ray fold versus the scattering angle of the recoils.

---

## Acknowledgements

I have realised that the first thing anyone does when they have a thesis in their hands, is to read the acknowledgements. Therefore this section is one of the most important in terms of the number of readers. Thus, I shall try to make the following lines as interesting as possible to encourage people to continue reading the fabulous findings that are described in this thesis.

Firstly, I would like to thank my supervisor Paddy Regan, who has guided me through my PhD studies. The optimistic way in which he faces life has made all the tedious moments that I came across during my thesis much more pleasant. I am very thankful to Carl Wheldon who has helped me with every-day problems while dealing with experimental Nuclear Physics. I am very grateful to Bill Gelletly for his support and interesting conversations about the recent Spanish history. I also want to thank Makito Oi, Phil Walker and Zsolt Podolyák for interesting discussions on Physics. A special thanks goes to Berta Rubio for introducing me to the world of Physics. I would like to thank all my office mates, Tamara Baldwin, Hasna El-Masri, Scott Langdown, Steve Pain, Nicolas Schunck, Scott Williams and Arata Yamamoto, for their help and our long coffee breaks full of nice conversations which made the day more pleasant.

At a more personal level, I would like to thank Alicia Nuez Imbernón, because she is my North, my South, my East and West. I would like to thank my friends from València, Carmen Chorro, Enric Casanova, Héctor Beltran, Juan Vilata, Nadia Torres, Olga Martínez and Sari Zorio, and the Oveja Negra gang, Albor Dobón, Fernando Gil, María Jesus Amblart, Miguel Iserte, Sergio Sotos and Eloy and Diego Rubio, for those great moments that we have shared together. I am very thankful to my second family in England, namely Noelia Rapún, Ana López, Olga Martínez, Jose Rodríguez and Álvaro García that made my stay in England more pleasant and to my second German-Polish family, namely Gosia Sudol, Kasia Tyminska, Przemek Adrich and Gonzalo Rodríguez, among others, that made my stays in

---

Germany memorable. I would like to thank Tobias Neher and Evan Knox-Davies for their friendship and the very nice squash games that we have shared. I am very thankful to Enrique Nácher, mi compañero de fatigas.

I am forever indebted to my mother, my father and my sister for all the support over the years.

Although a thesis would seem an inappropriate place to certain people, I would like to remember the International Brigades and the Spanish people who died fighting for the Second Spanish Republic during the Spanish Civil War (1936-1939) against the rebels. In spite of the effort of many Spanish politicians to make us forget in the past and still nowadays, many of us still believe in democracy. Thus it is always a good moment to remember and not to forget those that lost their lives fighting for a fairer world.

---

*A todo el mundo se le puede hacer, a mano,  
un alma nueva, y se le pueden soplar  
inquietudes en el alma.*

*Federico García Lorca*

# Contents

<b>1</b>	<b>Nuclear Structure and Electromagnetic decays</b>	<b>1</b>
1.1	The Nuclear Shell Model . . . . .	1
1.1.1	Saitama's Shell Model and Pair-Truncated Shell Model . . . . .	4
1.2	Seniority Scheme . . . . .	5
1.3	Deformed Shell Model . . . . .	7
1.3.1	Nilsson Model . . . . .	8
1.4	Blocked BCS Calculations . . . . .	8
1.5	Two-State Mixing . . . . .	10
1.6	Gamma Decay . . . . .	11
1.6.1	Selection Rules . . . . .	11
1.6.2	Electromagnetic Transition Rates . . . . .	12
1.7	Internal Conversion . . . . .	14
1.8	Angular Distribution of $\gamma$ Rays . . . . .	16
<b>2</b>	<b>Experimental Considerations</b>	<b>18</b>
2.1	Nuclear Reactions of Heavy Ions . . . . .	18
2.2	Deep-Inelastic Nuclear Reactions . . . . .	19
2.2.1	Kinematics in Binary Reactions . . . . .	21
2.2.2	Angular Momentum in Binary Reactions . . . . .	22
2.2.3	Grazing Angle in a DIC . . . . .	26
2.2.4	Q-value of a Nuclear Reaction . . . . .	27
2.3	Gamma-Ray Interactions in Matter . . . . .	27

## Contents

---

2.3.1	Suppression of Compton Events . . . . .	31
2.3.2	Probability of Detecting a $\gamma$ Ray . . . . .	32
2.3.3	Deposition of the $\gamma$ -Ray Energy in Germanium . . . . .	33
2.4	General Description of HPGe Detectors . . . . .	34
2.4.1	Gamma-Ray Arrays: GAMMASPHERE . . . . .	36
2.4.2	Doppler Shift and Doppler Broadening Correction . . . . .	37
2.5	Heavy Ion Detector: CHICO . . . . .	40
<b>3</b>	<b>Analysis of the GAMMASPHERE-CHICO Data</b>	<b>43</b>
3.1	Experimental Procedure . . . . .	43
3.1.1	Efficiency of GAMMASPHERE with CHICO . . . . .	45
3.2	Data Reduction and Off-line Analysis . . . . .	46
3.2.1	Particle Identification . . . . .	46
3.2.2	Doppler Correction . . . . .	48
3.2.3	Pseudo Q-value of the Reaction . . . . .	53
3.2.4	Gamma-Ray Fold . . . . .	54
3.2.5	Description of Matrix and Cube Analysis . . . . .	56
<b>4</b>	<b>Results and Discussion</b>	<b>57</b>
4.1	Isomers Populated . . . . .	57
4.2	Isomeric $(\nu h_{\frac{11}{2}})_{10^+}^{-2}$ State in $^{136}_{56}\text{Ba}$ . . . . .	63
4.2.1	Transitions below the $10^+$ isomer in $^{136}\text{Ba}$ . . . . .	65
4.2.2	Transitions above the $10^+$ isomer in $^{136}\text{Ba}$ . . . . .	68
4.2.3	Discussion of $^{136}\text{Ba}$ . . . . .	73
4.3	A Multi-Quasiparticle Isomeric State in $^{184}_{74}\text{W}$ . . . . .	85
4.3.1	Decay Scheme of $^{184}\text{W}$ . . . . .	85
4.3.2	Discussion of $^{184}\text{W}$ . . . . .	90
4.4	Study of $^{198}_{78}\text{Pt}$ . . . . .	96
4.4.1	Prompt $\gamma$ Rays in $^{198}\text{Pt}$ . . . . .	96
4.4.2	Isomeric State in $^{198}\text{Pt}$ . . . . .	99

## Contents

---

4.4.3	Discussion of $^{198}\text{Pt}$	101
4.5	Study of Complementary Fragments	103
4.5.1	$^{196}\text{Os}$ or Not $^{196}\text{Os}$ , That Is the Question	106
4.6	Angular Momentum Transfer Determination	108
<b>5</b>	<b>Conclusions and Future Work</b>	<b>113</b>
<b>A</b>	<b>Gamma-Ray Tracking</b>	<b>126</b>
A.1	6×6 Segmented Germanium Detector	126
A.1.1	Prototype Description	126
A.1.2	Measurement of Resolution and Risetimes	129
A.1.3	Net Charge and Mirror Charge Signals	130
A.1.4	Energy Deposited in an Interaction: Moving Window Deconvolution Method (MWD)	133
A.1.5	MWD Results	135
A.2	Reconstructing the $\gamma$ -Ray Path	136
A.2.1	Introduction	136
A.2.2	Simulation of the Prototype	137
A.2.3	Tracking Algorithm	138
A.2.4	Tracking Algorithm Results	143
<b>B</b>	<b>Publications</b>	<b>148</b>
<b>C</b>	<b>Oral and Poster Presentations</b>	<b>152</b>

# List of Figures

1.1	The schematic structure of the single particle orbitals resulting from the simple, spherical nuclear mean field. Taken from Ref. [3]. . . . .	3
1.2	Behaviour of the $B(E2)$ values along a shell in the seniority scheme in terms of the fractional $j$ -shell filling $f = \frac{n}{(2j+1)}$ . At the middle of a shell $f = 0.5$ . Modified from Ref. [7]. . . . .	7
1.3	Theoretical internal conversion coefficients for $E1$ , $M1$ , $E2$ and $M2$ transitions for atomic numbers $Z = 56$ (left) and $Z = 74$ (right). . . . .	15
2.1	Semiclassical description of a Deep Inelastic Nuclear Reaction between heavy ions. . . . .	20
2.2	Reaction geometry. Projectile and target recoils define the reaction plane of the binary reaction. . . . .	21
2.3	Calculated velocities of the projectile and the target recoils for the particular case of a $^{136}\text{Xe}$ beam at 850 MeV in the laboratory frame impinging on a $^{198}\text{Pt}$ target. An elastic collision and simple two-body kinematics have been assumed. . . . .	22
2.4	Differential cross-section $d\sigma(\theta)/d\Omega$ for the production of secondary photons from Compton scattering. Curves are shown for six different values of primary photon energy ( $\alpha = 1$ , $E_\gamma = 511$ keV). . . . .	30
2.5	Gamma-ray linear attenuation coefficients for Ge as a function of $\gamma$ -ray energy. Taken from Ref. [49] . . . . .	32

---

## List of Figures

---

2.6 Schematic view of a <i>n-type</i> germanium detector with the corresponding charge carriers drift velocities. . . . .	36
2.7 Picture showing a quarter of GAMMASPHERE. . . . .	37
2.8 Ratio of the energy in the laboratory frame ( $E_s$ ) to energy in the rest frame ( $E_0$ ), versus the laboratory angle $\theta$ . . . . .	38
2.9 Contribution to the energy resolution due to the uncertainty in the scattering angle $\theta$ , assuming $\Delta\theta = 10^\circ$ . . . . .	38
2.10 Contribution to the energy resolution due to the uncertainty in the beam velocity, assuming $\Delta\beta = 0.03$ . . . . .	39
2.11 The two contributions to the Doppler broadening ( $\Delta\beta$ and $\Delta\theta$ ) added in quadrature. This plot represents the ultimate energy resolution in an experiment using detectors which have a “perfect” intrinsic energy resolution. . . . .	39
2.12 Sectional view of CHICO within GAMMASPHERE. The target chamber housing the PPACs and the pressure window can be seen. The length of the assembly is 91 cm. . . . .	41
2.13 View of an individual PPAC, taken from [65]. The upper one is the asymmetrically segmented anode and the one below is the cathode board, showing the delay line. . . . .	42
2.14 Segmentation of two coplanar anode pairs. . . . .	42
3.1 Spectrum (a) shows the total time projection of $\gamma$ -ray events in the current work, note that the time between the cyclotron bursts is 178 ns. Spectrum (b) shows the time difference between pairs of $\gamma$ rays ( $t_{\gamma_1} - t_{\gamma_2}$ ). . . . .	44
3.2 Relative efficiency curve for GAMMASPHERE with CHICO. The experimental points correspond to $^{152}\text{Eu}$ and $^{133}\text{Ba}$ sources. . . . .	45
3.3 Particle identification plot for the current work. The measurement of the $\Delta\text{TOF}$ and scattering angles of the recoils $\theta$ allows the two binary partners to be cleanly separated. . . . .	47

---

List of Figures

---

3.4 Angular correlation between the two scattered fragments BLFs and TLFs as measured in CHICO for the reaction of a $^{136}\text{Xe}$ beam at 850 MeV on a $^{198}\text{Pt}$ target. . . . .	48
3.5 Two dimensional plot of $\gamma$ -ray energy versus time relative to the master trigger. The various vertical stripes are the beam pulses, separated by 178 ns. The plot clearly shows the presence of a number of isomeric states (horizontal lines). . . . .	49
3.6 Schematic view of the angles in spherical coordinates that define the vector position of the recoils and $\gamma$ rays. It shows the angles involved in the Doppler correction. . . . .	50
3.7 Spectrum (a) shows prompt $\gamma$ rays without any Doppler correction, spectra (b) and (c) show the total projection of prompt Doppler corrected spectra for BLFs and TLFs respectively. The two lower spectra show delayed spectra for two different time ranges. (d) shows delayed $\gamma$ rays emitted within the time range 200 ns to 780 ns, while (e) shows $\gamma$ rays emitted within the first 200 ns following the CHICO fragments detection. The peaks marked with a + symbol are $^{136}\text{Ba}$ $\gamma$ rays which feed into the $10^+$ isomer. . . . .	51
3.8 Pseudo Q-value versus $\theta$ gated for BLFs (upper spectrum) and for TLFs (lower spectrum), for the reaction 850 MeV $^{136}\text{Xe}$ beam, $^{198}\text{Pt}$ target. . . . .	54
3.9 Total Fold measured in the reaction (top), lower panels show the different contributions. Note that the total fold ( $F_{tot}$ ) shown in the upper panel is not the direct sum of the three lower panels but the addition of the three contributions ( $F_{BGO}$ , $F_{HPGe}$ , $F_{CS}$ ) event by event (see text). . . . .	55

## List of Figures

---

4.1 Summary of isomers identified in the reaction (850 MeV $^{136}\text{Xe}$ beam, $^{198}\text{Pt}$ target). The $N/Z$ equilibration line has been plotted for both BLFs and TLFs. Note that the isomers marked in magenta (colour code), are newly observed isomers. . . . .	58
4.2 Background subtracted $\gamma$ -ray spectra for selected isomeric states in BLFs populated in the reaction $^{136}\text{Xe}$ beam at 850 MeV impinging on a $^{198}\text{Pt}$ target. The insets show the fitted half-life curves obtained in this work and the pairs of double $\gamma$ -ray gates used to obtain the half-life curve are given in braces. The isomers identified in $^{131}\text{I}$ and $^{133}\text{I}$ have not previously been reported. . . . .	60
4.3 Background subtracted $\gamma$ -ray spectra for selected isomeric states in TLFs populated in the reaction $^{136}\text{Xe}$ beam at 850 MeV impinging on a $^{198}\text{Pt}$ target. The insets show the fitted half-life curves obtained in this work and the pairs of double $\gamma$ -ray gates used to obtain the half-life curve are given in braces. The isomers identified in $^{184}\text{W}$ , $^{191}\text{Os}$ , $^{192}\text{Os}$ and $^{198}\text{Pt}$ have not previously been reported. . . . .	61
4.4 Background subtracted $\gamma$ -ray spectra for selected isomeric states in BLFs populated in this reaction. A limit on the half-life has been obtained for each of the reported isomers. . . . .	62
4.5 Background subtracted $\gamma$ -ray spectra for selected isomeric states in TLFs populated in this reaction. A limit on the half-life has been obtained for each of the reported isomers. . . . .	62
4.6 Gamma-ray decay curves for the isomers identified in $^{139}\text{La}$ (upper) and $^{190}\text{Os}$ (lower). Due to experimental constraints precise values for the half-lives could not be obtained but limits of $t_{1/2} > 1 \mu\text{s}$ and $t_{1/2} < 110 \text{ ns}$ respectively have been estimated. . . . .	63

4.7 Level scheme of $^{136}\text{Ba}$ deduced from the present work with the $91 \pm 2$ ns $I^\pi = 10^+$ isomer. The widths of the arrows are proportional to the relative $\gamma$ -ray intensities. Note that all the energies are given in keV. . . . .	64
4.8 Background subtracted delayed $\gamma$ -ray spectra from the decay of the $I^\pi = 10^+$ isomer in $^{136}\text{Ba}$ . The time condition is that the $\gamma$ rays are observed in the time range $\Delta t = 100\text{-}600$ ns with respect to the master trigger. . . . .	66
4.9 Time difference $\gamma - \gamma$ spectrum obtained by gating above and below the isomeric $10^+$ state to determine the half-life of the $10^+$ state in $^{136}\text{Ba}$ ( $91 \pm 2$ ns). . . . .	67
4.10 Upper spectrum (a) shows the background subtracted delayed $\gamma$ -ray spectra gated by prompt transitions above the proposed $10^+$ isomer in $^{136}\text{Ba}$ . Lower spectrum (b) shows the background subtracted prompt $\gamma$ -ray spectra gated by delayed transitions placed below the proposed $10^+$ isomer. . . . .	68
4.11 Background subtracted prompt $\gamma$ -ray spectra single-gated by the delayed 341, 363, 787, 819, 1048, 1235 keV transitions placed below the $10^+$ isomer in $^{136}\text{Ba}$ . The time condition is that the prompt $\gamma$ rays are observed within $\Delta t = \pm 45$ ns of the master trigger. . . . .	70
4.12 Gamma-ray angular distributions. The top-left panel shows angular distributions for known transitions, $^{198}\text{Pt}$ ( $4^+ \rightarrow 2^+$ ) ( $E2$ transition) and $^{138}\text{Ba}$ ( $9^- \rightarrow 8^+$ ) ( $E1$ transition), the other panels show the angular distributions for the $\gamma$ rays above the $10^+$ isomer in $^{136}\text{Ba}$ . . . . .	72

---

## List of Figures

---

4.13 Comparison of the experimental energy spectra (left panel) with the results of the shell-model calculation (middle panel) and the pair-truncated shell-model calculations (right panel) for $^{136}\text{Ba}$ (see text for details). Note that in the middle and right panel the states are separated into columns for the yrast states up to $10^+$ , the positive-parity states and the negative-parity states. . . . .	75
4.14 The upper panel shows the expectation numbers of neutron $D_\nu$ and $G_\nu$ pairs, the middle panel shows the expectation numbers of proton $D_\pi$ and $G_\pi$ pairs calculated in the PTSM. The lower panel shows the expectation numbers of neutron and proton $H_{\nu,\pi}$ pairs calculated in the PTSM. The expectation numbers are for the positive yrast states. . . . .	76
4.15 Energy systematics for the $N = 80$ isotones. The predominantly $(\nu h_{\frac{11}{2}})^{-2}$ or $(\pi h_{\frac{11}{2}})^2$ configuration character of the $10^+$ state is indicated for each isotope. . . . .	80
4.16 Upper panel ( <i>a</i> ) shows the energies of the $I^\pi = \frac{11}{2}^-$ single-particle states for the $N = 81$ isotones, taken from [66]. Panels ( <i>b</i> ) and ( <i>c</i> ) show the excitation energy of the $I^\pi = 10^+$ isomer and the $B(E2 : 10^+ \rightarrow 8^+)$ transitions rates for the $N = 80$ isotones respectively, taken from [84, 85, 87]. . . . .	81
4.17 The left panel shows the energy systematics for the yrast $2^+, 4^+, 6^+, 8^+, 10^+$ states in the tin isotopes, from $^{116}\text{Sn}$ to $^{130}\text{Sn}$ . The right panel shows the $B(E2)$ value systematics with the filling of the $h_{\frac{11}{2}}$ orbital for the $10^+ \rightarrow 8^+$ transition. . . . .	82
4.18 The left panel shows the energy systematics for the yrast $2^+, 4^+, 6^+, 8^+, 10^+$ states in the barium isotopes, from $^{126}\text{Ba}$ to $^{138}\text{Ba}$ . The right panel shows the $B(E2)$ value systematics with the filling of the $h_{\frac{11}{2}}$ orbital for the $10^+ \rightarrow 8^+$ transition. . . . .	83

4.19 Comparison of the experimental $B(E2)$ values (solid line) for barium isotopes filling the $h_{\frac{11}{2}}$ shell with the theoretical $B(E2)$ values obtained in the seniority scheme framework, for transitions that connect states with $\Delta\nu = \pm 2$ (dashed-dotted line) and for transitions that do not change seniority (dashed line). . . . .	84
4.20 Partial level scheme for $^{184}_{74}\text{W}_{110}$ showing the newly observed 4-quasiparticle isomer at $E_x = 3862$ keV (this work) together with the previously known 2-quasiparticle isomer at 1285 keV [115, 116]. It is also shown two $10^+$ levels at 1816 and 2471 keV from which non decay has been observed in the current work [66]. The widths of the arrows are proportional to the relative $\gamma$ -ray intensity (black) and electron conversion intensity (white) except for the tentative transitions (dashed arrows). Preferred tentative spin and parity assignments are given in parentheses, though there are typically several other possible labels for each of these levels (see text). . . . .	86
4.21 Gamma-ray coincidence spectrum gated by the delayed 253 keV transition in the ground-state band of $^{184}\text{W}$ . The transitions labelled only by energy are assigned to $^{184}\text{W}$ . Known contaminants in coincidence with the 253 keV are indicated and those which are unknown are labelled by ‘c’. Intense X-rays from the platinum target are due to ‘time-walk’ into the delayed spectra. X-rays from the cerium binary partner nuclei are due to coincident isomeric decays and/or timewalk. . . . .	87
4.22 Time spectrum showing the $188 \pm 38$ ns half-life and an exponential fit to the data (solid line) for the 3862 keV isomer in $^{184}\text{W}$ . It has been obtained from pairs of double $\gamma$ -ray gates. . . . .	88

---

## List of Figures

4.23 Tungsten low-lying 4-quasiparticle isomer systematics for $A = 176 \rightarrow 190$ . Filled circles represent experimental energies, and the dotted line denotes the corresponding energies from the blocked BCS calculations (see text for details). A rigid rotor reference energy (appropriate for the deformation) has been subtracted in all cases. For $^{184}\text{W}$ both the data and calculation cover 2 scenarios for $K = 15$ and $K = 17$ . Measured half-lives are quoted for all of the experimentally observed states. . . . .	95
4.24 Level scheme of $^{198}\text{Pt}$ , obtained by looking at prompt $\gamma - \gamma$ coincidences, including the previously unreported 813 and 802 keV transitions. The widths of the arrows are proportional to the observed relative $\gamma$ -ray intensity (black) and the electron conversion intensity (white). . . . .	96
4.25 Background subtracted prompt $\gamma$ -ray spectra for $^{198}\text{Pt}$ . These spectra are software gated with a condition on the time range $\Delta t = \pm 45\text{ns}$ with respect to the detection of the recoils. . . . .	97
4.26 Background subtracted delayed $\gamma$ -ray spectra for $^{198}\text{Pt}$ . The time condition is that the $\gamma$ rays are observed in the time range $\Delta t = 30 - 150\text{ ns}$ with respect to the detection of the two binary fragments. . . . .	99
4.27 Level scheme of $^{196}\text{Pt}$ (left). Level scheme of $^{198}\text{Pt}$ (middle), obtained from delayed $\gamma - \gamma$ coincidences. It shows the $36 \pm 2\text{ ns}$ isomer. The widths of the arrows are proportional to the relative $\gamma$ -ray intensity. Level scheme of $^{200}\text{Pt}$ (right), taken from [139]. . . . .	100
4.28 Gamma-ray decay curve used to determine the half-life of the ( $I^\pi = 12^+$ ) isomeric state in $^{198}\text{Pt}$ ( $t_{1/2} = 36 \pm 2\text{ ns}$ ), gated by pairs of double $\gamma$ -ray gates. . . . .	101

---

## List of Figures

4.29 Background subtracted prompt $\gamma$ -ray spectra for osmium isotopes, gated on delayed barium $\gamma$ rays. The upper panel is gated by $^{138}\text{Ba}$ delayed $\gamma$ rays, whose binary partner is $^{196}\text{Os}$ and the lower panel is gated by $^{136}\text{Ba}$ delayed $\gamma$ rays, whose binary partner is $^{198}\text{Os}$ . . . . .	103
4.30 Background subtracted prompt $\gamma$ -ray spectra for platinum isotopes, gated by delayed xenon $\gamma$ rays. The upper panel is gated by $^{136}\text{Xe}$ delayed $\gamma$ rays, whose binary partner is $^{198}\text{Pt}$ . The middle panel is gated by $^{134}\text{Xe}$ delayed $\gamma$ rays, whose binary partner is $^{200}\text{Pt}$ and the lower panel is gated by $^{133}\text{Xe}$ delayed $\gamma$ rays, whose binary partner is $^{201}\text{Pt}$ . Note that xenon and platinum are binary partners. . . . .	104
4.31 Relative Yield for osmium isotopes. The upper panel shows the Relative Yield for osmium isotopes gated by $^{138}\text{Ba}$ , whose binary partner is $^{196}\text{Os}$ which is unknown. The lower panel shows the Relative Yield for osmium isotopes gated on $^{136}\text{Ba}$ , whose binary partner is $^{198}\text{Os}$ . . . . .	105
4.32 Level scheme of $^{196}\text{Os}$ , taken from [144] (left) and level scheme for $^{194}\text{Os}$ , taken from [145], including the new 283 keV transition deduced from the present work (right). . . . . . . . . . .	106
4.33 Background subtracted prompt $\gamma$ -ray spectra for $^{194}\text{Os}$ . These spectra have been obtained by looking at $\gamma$ - $\gamma$ prompt coincidences. The $\gamma$ - $\gamma$ prompt matrix has been gated on the delayed 192, 463 and 1436 keV $\gamma$ rays from the binary partner $^{138}\text{Ba}$ . . . . . . . . . . .	107
4.34 Fold distribution for different $\gamma$ -ray transitions for the target nucleus, $^{198}\text{Pt}$ . Low fold events clearly dominate, corresponding to Coulomb scattering. For the $8^+ \rightarrow 6^+$ transition some events of higher fold start appearing, corresponding to some population from more inelastic processes. . . . . . . . . . .	109

---

## List of Figures

4.35 Average fold distribution versus laboratory scattering recoil angle $\theta$ for the beam $^{136}\text{Xe}$ (left) and the target $^{198}\text{Pt}$ (right) nuclei. In the lower (a), (b), (c) spectra fold projections for various angular ranges is shown. These plots were made by gating on the delayed $\gamma$ rays 1313 keV and 407 keV to select $^{136}\text{Xe}$ and $^{198}\text{Pt}$ respectively. Note that the estimated grazing angle of the reaction lies around 50°.	110
4.36 Average fold distribution versus laboratory scattering recoil angle $\theta$ for $^{136}\text{Ba}$ (top-left), $^{138}\text{Ba}$ (top-right), $^{125}\text{Sb}$ (bottom-left), $^{138}\text{Ce}$ (bottom-right). In the lower (a), (b), (c) spectra a fold cut for various angular ranges is shown. These plots have been made gating on the delayed $\gamma$ rays 819 keV, 1436 keV, 904 keV and (815, 980) keV to select $^{136}\text{Ba}$ , $^{138}\text{Ba}$ , $^{125}\text{Sb}$ and $^{138}\text{Ce}$ respectively. The number of minimum nucleons transfer to produce these nuclei in the reaction are: (+2p, +2n) onto the beam for $^{136}\text{Ba}$ , (+2p) onto the beam for $^{138}\text{Ba}$ , (-3p, -8n) from the beam for $^{125}\text{Sb}$ and (+4p, -2n) from the beam for $^{138}\text{Ce}$ .	111
A.1 EURISYS measures ( <i>EGC 60-90 SEG36</i> ) prototype.	127
A.2 Schematic view of the segmented germanium crystal. The letters label the different disk sections and the numbers label the longitudinal sections.	127
A.3 Diagram of the electronics used for pulse processing, module <i>cM62</i> and <i>AD40</i>	128
A.4 Energy resolution for all the segments in the EURISYS $6 \times 6$ prototype. The full black points show the FWHM at 122 keV, the open points show the FWHM at 1332 keV. Note, the data points for segment C3 are missing due to problems with the preamplifier.	129
A.5 Risetime distributions for the front slide (slide 1) and the slide 3, for 1332 keV $\gamma$ -rays.	130

---

## List of Figures

---

A.6 Digitised signals for an event in segment E3 and a negative mirror charge in segment D3. . . . .	131
A.7 Digitised signals for an event in segment E3 and a positive mirror charge in segment F3. . . . .	132
A.8 Pulse signal from segment D3 with energy deposition by a $\gamma$ -ray and the neighbouring image charge, segment E3. The deconvoluted calculated signals according to Equations (A.5) and (A.6) are shown on the right-hand side. . . . .	135
A.9 Performance of the Moving Window Deconvolution MWD method for $^{60}\text{Co}$ and $^{152}\text{Eu}$ sources for segment B1 (front edge). . . . .	136
A.10 Performance of an exponential fitting of the digitised signal for $^{60}\text{Co}$ and $^{152}\text{Eu}$ sources for segment B1 (front edge). . . . .	137
A.11 Simulated spectra for a $^{60}\text{Co}$ source (upper panel), detail of the Compton background (lower panel). . . . .	138
A.12 For different position resolutions are shown the fraction of events which are not distinguishable, for more than one interaction in a segment (lower panel), more than two interactions (middle panel) or more than three interactions (upper panel). The 20 mm position resolution corresponds to the whole segment. Data obtained using EGS4 Monte Carlo simulations. . . . .	139
A.13 Range and total track length of the electrons produced in the interaction of a $\gamma$ ray in germanium. Data obtained using EGS4 Monte Carlo simulations. . . . .	140
A.14 Schematic representation of $\Theta_1^{\min}$ and $\Theta_1^{\max}$ , calculated numerically by the tracking algorithm for the first point of the $\gamma$ -ray interaction. The different interaction points have an uncertainty that has been represented by spheres. The source is indicated outside of the detector.	141

## List of Figures

---

A.15 Compton suppression performance of the tracking algorithm for a simulated $^{60}\text{Co}$ source, for a position resolution of 5 mm (upper panel) and for a position resolution of 20 mm (lower panel). . . . .	143
A.16 Doppler correction performance of the tracking algorithm for a simulated $^{60}\text{Co}$ source. . . . .	144
A.17 Photopeak efficiency and Peak-to-Total for different energies as a result of tracking. . . . .	146
A.18 Experimental Compton suppression performance of the tracking algorithm for source data, using a $^{60}\text{Co}$ source at a distance of 25 cm to the front edge. . . . .	147

# List of Tables

1.1	Electromagnetic transition rates. The units are: $T(\sigma L) - s^{-1}$ , $B(EL)$ – $e^2 fm^{2L}$ , $B(ML) - \mu_n^2 fm^{2L-2}$ when the $\gamma$ -ray energy $E$ is expressed in MeV. Taken from [20]. . . . .	13
1.2	Single particle or Weisskopf estimates. The units are $s^{-1}$ when the $\gamma$ -ray energy $E$ is expressed in MeV and $A$ is the atomic mass number. Taken from [18]. . . . .	14
3.1	Polar angle $\theta$ for the different rings of the $\gamma$ -array GAMMASPHERE and the number of working detectors in each ring. . . . .	52
3.2	List of the different matrices and cubes used in the analysis of the present work. . . . .	56
4.1	Half-lives of the isomers measured in the present work and a comparison with previous works. . . . .	59
4.2	Energies, assignments and relative out-of-beam intensities, for transitions observed in $^{136}_{56}\text{Ba}$ . The uncertainties in the transition energies are $\pm 0.2$ keV. . . . .	69
4.3	Energies, relative in-beam intensities and $A_2$ coefficients for transitions observed in $^{136}_{56}\text{Ba}$ above the $10^+$ isomer. The energy resolution for prompt $\gamma$ rays is approximately 1%. . . . .	71
4.4	The expectation numbers of $D$ , $G$ and $H$ pairs calculated in the PTSM for the yrast $8_1^+$ state and the second $8_2^+$ state. . . . .	77

## List of Tables

---

4.5 Comparison of the yrast $B(E2)$ values in the shell model (SM) with the measured values in $e^2\text{fm}^4$ . The experimental values have been taken from [103, 104] and the present work. . . . .	78
4.6 Weisskopf single-particle estimates for a 148 keV transition in $^{184}\text{W}$ . The relevant electron conversion coefficients [22] ( $\alpha_T$ ) are quoted together with the corresponding partial $\gamma$ -ray half-life. . . . .	89
4.7 Energy systematics in the $A \approx 184$ region for 2- and 4-quasiparticle states. Energies in brackets indicate tentative assignments. Where multiple states of the same spin and parity are known the energy of the lowest lying state is quoted. . . . .	91
4.8 Low-lying 2- and 4-quasiparticle states in $^{184}\text{W}$ . The calculated energy from the blocked BCS calculations is $E_{qp}$ (see text for details), $E_{res}$ is the residual nucleon-nucleon interaction energy [132] and $E_{calc} = E_{qp} + E_{res}$ is directly comparable with the experimentally determined energies. Experimental energies quoted in parentheses are states observed in the current work for which the spins and parities are uncertain. All other values of $E_{expt}$ are from Ref.[66]. A ‘-’ sign in front of a $\frac{1}{2}^-$ [510] orbital indicates a configuration with a less than maximal $K$ coupling. . . . .	92
4.9 Energies, assignments and relative in-beam intensities, for the transitions observed in $^{198}\text{Pt}$ . The FWHM of the Doppler corected transition energies is approximately 1%. . . . .	98
4.10 Energies, assignments and relative out-of-beam intensities, for the transitions observed in $^{198}\text{Pt}$ . The uncertainties in the transition energies are $\pm 0.2$ keV. . . . .	102
A.1 Summary of the results from simulated data for 5mm and 20mm resolution. . . . .	145

List of Tables

A.2 Summary of the results from experimental source data for 20mm resolution. Doppler correction is missing, since non in beam experiment has been performed. . . . .	147
---	-----

# Chapter 1

## Nuclear Structure and Electromagnetic decays

### 1.1 The Nuclear Shell Model

The study of nuclear properties shows evidence of nuclear shells analogous to those observed in the atoms. One clear piece of evidence in the nuclear case is the sharp discontinuity in nucleon separation energies for certain numbers of  $N$  (neutron number) and  $Z$  (proton number), known as magic numbers. In the case of the electronic shells in atoms the picture is very clear, since there is a central Coulomb potential, due to the charge carried by the nucleus and electrons. In the case of the nucleus there is no such external potential but the nucleons move in the potential created by themselves. This potential contains many terms: central, spin-orbit, tensor, spin-spin, *etc.* At long distances it has a Yukawa form [1], while at short distances it shows an extremely repulsive core. The idea of a shell model for the nucleus may seem contradictory with these strong correlations because this rudely breaks the independent particle picture.

We shall consider the nucleus as composed of  $Z$  protons and  $N$  neutrons, that interact via two-body forces and obey the Schrödinger equation, the general time

independent form of which is [1],

$$\left( -\frac{\hbar^2}{2m} \nabla^2 + V \right) |\Psi\rangle = E |\Psi\rangle \quad (1.1)$$

where  $V$  is the potential and  $|\Psi\rangle$  is the wave function with an associated energy  $E$ .

The experimental idea of magic numbers led M. Goeppert-Mayer and H. Jensen [2] to the construction of the nuclear mean field, a harmonic oscillator, whose main novelty was the very strong spin-orbit splitting needed to explain the experimental magic numbers. This idea originates from atomic physics in which the magnetic moment of an electron interacts with a magnetic field generated by its motion around the nucleus.

$$V(r) = \frac{1}{2}m\omega^2r^2 + D\mathbf{l}^2 - C\mathbf{l}\cdot\mathbf{s} \quad (1.2)$$

where  $\frac{1}{2}m\omega^2r^2$  is the kinetic energy of an harmonic oscillator with frequency  $\omega$  and mass  $m$ ,  $\mathbf{l}$  is the orbital angular momentum operator,  $\mathbf{s}$  is the spin operator,  $D$  and  $C$  are constants to fit and where,

$$\begin{aligned} \mathbf{l}\cdot\mathbf{s} &= -\frac{1}{2}(\mathbf{j}^2 - \mathbf{l}^2 - \mathbf{s}^2) = -\frac{1}{2}(j(j+1) - l(l+1) - \frac{3}{4}) \\ &= l+1 \quad \text{for} \quad j = l - \frac{1}{2} \\ &= -l \quad \text{for} \quad j = l + \frac{1}{2} \end{aligned} \quad (1.3)$$

The single-particle levels of the nuclear mean field are represented in Fig. 1.1. The left-hand side shows the shell structure of the isotropic harmonic oscillator, then the splitting due to the  $\mathbf{l}^2$  term and finally the single-particle levels taking into account the spin-orbit splitting. To the right are the predicted magic numbers. Therefore, due to the  $\mathbf{l}\cdot\mathbf{s}$  term in the potential, the total degeneracy becomes  $(2j+1)$ . This means that, for example, a  $1p$  level, with a total degeneracy of  $2(2l+1) = 6$ , will split into two levels according to Equation 1.3,  $1p_{1/2}$  and  $1p_{3/2}$  with degeneracies 2 and 4 respectively, see Fig. 1.1.

For a given nucleus ( $N, Z$ ) the mean field dictates which levels are occupied (those below the Fermi level) and which are empty (those above). However, these

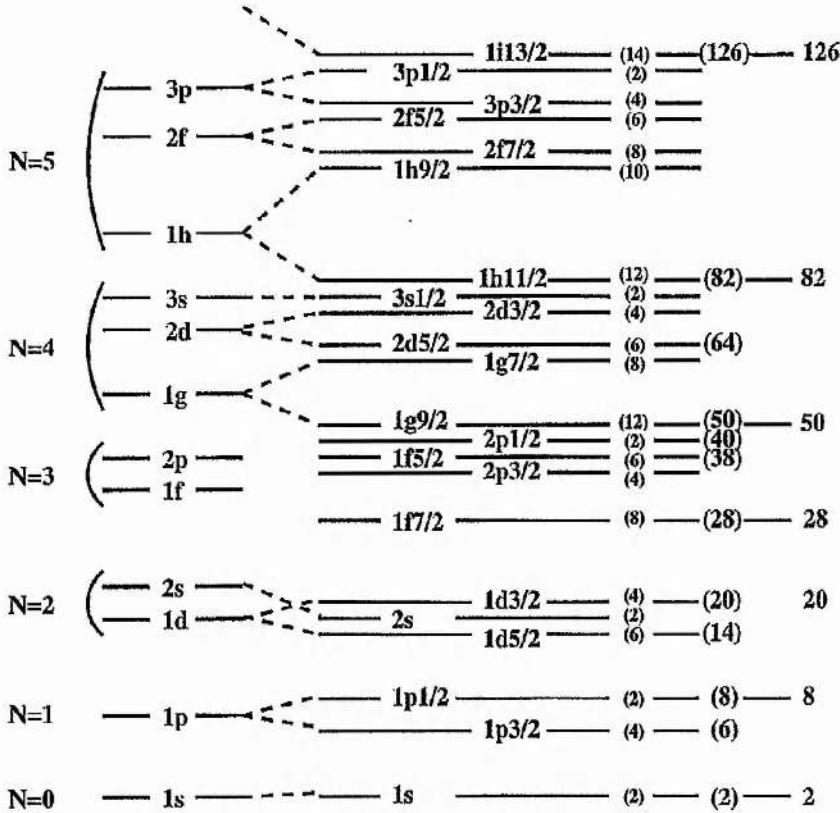


Figure 1.1: The schematic structure of the single particle orbitals resulting from the simple, spherical nuclear mean field. Taken from Ref. [3].

states can be close enough in energy or have a structure such that the residual two-body interaction can mix them to produce correlated states. Therefore, the infinite set of mean-field orbits will be divided in three parts:

- i) Inert core: the orbits that are forced to be always full. Imagine that the core consists of  $N_c$  neutrons and  $Z_c$  protons, thus if we are studying a nucleus  $(N, Z)$  there will remain  $n_v = N - N_c$  valence neutrons and  $z_v = Z - Z_c$  valence protons.
- ii) Valence space: the orbits available to the valence particles, that will be partially occupied by them according to the effective interaction.
- iii) External space: the remaining orbits that are always empty.

### 1.1.1 Saitama's Shell Model and Pair-Truncated Shell Model

This section focuses on the description of an effective shell model developed by the Saitama group (see Higashiyama *et al.* [4]). In a shell model calculation it is necessary to include all the relevant orbits to describe a nucleus, but since this is not always feasible for medium-heavy nuclei, various truncation schemes are commonly used. To determine which orbitals should be included and make feasible the calculations, physical arguments are considered. The principal case of study of this thesis in terms of the shell model is  $^{136}_{56}\text{Ba}_{80}$  and the following considerations will be made for this nucleus. To truncate the model space, the proton single-particle orbitals involved in the calculations are restricted to the three orbitals,  $0g_{\frac{7}{2}}$ ,  $1d_{\frac{5}{2}}$  and  $0h_{\frac{11}{2}}$ . The neutron single-particle orbitals include all of the five orbitals between the  $N = 50$  and 82 shell, *i.e.* the  $1d_{\frac{3}{2}}$ ,  $0h_{\frac{11}{2}}$ ,  $2s_{\frac{1}{2}}$ ,  $1d_{\frac{5}{2}}$  and  $0g_{\frac{7}{2}}$ . The single-particle energies are extracted from experiment.

The effective shell-model hamiltonian is written as,

$$H = H_\nu + H_\pi + H_{\nu\pi}, \quad (1.4)$$

where  $H_\nu$ ,  $H_\pi$ , and  $H_{\nu\pi}$  represent the neutron interaction, the proton interaction and the neutron-proton interaction respectively. The interaction among like nucleons  $H_\tau$  ( $\tau = \nu$  or  $\pi$ ) consists of spherical single-particle energies, a monopole-pairing interaction ( $MP$ ), a quadrupole-pairing interaction ( $QP$ ), a quadrupole-quadrupole interaction ( $QQ$ ), a hexadecapole-pairing ( $HP$ ) and a hexadecapole-hexadecapole ( $HH$ ) interaction. The strengths of these interactions are determined so as to reproduce the corresponding experimental energies of single-closed-shell nuclei. A detailed description of these interactions can be found in Ref. [4]. The definitions of the  $HP$  and  $HH$  interactions are extensions of the  $QP$  and the  $QQ$  interactions from angular momentum coupling two to four, but no radial dependence is assumed. The transition rates between levels are studied using the resultant shell-model wavefunctions.

To study the basic structure of the levels in  $^{136}\text{Ba}$  and to keep the basis to

a reasonable truncation, the pair-truncated shell model (PTSM) approach, which is described in Ref. [5], has also been used. This approach is very similar to the interacting boson model (IBM) [6, 7] in concept, but the bosons are now replaced by correlated nucleon pairs to treat Pauli effects explicitly. In addition to the  $S: J = 0$  pairs, the truncated valence space only allows pair excitations of the following type,  $D: J = 2$ ,  $G: J = 4$  and  $H$ . Note that the calculation is limited to a single  $H$  pair that can only be formed by the coupling of two  $h_{\frac{11}{2}}$  proton particles or neutron holes to angular momentum  $J = 0, 2, 4, 6, 8, 10$ . In contrast, the other pairs in this model space are collective and can be made from linear combinations of other angular momentum couplings between pairs of nucleons in different single-particle orbitals. All these pairs have positive parity so that only positive parity states are predicted. The PTSM model allows the study of the structure of the levels in terms of the expectation number of pairs (see later).

## 1.2 Seniority Scheme

In the previous sections a shell model has been described, which in most of the cases is able to describe quite accurately the nuclear states and the electromagnetic transitions between them. In this section the purpose is to introduce a new tool to look primarily at electromagnetic transitions using the so called *seniority scheme*. An interesting discussion on the transition from the seniority regime to collective motion can be found in Ref. [8]. Seniority,  $\nu$ , is the number of unpaired particles in a state of angular momentum  $\mathbf{J}$ . Therefore, in a multi-particle configuration  $|j^\nu \mathbf{J}\rangle$ , where  $j$  is the total angular momentum of the state where the particles are lying, there are  $\nu$  unpaired particles which are coupled to a total angular momentum  $\mathbf{J}$ . In a configuration  $|j^{\nu+2} \mathbf{J}\rangle$ , a state of the same spin coupling  $\mathbf{J}$ , can be made by coupling a pair of particles to  $\mathbf{J}=0$ , this state has the same seniority as the former one. In a configuration  $|j^n \mathbf{J}\rangle$ , where  $n$  is the number of valence particles, the number of paired particles is  $(n - \nu)$ . In the case of  $\nu = 0$ , all particles are paired and  $\mathbf{J}=0$ .

In a  $j^n$  configuration the maximum angular momentum that can be created is given by [7]

$$J^{max} = nj - \frac{n(n-1)}{2} \quad (1.5)$$

Therefore in a configuration of  $j = (11/2)^2$  the maximum angular momentum that can be created is  $J^{max} = 10$ , since the Pauli principle does not allow two identical fermions with the same quantum numbers.

It is not within the compass of this thesis to give a rigorous analysis of the matrix elements for a general  $j^n$  configuration. This treatment can be found in Ref. [9]. This section will focus on the discussion of quadrupole ( $E2$ ) transitions in the nucleus induced by the even-tensor quadrupole operator  $\mathbf{Q} = r^2 Y_2$ . For an even-tensor operator the seniority is not necessarily conserved and it can connect states with  $\Delta\nu = \pm 2$ . The behaviour of the transition rates throughout a shell for the quadrupole operator is given by [7],

$$\begin{aligned} \left\langle j^n, \nu, \alpha, \mathbf{J} \middle\| \mathbf{Q} \middle\| j^n, \nu - 2, \alpha', \mathbf{J}' \right\rangle^2 &= \left( \frac{(n-\nu+2)(2j+3-n-\nu)}{2(2j+3-2\nu)} \right) \\ &\times \left\langle j^\nu, \nu, \alpha, \mathbf{J} \middle\| \mathbf{Q} \middle\| j^\nu, \nu - 2, \alpha', \mathbf{J}' \right\rangle^2 \end{aligned} \quad (1.6)$$

where  $\alpha$  and  $\alpha'$  denote any additional quantum numbers needed. An interesting result is the reduction of the matrix element in the  $j^n$  configuration to one in  $j^\nu$  and the independence on  $n$ . So the seniority scheme allows the connection of matrix elements in the configuration  $j^n$  to those in the configuration  $j^\nu$ .

For transitions that do not change seniority, the transition rates are given by [7],

$$\left\langle j^n \nu \alpha \mathbf{J} \middle\| \mathbf{Q} \middle\| j^n \nu \alpha' \mathbf{J}' \right\rangle^2 = \left( \frac{(2j+1-2n)}{(2j+1-2\nu)} \right)^2 \times \left\langle j^\nu \nu \alpha \mathbf{J} \middle\| \mathbf{Q} \middle\| j^\nu \nu \alpha' \mathbf{J}' \right\rangle^2. \quad (1.7)$$

Figure 1.2 shows the behaviour of the  $B(E2 : J_i \rightarrow J_f) = \frac{1}{2J_i+1} \langle J_f || \mathbf{Q} || J_i \rangle^2$  values across a shell in the seniority scheme. The results are shown in terms of the so called fractional  $j$ -shell filling  $f = \frac{n}{(2j+1)}$ .

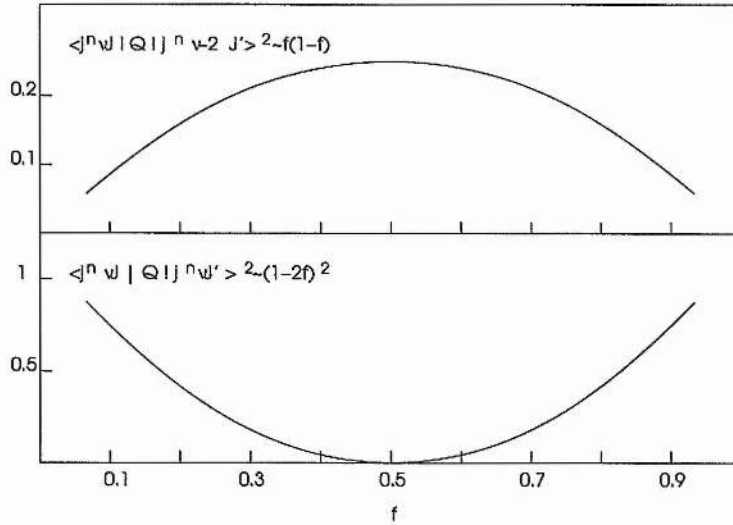


Figure 1.2: Behaviour of the  $B(E2)$  values along a shell in the seniority scheme in terms of the fractional  $j$ -shell filling  $f = \frac{n}{(2j+1)}$ . At the middle of a shell  $f = 0.5$ . Modified from Ref. [7].

### 1.3 Deformed Shell Model

The spherical shell model does not describe well those nuclei far from closed shells. For these regions a deformed potential has to be assumed. The assumption of a deformation is able to explain some experimental facts such as rotational bands and very large quadrupole moments.

The nuclear surface of a non-spherical nucleus can be mathematically described by [10]

$$R(\theta, \phi) = R_0 \left( 1 + \sum_{\lambda=2}^{\infty} \sum_{\mu=-\lambda}^{\lambda} \alpha_{\lambda\mu} Y_{\lambda\mu}(\theta, \phi) \right) \quad (1.8)$$

where  $\alpha_{\lambda\mu}$  are the coefficients of the spherical harmonics  $Y_{\lambda\mu}(\theta, \phi)$ . The terms with  $\lambda = 1$  are not included since they correspond to a translation of the centre of mass.  $R_0$  is the average radius. For axially symmetric nuclei (independent of  $\phi$ ) the radius is defined,

$$R(\theta) = R_0 (1 + \beta_2 Y_{20}(\theta)) \quad (1.9)$$

where the deformation parameter  $\beta_2 = \alpha_{20}$ . If  $\beta_2 < 0$  the nuclear shape is called

*oblate* (“spaceship” shaped), if  $\beta_2 > 0$  the nuclear shape is called *prolate* (“cigar” shaped), if  $\beta_2 = 0$  then the nucleus is spherical. The larger the value of  $\beta_2$ , the more deformed the nucleus.

The nuclei can be axially asymmetric ( $\lambda = 2$ ), in this case a new deformation parameter  $\gamma$  enters into the description of the nuclear shape, where the  $\gamma$  deformation is related to the  $\alpha_{\lambda\mu}$  coefficients as follows [10],

$$\begin{aligned}\alpha_{20} &= \beta_2 \cos \gamma \\ \alpha_{22} &= \alpha_{2-2} = \frac{1}{\sqrt{2}} \beta_2 \sin \gamma\end{aligned}\tag{1.10}$$

The  $\gamma$  deformation goes from  $0^\circ$  to  $60^\circ$  corresponding to prolate and oblate shapes respectively. A completely triaxial nucleus has a  $\gamma = 30^\circ$ .

### 1.3.1 Nilsson Model

In the Nilsson model [11] the Schrödinger equation is solved using a deformed anisotropic harmonic oscillator potential, that is parametrised with the deformation parameter  $\beta_2$ . The Nilsson orbitals are defined with the following quantum numbers  $\Omega[N, n_z, \Lambda]$ , where  $\Omega$  is the projection of the angular momentum onto the symmetry axis,  $N$  is the total quantum number and determines the parity as  $(-1)^N$ ,  $n_z$  is the number of oscillator shell quanta along the direction of the symmetry axis and  $\Lambda$  is the projection of the particle orbital angular momentum  $\mathbf{l}$  on the symmetry axis. In this deformed shell model the orbital angular momentum  $\mathbf{l}$  and the intrinsic spin  $\mathbf{s}$  are not conserved, *i.e.* they are not good quantum numbers.

## 1.4 Blocked BCS Calculations

In nuclei pairing correlations between nucleons are very important. The BCS model provides the theoretical basis to study these correlations in nuclei, in analogy to the Bardeen Cooper and Schrieffer (BCS) theory [12], which almost fifty years ago explained superconductivity in metals on the basis of electron pair correlations.

There are clear analogies between both theories, for example if a superconductor is sufficiently heated, the Cooper pairs (correlated electrons) are broken and therefore the superconductivity is lost. In the case of a nucleus, if a nucleus is rotating sufficiently fast the pairing between nucleons is broken which manifests as an increase in the effective moment of inertia [13].

The pairing effect in the BCS theory is considered as a perturbation of the mean-field Hamiltonian and the solution of the eigenvalue problem is derived from a variational principle [14]. The new states created are called single-quasiparticle states with energies given by [14],

$$E_k = \sqrt{(\epsilon_k - \mu)^2 + \Delta^2} \quad (1.11)$$

where  $\epsilon_k$  is the single-particle energy for a Nilsson state  $k$ ,  $\mu$  is the Fermi energy and the pair gap,  $\Delta$ , is given by [14],

$$\Delta = G \sum_k v_k u_k \quad (1.12)$$

$v_k^2$  and  $u_k^2$  are the probabilities for the  $k^{th}$  Nilsson orbital being occupied or unoccupied respectively and  $G$  is the so called monopole pairing strength, which is one of the Hamiltonian parameters.

The free parameter  $G$  is chosen in the BCS calculations to reproduce the lowest 2-quasiparticle states. The neutron pair strength  $G_\nu$  and a proton pair strength  $G_\pi$  are adjusted independently.

The blocked BCS (BBCS) theory takes into account that the Nilsson level that has been occupied by an unpaired particle, cannot be occupied by another particle, and therefore the level is blocked. The Pauli principle prevents this level from participating in the scattering process of nucleons caused by the pairing correlations. The blocking effect manifests as a reduction in the pair gap, which changes to [14],

$$\Delta = G \sum_{k \neq k_j} v_k u_k \quad (1.13)$$

where  $k_j$  is the blocked orbital. This reduction in pairing energy can be large in some cases. This happens particularly for deformed nuclei where, although there

may be twenty or more single-particle levels in the spectrum, only four or five contribute appreciably to the sum [14].

It can be taken into account another residual interaction arising from the interaction of the intrinsic spins of the particles, the so called Gallagher and Moszkowski coupling rules [15]. This interaction favours couplings of *like* particles with opposite spins and *unlike* particles with the same spin. Nevertheless the variation of the state energy will not change by more than a few hundred keV. A compilation of these residual interaction energies between proton-proton, neutron-neutron and proton-neutron orbitals in the 180 mass region can be found in Ref. [16].

To carry out the BCS calculations according to Ref. [16] the deformation parameters  $\beta_2$  and  $\beta_4$ , the proton ( $Z$ ) and neutron ( $N$ ) number and the neutron and proton pair strength  $G_\nu$ ,  $G_\pi$  are all required. The Nilsson single-particle energies  $\epsilon_k$ , can be adjusted to reproduce the experimentally observed single-quasiparticle energies  $E_k$  in the neighbouring odd-mass nuclei. The pair gap,  $\Delta$ , for each configuration of like particles is calculated by blocking the occupied orbitals. The multi-quasiparticle energies,  $E_{mfp}$ , are obtained by combining algebraically the neutron and proton configuration energies [16]

$$E_{mfp} = E^\nu + E^\pi \quad (1.14)$$

## 1.5 Two-State Mixing

In this section, it will be considered the case of two-state mixing due to an interaction,  $\mathbf{V}$ . In turn, it will be considered that the interaction,  $\mathbf{V}$ , mixes the wave functions of the original states, denoted by  $\phi_1$  and  $\phi_2$ , with energies  $e_1$  and  $e_2$  respectively, where both states have the same spin and parity  $I^\pi$ . The wave functions of the mixed states can be written in terms of the original wavefunctions as follows,

$$\begin{aligned} \Psi_1 &= \alpha\phi_1 + \beta\phi_2 \\ \Psi_2 &= -\beta\phi_1 + \alpha\phi_2 \end{aligned} \quad (1.15)$$

where  $\alpha$  and  $\beta$  are the mixing amplitudes and  $\alpha^2 + \beta^2 = 1$ .

The energies of the new states  $E_1$  and  $E_2$  are obtained by diagonalising the Hamiltonian that takes into account, explicitly, the interaction,  $\mathbf{V}$ . The resultant energies are [7],

$$E_{1,2} = \frac{1}{2} \left( (e_1 + e_2) \pm \sqrt{(e_2 - e_1)^2 + 4V^2} \right) \quad (1.16)$$

where  $E_{1,2}$  are the eigenvalues of  $\Psi_{1,2}$  respectively and  $V$  is the mixing matrix element  $V \equiv \langle \phi_1 | \mathbf{V} | \phi_2 \rangle$ , *i.e.* the strength of the interaction.

The mixing amplitude  $\beta$  can be written in terms of the mixing matrix element  $V$  as follows [7],

$$\beta = \frac{1}{\sqrt{1 + \left( \frac{e_2 - e_1}{2V} + \sqrt{1 + \frac{(e_2 - e_1)^2}{4V^2}} \right)^2}} \quad (1.17)$$

Equations 1.16 and 1.17 are universal expressions and do not depend on the nature of the interaction,  $\mathbf{V}$ .

## 1.6 Gamma Decay

The study of  $\gamma$ -ray emission is of considerable importance in nuclear spectroscopy for the study of nuclear structure. Studying  $\gamma$  emission and its competing process, internal conversion, allows the spins and parities of excited states to be determined.

### 1.6.1 Selection Rules

Excited nuclear states decay following an exponential decay time profile of the form ( $e^{-\lambda t}$ ). Consider a  $\gamma$  transition from an initial excited state of energy  $E_i$ , angular momentum  $I_i$  and parity  $\pi_i$  to a final state  $E_f$ ,  $I_f$  and  $\pi_f$ . The energy of the  $\gamma$  is given by<sup>a</sup>

$$E_\gamma = E_f - E_i \quad (1.18)$$

and its angular momentum will be within the limits [17],

$$|I_i - I_f| \leq L \leq I_i + I_f \quad (1.19)$$

---

<sup>a</sup>Note that there is a negligible effect due to the recoil of the nucleus.

The parity change in the transition is given by the selection rules [17]:

$$\begin{aligned}\Delta\pi(EL) &= (-1)^L \\ \Delta\pi(ML) &= (-1)^{L+1}\end{aligned}\quad (1.20)$$

Note that electric and magnetic multipoles of the same order always have opposite parity. Transitions between two  $0^+$  or  $0^-$  states, *i.e.* pure  $\Delta L = 0$ , are forbidden to proceed via  $\gamma$  decay since photons have an intrinsic spin  $1 \hbar$ . Such transitions can occur via internal conversion or internal pair formation (if  $E_\gamma > 1.022$  MeV).

### 1.6.2 Electromagnetic Transition Rates

The motion of protons in the nucleus gives rise to charge and current distributions; charge distributions can be described by electric multipole moments and currents distributions by magnetic multipole moments. The electromagnetic radiation field produced when the nucleus emits radiation in the form of  $\gamma$  rays can be described in terms of a multipole expansion [14, 18, 19]. The total transition probability can be determined by [18]

$$\lambda_{fi} = \frac{8\pi(L+1)}{\hbar L((2L+1)!!)^2} \left(\frac{E_\gamma}{\hbar c}\right)^{2L+1} B(\sigma L; I_i \rightarrow I_f) \quad (1.21)$$

where the values of  $B(\sigma L)$  are known as the *reduced transition probabilities* and are given by [18]

$$B(EL; I_i \rightarrow I_f) = \frac{1}{2I_i + 1} |\langle f \|\hat{Q}\|i\rangle|^2 \quad (1.22)$$

for the electric case, meanwhile for the magnetic case is:

$$B(ML; I_i \rightarrow I_f) = \frac{1}{2I_i + 1} |\langle f \|\hat{M}\|i\rangle|^2 \quad (1.23)$$

where  $\hat{Q}$  and  $\hat{M}$  are the electric and magnetic multipole operators, respectively. It is assumed that the wavelength of the emitted radiation is long compared to the dimensions of the nucleus. In order to account for the different possible orientations of the angular momentum,  $L$ , an average over the initial  $m$  state values and a sum over the final  $m$  state values has been performed.

Table 1.1 shows the electromagnetic transition rate estimates given in terms of the reduced transition probabilities for the lowest multipole orders. The estimates are obtained by multiplying out the constant terms in Equation 1.21.

Table 1.1: Electromagnetic transition rates. The units are:  $T(\sigma L) - s^{-1}$ ,  $B(EL) - e^2 fm^{2L}$ ,  $B(ML) - \mu_n^2 fm^{2L-2}$  when the  $\gamma$ -ray energy  $E$  is expressed in MeV. Taken from [20].

$T(E1) = 1.59 \times 10^{15} B(E1)E^3$	$T(M1) = 1.76 \times 10^{13} B(M1)E^3$
$T(E2) = 1.22 \times 10^9 B(E2)E^5$	$T(M2) = 1.35 \times 10^7 B(M2)E^5$
$T(E3) = 5.76 \times 10^2 B(E3)E^7$	$T(M3) = 6.28 \times 10^0 B(M3)E^7$
$T(E4) = 1.69 \times 10^{-4} B(E4)E^9$	$T(M4) = 1.87 \times 10^{-6} B(M4)E^9$

### Weisskopf Estimates

Electromagnetic transition rates, under the basic assumption that the transition is due to a single proton moving from one spherical shell model state to another can be estimated using the Weisskopf expressions [18],

$$\lambda_{EL} = \frac{8\pi(L+1)}{\hbar L((2L+1)!!)^2} \frac{e^2}{4\pi\epsilon_0\hbar c} \left(\frac{E_\gamma}{\hbar c}\right)^{2L+1} \left(\frac{3}{L+3}\right)^2 c R^{2L} \quad (1.24)$$

and

$$\lambda_{ML} = \frac{8\pi(L+1)}{L((2L+1)!!)^2} \frac{e^2}{4\pi\epsilon_0\hbar c} \left(\mu_p - \frac{1}{L+1}\right)^2 \left(\frac{\hbar}{m_p c}\right)^2 \left(\frac{E_\gamma}{\hbar c}\right)^{2L+1} \left(\frac{3}{L+2}\right)^2 c R^{2L-2} \quad (1.25)$$

where  $\mu_p$  is the magnetic moment and  $m_p$  is the mass of the proton. The wavefunctions of the states are those obtained using a square well potential. By taking  $R = R_0 A^{1/3}$  and the customary replacement  $\left(\mu_p - \frac{1}{L+1}\right)^2 = 10$  [18], estimates can be made for the lower multipole orders. These are known as the *Weisskopf Estimates* and are given in Table 1.2.

Table 1.2: Single particle or Weisskopf estimates. The units are  $s^{-1}$  when the  $\gamma$ -ray energy  $E$  is expressed in MeV and  $A$  is the atomic mass number. Taken from [18].

$T(E1) = 1.0 \times 10^{14} A^{2/3} E^3$	$T(M1) = 5.6 \times 10^{13} E^3$
$T(E2) = 7.3 \times 10^7 A^{4/3} E^5$	$T(M2) = 3.5 \times 10^7 A^{2/3} E^5$
$T(E3) = 3.4 \times 10^1 A^2 E^7$	$T(M3) = 1.6 \times 10^1 A^{4/3} E^7$
$T(E4) = 1.1 \times 10^{-5} A^{8/3} E^9$	$T(M4) = 4.5 \times 10^{-6} A^2 E^9$

The estimates are not realistic calculations of the transition rates, but provide values that can be compared to those measured experimentally.

## 1.7 Internal Conversion

Internal conversion is an electromagnetic process that competes with  $\gamma$  ray emission. In the case of internal conversion the electromagnetic multipole fields of the nucleus do not result in the emission of a photon, but rather the emission of a bound electron usually from the inner atomic shells. Internal conversion is not a two step process in which a photon is first emitted and then knocks out an atomic electron; this process has a very small probability to occur. The electron emitted in internal conversion will have a kinetic energy, such that [21]

$$T_e = \Delta E - B \quad (1.26)$$

where  $\Delta E$  is the transition energy and  $B$  is the binding energy that has to be supplied to knock the electron out of the atomic shell. Since  $B$  will change depending on which shell the electron resides, there will be internal conversion electrons emitted with different energies, but corresponding to the same nuclear transition. The emission of the electron and the resultant rearrangement of the electrons will subsequently lead to the emission of an X-ray or Auger electrons.

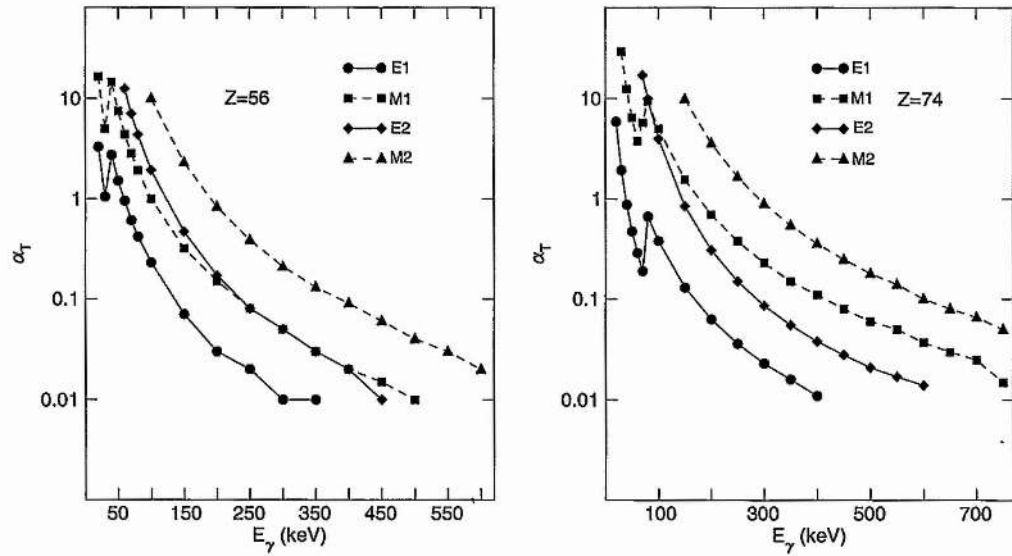


Figure 1.3: Theoretical internal conversion coefficients for  $E1$ ,  $M1$ ,  $E2$  and  $M2$  transitions for atomic numbers  $Z = 56$  (left) and  $Z = 74$  (right).

The internal conversion coefficient  $\alpha$ , is defined as follows:

$$\alpha = \frac{\lambda_e}{\lambda_\gamma} \quad (1.27)$$

where  $\lambda_e$  is the decay probability due to electron conversion and  $\lambda_\gamma$  is due to  $\gamma$  emission.

The total internal conversion coefficient,  $\alpha_T$ , is given by the sum of the individual coefficients for each atomic shell:

$$\alpha_T = \alpha_K + \alpha_L + \alpha_M + \dots \quad (1.28)$$

The total decay probability then becomes,

$$\lambda_T = \lambda_\gamma(1 + \alpha_T) \quad (1.29)$$

The internal conversion coefficients for electric and magnetic multipoles in a non-relativistic calculation are [22],

$$\alpha(EL) \approx \frac{Z^3}{n^3} \left( \frac{L}{L+1} \right) \left( \frac{e^2}{4\pi\epsilon_0\hbar c} \right)^4 \left( \frac{2m_e c^2}{E} \right)^{L+5/2} \quad (1.30)$$

$$\alpha(ML) \approx \frac{Z^3}{n^3} \left( \frac{e^2}{4\pi\epsilon_0\hbar c} \right)^4 \left( \frac{2m_e c^2}{E} \right)^{L+3/2} \quad (1.31)$$

where  $Z$  is the atomic number,  $n$  is the principal quantum number of the electron shell and  $E$  is the transition energy. Figure 1.3 shows the theoretical internal conversion coefficients for  $E1$ ,  $M1$ ,  $E2$  and  $M2$  transitions for atomic numbers  $Z = 56$  and  $Z = 74$ .

These approximate expressions give us the main features of the conversion coefficients:

- i) They increase as  $Z^3$ , therefore the conversion process is much more important for heavy nuclei than for light nuclei.
- ii) They increase rapidly with decreasing transition energy.
- iii) They increase rapidly as the multipole order increases.
- iv) They decrease as  $1/n^3$  for higher atomic shells ( $n > 1$ ).

Transitions with energies greater than 1.022 MeV can also proceed through internal pair formation, in which the state decays by producing an electron-positron pair [21].

## 1.8 Angular Distribution of $\gamma$ Rays

The measurement of the angular distribution of a  $\gamma$ -ray transition can help to determine the multipolarity of the transition and consequently the spins of the excited nuclear states. The nuclei produced in a fusion-evaporation reaction, for example, are aligned with the angular momentum vector perpendicular to the beam direction. It is therefore possible to obtain an anisotropic angular distribution [23]. If there is no preferred direction, the angular distributions are isotropic. The initial alignment of the nucleus can be smeared out by the emission of evaporated particles.

The angular distribution formula is given by [24]

$$W(\theta) = \sum_k A_k P_k(\cos \theta) \quad (1.32)$$

where  $W(\theta)$  is the  $\gamma$ -ray intensity measured at angle  $\theta$  to the beam direction. In

the case of  $\gamma$ -ray emissions, where the parity is conserved, only  $k=\text{even}$  numbers are considered, less than or equal to  $2l$  where  $l$  is the angular momentum taken away by the emitted photon.  $P_k(\cos \theta)$  are the standard Legendre polynomials and the  $A_k$  are the angular distribution coefficients. The  $A_k$  value depends on the  $m$ -population distribution and the  $I^\pi$  values of the initial and final states [24].

For an electric dipole ( $E1$ ) transition  $\Delta L = 1$ , or magnetic dipole transition ( $M1$ ),  $W(\theta)$  will be given by

$$W(\theta) = A_0(1 + A_2 P_2(\cos \theta)) \quad (1.33)$$

where  $P_2(\cos \theta) = \frac{1}{2}(\cos^2 \theta - 1)$  and  $A_0$  is the “true” intensity.

For an electric quadrupole ( $E2$ ) transition  $\Delta L = 2$ , or magnetic quadrupole transition ( $M2$ ), the angular distribution will be given by

$$W(\theta) = A_0(1 + A_2 P_2(\cos \theta) + A_4 P_4(\cos \theta)) \quad (1.34)$$

where  $P_4 = \frac{1}{8}(35 \cos^4 \theta - 30 \cos^2 \theta + 3)$ .

Experimentally, the dependence of the  $\gamma$ -ray intensity versus the polar angle of the  $\gamma$  detectors will be directly measured. In this thesis those angles will be given by the germanium detectors of GAMMASPHERE (see *Chapter 3*).

# Chapter 2

## Experimental Considerations

### 2.1 Nuclear Reactions of Heavy Ions

The different nuclear interactions between heavy ions can be, broadly speaking, divided into three main categories, depending on the energy involved in the interaction. Nevertheless, a nuclear reaction is determined in addition to the centre-of-mass energy by the impact parameter  $b$  and the nature of the projectile and target.

For low energy reactions (1-10 MeV/A) fusion evaporation type reactions might happen. These reactions occur at small values of the impact parameter and the projectile and target stay together for enough time (from  $10^{-18}$  s to  $10^{-16}$  s) to form a hot compound nucleus. In this case the resulting nuclei can be formed in a high spin state, thus allowing the nuclear spectroscopy of nuclear states at extremes of angular momentum [25]. As the beam energy increases the reactions become more peripheral and the reaction times are much faster,  $\sim 10^{-22}$  s, and the impact parameter is extended compared to fusion-evaporation reactions. Nucleon transfer or deep inelastic reactions (DIC) can occur in which a few nucleons are transferred but the beam and target retain their original character [26, 27, 28]. These reactions are still not completely understood as the mechanism through which nucleons are transferred becomes extremely complicated as the number of nucleons increases [29, 30], but the study of these reactions provides valuable information on particle-

particle correlations in nuclei, especially at energies close to the Coulomb barrier [31]. In addition these reactions populate regions of the Segré Chart that otherwise can not be populated with fusion-evaporation reactions using stable beam and target combinations. For nearly a decade DIC have been successfully used to populate neutron rich nuclei for spectroscopic studies. During the last decade Broda *et al.* have used DIC with thick-targets and large arrays of germanium detectors to study exotic nuclei [32, 33]. It has been shown that using DIC it is possible to populate high-spin states in nuclei along the valley of stability and towards the neutron-rich side [34, 35, 36, 37]. For beam energies greater than about 40MeV/A a large fraction of the cross section goes into nuclear fragmentation, producing a large range of nuclei [25, 38, 39]. The work carried out in this thesis involved the use of deep inelastic collisions and in the following sections these reactions are discussed in more detail.

## 2.2 Deep-Inelastic Nuclear Reactions

A considerable amount of data on deep inelastic collisions has been accumulated over the last three decades (*e.g.* [29, 30, 32, 40, 41]), albeit limited in character. From these accumulated experimental data, it is possible to list the following general features of DIC.

- i) An essential feature is that these collisions preserve the binary character of the system, so that the final fragments maintain some resemblance to the initial nuclei,
- ii) These reactions involve a fast redistribution of protons and neutrons among the colliding nuclei, which is governed by strong driving forces associated with the potential energy surface of the dinuclear complex. This fast rearrangement of neutrons and protons is called  $N/Z$  equilibration [26]. The time involved in this equilibration is around  $10^{-22}$  seconds [41],
- iii) Momentum analyses of the nuclide distributions indicate that the exchange of nucleons starts out in an uncorrelated fashion [41]. Then, due to the confinements imposed on the exchange process by the gradients of the potential energy surface,

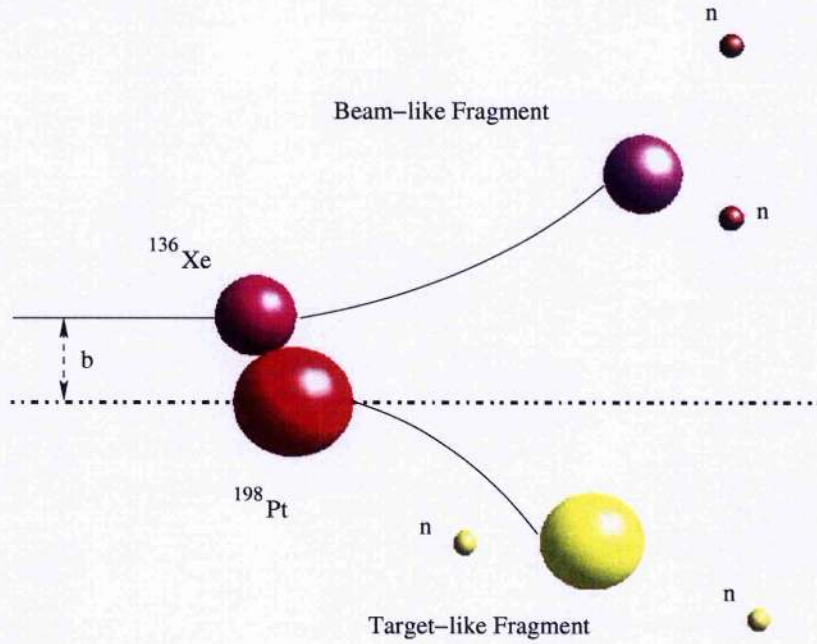


**Figure 2.1:** Semiclassical description of a Deep Inelastic Nuclear Reaction between heavy ions.

a correlation develops with increasing energy loss. Moreover, there are indications that the development of charge and mass flow is not only determined by macroscopic dynamics and liquid-drop potentials, but for small bombarding energies and small energy losses, single-particle degrees of freedom and tunneling probabilities add to the complexity of the observed phenomena [40],

- iv) Angular momentum is transferred from relative orbital motion to the intrinsic spin of the two primary fragments [41], and
- v) The primary fragments produced in these reactions de-excite mainly through the evaporation of light particles, namely neutrons, protons and  $\alpha$ -particles, the emission of  $\gamma$  rays and in the case of heavier fragments via fission.

A semiclassical schematic illustration of a DIC can be seen in Fig. 2.1.

### 2.2.1 Kinematics in Binary Reactions

The following kinematic equations refer to the laboratory reference frame, where the nuclei in the target are considered at rest. If the reaction plane is defined by the direction of the incident beam and one of the outgoing particles, then conserving the component of momentum perpendicular to that plane shows immediately that the motion of the second outgoing particle must lie in the same plane, see Fig. 2.2.

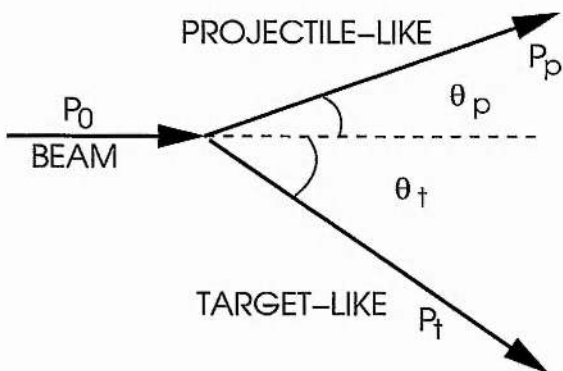


Figure 2.2: Reaction geometry. Projectile and target recoils define the reaction plane of the binary reaction.

Conservation of linear momentum gives,

$$\begin{aligned} P_0 &= P_p \cos \theta_p + P_t \cos \theta_t \\ 0 &= P_p \sin \theta_p - P_t \sin \theta_t \end{aligned} \quad (2.1)$$

where  $P_0$  is the initial momentum of beam,  $P_p$ ,  $P_t$  are the recoil momenta for the projectile and the target recoils respectively and  $\theta_p$ ,  $\theta_t$  are the scattering angles for the projectile and target nuclei respectively.

After some algebra manipulation, the relation of the recoil momenta to the initial beam momentum is given by,

$$P_{p,t} = P_0 \frac{\sin(\theta_t, \theta_p)}{\sin(\theta_p + \theta_t)} \quad (2.2)$$

In a non-relativistic approximation the momentum is given by  $P = m\beta c$ , whereas the relativistic momentum is given by  $P = m\beta c\gamma$  where  $m$  is the mass and  $\gamma = \frac{1}{\sqrt{1-\beta^2}}$ .

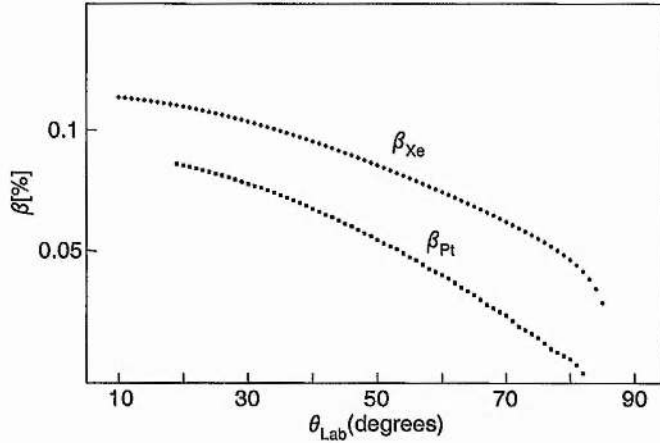


Figure 2.3: Calculated velocities of the projectile and the target recoils for the particular case of a  $^{136}\text{Xe}$  beam at 850 MeV in the laboratory frame impinging on a  $^{198}\text{Pt}$  target. An elastic collision and simple two-body kinematics have been assumed.

If an elastic collision is assumed, where the energy conservation can be given by Equation 2.3, then using Equations 2.2 and 2.3 for a given recoil angle, the recoil angle of the other fragment and the velocity of the recoils can be calculated using,

$$\frac{P_0^2}{2m_{\text{beam}}} = \frac{P_p^2}{2m_p} + \frac{P_t^2}{2m_t} \quad (2.3)$$

Figure 2.3 shows the calculated velocities for the projectile and target recoils in the case of a  $^{136}\text{Xe}$  beam at laboratory energy of 850 MeV impinging on a  $^{198}\text{Pt}$  target.

### 2.2.2 Angular Momentum in Binary Reactions

Unlike the fusion evaporation reactions where most of the input angular momentum of the reaction goes into the intrinsic angular momentum of the final products [42, 43], in deep inelastic collisions the transfer of angular momentum into intrinsic spins is not as efficient. There are different semiclassical models to explain the angular momentum distribution of the nuclei produced in a deep inelastic collision. The sharing of the angular momenta between relative and intrinsic rotation depends

upon the details of the frictional forces between the nuclei. The particular limiting cases of interest are *sliding*, *rolling* and *sticking* modes [40, 41, 44] which correspond to minimum, intermediate and maximum angular momentum dissipation from the relative motion.

Consider a nucleus of radius  $r_p$  approaching the target nucleus of radius  $r_t$  at an impact parameter such that the initial angular momentum is  $L$ . In any real case there would be a distribution of  $L$  values corresponding to the range of partial waves that contribute to the DIC. After contact, the spheres will move around the centre of mass with an angular speed  $\omega$ . Each sphere may have its own intrinsic rotation  $\omega_p$  and  $\omega_t$ . Conservation of angular momentum requires:

$$L = \mu R^2 \omega + \mathfrak{I}_p \omega_p + \mathfrak{I}_t \omega_t \quad (2.4)$$

where  $R = r_p + r_t$ ,  $\mathfrak{I}$  is the moment of inertia and  $\mu$  is the reduced mass, which is given in terms of the mass numbers of the target  $A_t$  and projectile  $A_p$  as

$$\mu = \frac{A_p A_t}{A_p + A_t}, \quad (2.5)$$

and  $J_p = \mathfrak{I}_p \omega_p$  and  $J_t = \mathfrak{I}_t \omega_t$  are the intrinsic angular momenta of the projectile and target, whose calculated values can be compared with those obtained experimentally. The maximum angular momentum input in the reaction can be estimated [45] to be,

$$L_{max} = 0.219 R \sqrt{\mu(E_{cm} - V_{cm})} \quad (2.6)$$

The *Sliding* model [41] is the simplest case and the one in which no angular momentum is put into the fragments ( $J_p = J_t = 0$ ), since they slide with respect to one another.

The *sticking* model [41] corresponds to the case where the projectile and target stick together, each nucleus rotates around its own centre at the same speed, *i.e.* ( $\omega_p = \omega_t$ ). This model is the one that converts more translational energy into rotational energy. From Equation 2.4 one can deduce the following relative angular speed:

$$\omega = \frac{L}{\mu R^2 + \mathfrak{I}_p + \mathfrak{I}_t} \quad (2.7)$$

then

$$J_p = \frac{\mathfrak{S}_p}{\mu R^2 + \mathfrak{S}_p + \mathfrak{S}_t} L \quad (2.8)$$

and

$$J_t = \frac{\mathfrak{S}_t}{\mu R^2 + \mathfrak{S}_p + \mathfrak{S}_t} L. \quad (2.9)$$

If the nucleus is considered to be a rigid sphere then  $\mathfrak{S} = \frac{2}{5}Ar^2$  and  $r = 1.2A^{1/3}$ , where  $A$  is the mass of the nucleus and  $r$  is its radius. For the reaction  $^{198}\text{Pt} + ^{136}\text{Xe}$  at 850 MeV that will be discussed in this thesis, the following values are obtained. An incident  $^{136}\text{Xe}$  beam at a laboratory energy of 850 MeV gives an  $L = L_{max} = 297 \hbar$ , then

$$\mathfrak{S}_{Xe} = \frac{2}{5}A_{Xe}r_{Xe}^2 = 2072 \text{ fm}^2 \text{ a.m.u.}, \quad (2.10)$$

$$\mathfrak{S}_{Pt} = \frac{2}{5}A_{Pt}r_{Pt}^2 = 3874 \text{ fm}^2 \text{ a.m.u.} \quad (2.11)$$

and

$$\mu R^2 = \frac{A_{Xe}A_{Pt}}{A_{Xe} + A_{Pt}}(r_{Xe} + r_{Pt})^2 = 13973 \text{ fm}^2 \text{ a.m.u.} \quad (2.12)$$

Therefore the intrinsic spin put into the fragments for the *sticking* mode can be estimated to be,

$$J_{Xe} = \frac{\mathfrak{S}_{Xe}}{\mu R^2 + \mathfrak{S}_{Xe} + \mathfrak{S}_{Pt}} L \approx 31\hbar \quad (2.13)$$

and

$$J_{Pt} = \frac{\mathfrak{S}_{Pt}}{\mu R^2 + \mathfrak{S}_{Xe} + \mathfrak{S}_{Pt}} L \approx 58\hbar \quad (2.14)$$

The *rolling* model [41, 44] is a situation intermediate between the *sliding* and the *sticking* models, which arises in the presence of a strong frictional force. In the rolling case, the point of contact has a velocity equal to zero in the rest frame. The condition for not sliding is given by,

$$r_p(\omega_p - \omega) + r_t(\omega_t - \omega) = 0 \quad (2.15)$$

If a frictional force,  $\mathbf{F}$ , is considered to be acting at the contact point, this force gives a torque on the projectile and the target in opposite directions,

$$\mathbf{F} \times \mathbf{r} \rightarrow \mathbf{J} \quad (2.16)$$

Therefore, the angular momentum sharing is given by,

$$\frac{J_p}{J_t} = \frac{r_p}{r_t} = \frac{\mathfrak{S}_p \omega_p}{\mathfrak{S}_t \omega_t} \rightarrow \frac{\omega_p}{\omega_t} = \frac{\mathfrak{S}_t r_p}{\mathfrak{S}_p r_t} \quad (2.17)$$

Combining Equations 2.15 and 2.17 one obtains,

$$\omega_t = \frac{\mathfrak{S}_p r_t R \omega}{\mathfrak{S}_t r_p^2 + \mathfrak{S}_p r_t^2} \quad (2.18)$$

and

$$\omega_p = \frac{\mathfrak{S}_t r_p R \omega}{\mathfrak{S}_t r_p^2 + \mathfrak{S}_p r_t^2} \quad (2.19)$$

Recalling that  $\mathfrak{S}_p = \frac{2}{5} A_p r_p^2$  and  $\mathfrak{S}_t = \frac{2}{5} A_t r_t^2$ , the sum of the angular momenta of the projectile and target is given by,

$$J_p + J_t = \mathfrak{S}_p \omega_p + \mathfrak{S}_t \omega_t = \frac{2}{5} \mu R^2 \omega \quad (2.20)$$

Moreover

$$L = \mu R^2 \omega + J_p + J_t = \mu R^2 \omega + \frac{2}{5} \mu R^2 \omega = \frac{7}{5} \mu R^2 \omega \quad (2.21)$$

therefore

$$J_p + J_t = \frac{2}{7} L \quad (2.22)$$

A fraction of  $2/7$  of the initial angular momentum is converted into the intrinsic angular momentum of the target and projectile while  $5/7$  stays in relative motion. Combining Equations 2.17 and 2.22 one obtains,

$$J_p = \frac{2}{7} \left( \frac{1}{1 + (\frac{A_t}{A_p})^{1/3}} \right) L \quad (2.23)$$

and

$$J_t = \frac{2}{7} \left( \frac{1}{1 + (\frac{A_p}{A_t})^{1/3}} \right) L. \quad (2.24)$$

So in the same case as before, for a  $^{136}\text{Xe}$  beam at a laboratory energy of 850 MeV incident on a  $^{198}\text{Pt}$  target, the angular momentum transferred to the fragments for the rolling mode can be estimated to be,

$$J_{Xe} \approx 17\hbar \quad (2.25)$$

and

$$J_{Pt} \approx 45\hbar \quad (2.26)$$

In this case the model predicts less angular momentum put into the fragments than in the case of the *sticking* model.

### 2.2.3 Grazing Angle in a DIC

For experimental purposes it is very important to know where the *grazing angle* of the reaction in the laboratory frame is expected to be due to the fact that at this angle the binary reaction cross section is expected to be maximised [46]. The grazing angle [46], is the angle at which one can be sure that nuclear interactions happen, rather than only Coulomb or Rutherford interactions. It is defined as the angle at which the distance of closest approach,  $d$ , is given by [21, 45]

$$d = \left( \frac{Z_t Z_p e^2}{4\pi\epsilon_0 E_k} \right) \left( 1 + \csc \frac{\theta}{2} \right) \quad (2.27)$$

where  $Z_t$  and  $Z_p$  are the atomic numbers of the two nuclei involved and  $E_k$  is the kinetic energy. The distance of the closest approach equals the sum of the nuclear radii, *i.e.* when the two nuclei are just touching, which can be estimated by the expression,

$$d = 1.2(A_t^{\frac{1}{3}} + A_p^{\frac{1}{3}}) fm \quad (2.28)$$

where  $A_t$  and  $A_p$  are the nuclear mass numbers for the target and beam respectively. A quick estimate for the grazing angle can be obtained equalizing Equations 2.27 and 2.28.

For the reaction of interest in this thesis ( $^{136}\text{Xe}$  at 850 MeV impinging on a  $^{198}\text{Pt}$  target) the grazing angle is roughly the same for beam and target-like fragments in the laboratory frame, *i.e.*  $50^\circ$ . See figures later in *Chapter 3*.

### 2.2.4 Q-value of a Nuclear Reaction

The Q-value of a nuclear reaction can be derived from the conservation of energy. In a nuclear reaction, the Q-value can be defined as [21],

$$Q = (m_{initial} - m_{final})c^2 = T_{final} - T_{initial} \quad (2.29)$$

where  $m_{initial}$  and  $m_{final}$  are the total initial and final masses of the system respectively and  $T_{initial}$ ,  $T_{final}$  are the total kinetic energies of the system before and after the reaction respectively.

The Q-value may be positive or negative. If  $Q > 0$  ( $T_{final} > T_{initial}$ ), then nuclear mass or binding energy is released as kinetic energy, which is shared between the final products. On the contrary when  $Q < 0$  ( $T_{final} < T_{initial}$ ), then the kinetic energy has been converted into binding energy. The changes in mass and energy must be related by the Einstein's familiar equation from special relativity,  $\Delta E = \Delta mc^2$ .

## 2.3 Gamma-Ray Interactions in Matter

The detection of photons is an indirect process, involving an interaction between the photon and the detector material which results in all, or part of the energy being transferred to one or more electrons. It is only through the energy loss from these electrons that the energy of the  $\gamma$  ray is converted into an electrical signal. For the signal to be a good representation of the energy of the incident photon it is desirable that the photon energy is completely converted into kinetic energy of electrons in the material and that no energy escapes from the volume of the detector in the form of low-energy or back scattered photons or secondary electrons. At the  $\gamma$ -ray energies of interest, three basic interaction processes are dominant in converting the incident photon energy into electrons in a detector [17]:

i) *Photoelectric effect.*

This process results in the total absorption of the photon and the release of an electron from an atom of the detector material. The photoelectron energy is equal

to the incident photon energy minus the binding energy of the electron in the atom.

$$E_e = E_\gamma - E_b \quad (2.30)$$

The X-rays subsequently emitted by vacancy filling in the shells of the atom are generally absorbed in a very short range within the detector, so the total signal corresponds to the total conversion of the original photon energy into kinetic energy of the electrons. The presence of a large mass is required to conserve momentum in the photoelectric process (*i.e.* the interaction must be with a bound electron). The probability of an interaction is a strong function of the atomic number in the absorbing material. The cross-section of the interaction, over the range of energies of interest and usual atomic number  $Z$  of detector material can be approximated [47] by:

$$\sigma_{pe} = k_{pe} \frac{Z^{4.5}}{E_\gamma^3} \quad (2.31)$$

where  $k_{pe}$  is a proportionality constant,  $\sigma_{pe}$  is the probability of a photon of energy  $E$  interacting with an electron in a material of atomic number  $Z$ . Materials with higher atomic numbers have much larger cross-sections and therefore stop a much higher proportion of photons.

Photoelectric absorption is the dominant interaction between  $\gamma$  rays and semiconductors below 100 keV. To detect the full energy peak, the final interaction in a full energy event must be of this type, since it is the only mechanism that does not produce secondary photons (see below). For this type of interaction, the full energy of the  $\gamma$  ray is transferred to the semiconductor material, effectively around the position where the interaction takes place.

### *ii) Compton effect.*

This is the classical “billiard ball” collision process whereby the photon strikes an electron resulting in the electron acquiring some of the photon’s original energy and at the same time, producing a lower energy photon. The energy of the scattered photon is given by [17].

$$E_\gamma' = \frac{E_\gamma^0}{1 + \frac{E_\gamma^0}{m_0 c^2} (1 - \cos \theta)} \quad (2.32)$$

where  $E_\gamma^0$  is the initial photon energy,  $m_0$  is the rest mass of an electron and  $c$  is the velocity of light ( $m_0c^2 = 511$  keV). For small scattering angles  $\theta$ , very little energy is transferred. The maximum energy  $E_{max}$  given to the electron (in a head-on collision) is:

$$E_{max} = \frac{E_\gamma^0}{1 + m_0c^2/2E_\gamma^0} \quad (2.33)$$

In a realistic experimental spectrum, the Compton effect produces a distribution of  $\gamma$  rays up to the energy given by Equation 2.33, which is known as the *Compton edge*. At higher incident photon energies, the photoelectric process becomes quite unlikely (see Equation 2.31), but the Compton process remains relatively effective since its probability is given [47] by

$$\sigma_{cs} = k_{cs} \frac{Z}{E} \quad (2.34)$$

where  $k_{cs}$  is a proportionality constant.

This is fortunate because the Compton-scattered photons stand a good chance of producing photoelectrons; in this case the summed energies of the Compton-produced electron and the photoelectron is equal to  $E$ , and the double event appears as one count in the full amplitude peak. Over much of the  $\gamma$ -ray energy range of interest (*i.e.* between approximately 200 keV and 2 MeV) this double (or multiple) process contributes most of the counts in the full-energy peak. As a result the greater the  $\gamma$ -ray energy increases, the fewer full energy (photoelectric) events will occur. For this interaction mechanism, only part of the initial photon energy ( $E_\gamma^0$ ) is transferred to the detector at the position of interaction.

The probability for Compton scattering at an angle  $\theta$  is predicted by the *Klein-Nishina formula* for the differential cross section per electron [23]<sup>a</sup>

$$\frac{d_e\sigma}{d\Omega} = \frac{1}{2} r_0^2 \left\{ \frac{1}{[1 + \alpha(1 - \cos \theta)]^2} \left[ 1 + \cos^2 \theta + \frac{\alpha^2(1 - \cos \theta)^2}{[1 + \alpha(1 - \cos \theta)]} \right] \right\} \quad (2.35)$$

In this expression  $\alpha$  is the photon energy in units of the electron rest energy ( $\alpha = E_\gamma/m_0c^2$ ) and  $r_0$  is a parameter called the *classical electron radius*,  $r_0 =$

<sup>a</sup>The Klein-Nishina formula is correctly written in references [17] and [23], but is incorrect in reference [21]

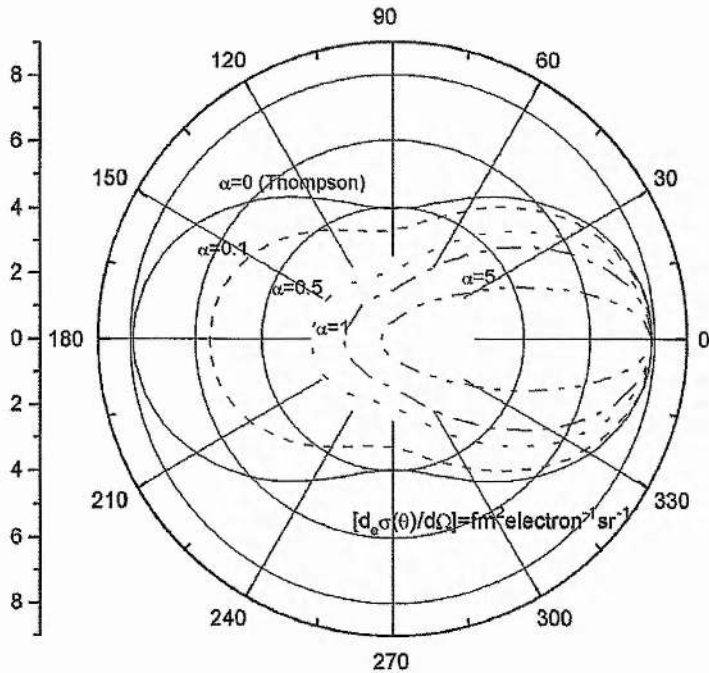


Figure 2.4: Differential cross-section  $d\sigma(\theta)/d\Omega$  for the production of secondary photons from Compton scattering. Curves are shown for six different values of primary photon energy ( $\alpha = 1, E_\gamma = 511 \text{ keV}$ ).

$e^2/4\pi\epsilon_0 m_0 c^2 = 2.818 \text{ fm}$  (this is simply a convenient parameter and has nothing to do with the “size” of the electron).

Inspection of the plot in Fig. 2.4 for the Klein-Nishina formula shows that the higher the  $\gamma$ -ray energy, the more improbable large scattering angles are.

### *iii) Pair production.*

This process can only take place when the incident photon energy exceeds the 1.022 MeV required to create an electron-positron pair. The excess energy (greater than 1.022 MeV) is transformed into the shared kinetic energy of the electron and positron, which subsequently then produce ionization along their tracks. When the positron comes to rest, it annihilates with an electron in the detector material to

produce two 511 keV photons which are emitted back-to-back in order to conserve momentum. The spectrum produced by this process always contains features whose relative intensities depend on the particular geometry of the detector. A full energy peak is produced when both 511 keV annihilation photons are absorbed in the detector, a peak in the spectrum at 511 keV less than the full energy corresponds to the escape of one 511 keV photon (<sup>single</sup><sub>escape</sub> peak) while a third peak of 1.022 MeV below the full energy peak, corresponds to the escape of both 511 keV photons (the double escape peak).

The cross section for pair production  $\sigma_{pp}$  is given by [47]

$$\sigma_{pp} = k_{pp}Z^2 \ln(E) - k_{pp}z^2 \ln(1.022\text{MeV}) = k_{pp}Z^2 \ln(E) - \sigma_{ppth} \quad (2.36)$$

where  $k_{pp}$  is a proportionality constant and the second term explicitly indicates the 1.022 MeV threshold.

### 2.3.1 Suppression of Compton Events

For the typical  $\gamma$ -ray energies which are measured in nuclear physics studies, the dominant interaction process is *Compton scattering*. A  $\gamma$  ray can interact by a Compton effect and the secondary  $\gamma$  ray may escape the detector, contributing to the Compton background and decreasing the Peak-to-Total ratio P/T. This ratio can be improved if the detector is surrounded by a shield detector to veto the events. For germanium detectors a scintillator made from Bismuth Germanate (BGO) is usually chosen due to its high average atomic number  $Z_{average} = 27.6$  and high density  $\rho = 7.12\text{g/cm}^3$  [48] (the probability of detecting  $\gamma$  rays increases with the atomic number and the density). If both detectors detect a  $\gamma$  ray within a fixed time interval, the event is discarded from the spectrum.

### 2.3.2 Probability of Detecting a $\gamma$ Ray

From the cross-section for an interaction, the corresponding linear attenuation coefficient is defined as [17]

$$\mu_i = \sigma_i N_{atom} = \sigma_i \rho \frac{N_A}{M} \quad (2.37)$$

where  $N_{atom}$ ,  $M$ ,  $\rho$ ,  $N_A$  are atomic densities, the molar mass, the density and the *Avogadro Number*. The linear attenuation coefficient gives the probability that a photon from a beam impinging on the detector interacts with the detector per unit path length [17]. For  $\gamma$  rays, using Equations 2.31, 2.34 and 2.36, one obtains,

$$\mu(E) = N_{atom} \left( k_{pe} \frac{Z^{4.5}}{E_\gamma^3} + k_{es} \frac{Z}{E} + k_{pp} Z^2 \ln(E) - \sigma_{ppth} \right) \quad (2.38)$$

Figure 2.5 shows the different attenuation coefficients for the three types of interaction in Ge and the sum over the range of energies of interest. It demonstrates that Compton scattering dominates the deposition of energy between 150 keV and 8 MeV. In this range of energies, further interactions will be required to fully absorb the total photon energy in a detector.

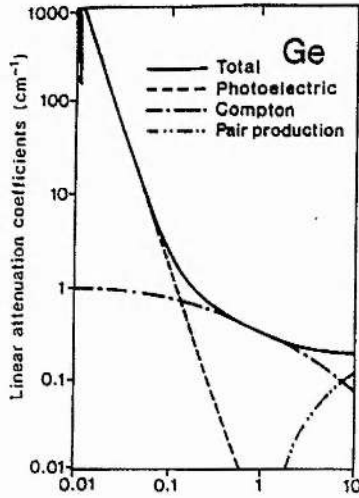


Figure 2.5: Gamma-ray linear attenuation coefficients for Ge as a function of  $\gamma$ -ray energy. Taken from Ref. [49]

If  $N_0$  photons impinge on the detector material, the number of photons,  $N$ , after

a length  $x$  which have not undergone an interaction is given by

$$N = N_0(1 - e^{-\mu x}) \quad (2.39)$$

This attenuation is clearly related to the overall detection efficiency. The average distance travelled by a  $\gamma$  ray in the detector before an interaction happens, is given by the mean free path  $\lambda$ , where,

$$\lambda = \frac{1}{\mu} \quad (2.40)$$

and  $\lambda$  varies between a few tens of  $\mu m$  to a few  $cm$  in Ge [17], depending on the  $\gamma$ -ray energy, and refers to the average thickness after which the intensity of an incident photon is reduced by a factor of  $e^{-1}$  ( $= 0.368$ ). The dependence on the material density  $\rho$  can be removed by using the mass attenuation coefficient  $\mu/\rho$ .

### 2.3.3 Deposition of the $\gamma$ -Ray Energy in Germanium

For all interaction types, a high energy electron, (and in the case of pair production also a positron), is released and it is only through its interaction with the material that the photon is detected. In a semiconductor the active volume for detecting charged particles is the depletion region of a reversed biased diode. In this region, the kinetic energy of the electron is consumed by creating electron-hole pairs, but at higher kinetic energies, Bremsstrahlung increasingly contributes to the total energy transfer. For an electron with 1 MeV kinetic energy, Bremsstrahlung represents about 5% of the total energy loss in Ge. The energy transferred by the fast electron to the semiconductor per unit displacement is the sum of the specific energy loss of a charged particle in a material, given by the Bethe-Bloch formula [50]

$$-\left(\frac{dE}{dx}\right)_{\text{collision}}^{\text{electron}} = \frac{2\pi e^4 N_{\text{atom}} Z}{m_0 v^2} \left[ \ln\left(\frac{m_0 v^2 E}{2I^2(1-\beta^2)}\right) + (1-\beta^2) \right. \\ \left. - \ln 2(2\sqrt{(1-\beta^2)} - 1 + \beta^2) + \frac{1}{8}(1 - \sqrt{(1-\beta^2)})^2 \right] \quad (2.41)$$

and the distribution from Bremsstrahlung [50],

$$-\left(\frac{dE}{dx}\right)_{\text{radiation}}^{\text{electron}} = \frac{\alpha N_{\text{atom}} E Z (Z+1) e^4}{m_e^2 c^4} \left( 4 \ln \frac{2E}{m_0 c^4} - \frac{4}{3} \right) \quad (2.42)$$

where  $\alpha$  is the fine structure constant,  $e$ ,  $m_0$ , are the electron charge and rest mass,  $c$  is the velocity of light in vacuum,  $E$  and  $v$  are the energy and velocity of the fast electron respectively,  $\beta = v/c$ ,  $Z$  and  $N_{atom}$  are the atomic number and atomic density in  $atoms/cm^3$  of the detector material respectively and  $I$  is the average ionization potential of the material.

The total energy loss is simply the sum of these two terms:

$$\left(\frac{dE}{dx}\right)^{electron} = \left(\frac{dE}{dx}\right)^{electron}_{collision} + \left(\frac{dE}{dx}\right)^{electron}_{radiation} \quad (2.43)$$

Combining both equations, the average distance covered by an electron before completely depositing its kinetic energy in the detector can be calculated. It illustrates that in Ge the energy is transferred to the detector [50] within a few  $mm$  of the electron being produced for all energies of interest.

Once the energy of the positron becomes comparable to the thermal energy of the electrons in the semiconductor crystal, it annihilates and at least two photons must be produced in order to conserve momentum. For the full energy of the positron to be deposited in the detector, all secondary photons must be absorbed. As the positron and the fast electron lose nearly the same energy and have the same properties, their ranges are comparable.

## 2.4 General Description of HPGe Detectors

There are different kinds of HPGe detectors depending on the residual minority carrier impurities. If the acceptors dominate, the electrical properties of the semiconductor crystal are mildly  $p$  type, if donor impurities dominate, high purity  $n$  type is the result. The level of impurities in these detectors is approximately  $10^9 - 10^{10} atoms/cm^3$ .

The configuration that is widely used is a *closed-ended coaxial (bulletized)* configuration, where the central core is removed and the electrical contacts are on the inner and on the outer surface of the cylindrical crystal. This configuration provides a quasi-planar front surface that can serve as an entrance window for weakly

penetrating radiation.

In a Germanium detector, the active volume for detecting radiation is the depletion region of a reversed biased diode. For an intrinsic semiconductor material with impurity concentration  $N$  and dielectric constant  $\epsilon$ , applying a reversed biasing voltage  $V_{BIAS}$  produces a depletion region depth

$$d = \sqrt{\frac{2\epsilon V_{BIAS}}{eN}} \quad (2.44)$$

When the whole block of material can be depleted, the minimum voltage that accomplishes full depletion is called the depletion voltage. In this region the high electric field separates the electron-hole pairs before recombination can occur. The charge carriers then drift under the influence of the field to the corresponding contacts, as indicated in Fig. 2.6. The rectifying contact is always the outer electrode of the crystal, producing higher field strengths in the large volume corresponding to larger radii than when it is placed at the core hole. Therefore  $n$ -type detectors have the  $n^+$  contact on the central electrode and the  $p^+$  contact on the outer surface, see Fig. 2.6, whereas  $p$ -type crystals have the contacts exchanged.

The only mechanism relevant for charge to be lost is trapping. Some of the other elements and any lattice defects present in the crystal create deep impurities or traps [51, 52]. The difference with impurities from donor or acceptor atoms is that the energy levels they introduce do not lie at the edges of the forbidden band, hence they are “deep” in energy. These deep impurities capture a conduction electron or hole for a certain period of time, eventually releasing it according to a relaxation time constant. For Ge at 77K, this time constant is much longer than the duration of the signal from the detection event ( $\sim 500\text{ns}$ ) effectively removing the trapped charge from the event. The probability of trapping taking place shows a sharp temperature dependence and detectors subjected to high neutron fluxes should be kept below 100K [53] in order to minimise the loss of energy resolution. The charge lost due to trapping is reflected in a detected lower energy “tail” just below the full peak energy  $E_\gamma$ . In a  $\gamma$ -ray detector, lattice dislocations can be due to fast neutrons or protons. These trapping centres can be removed by annealing the crystal.

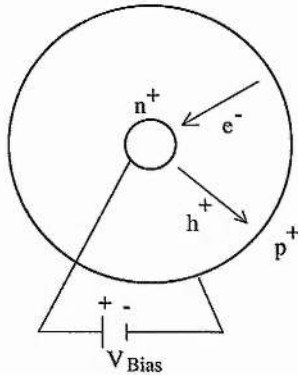


Figure 2.6: Schematic view of a  $n$ -type germanium detector with the corresponding charge carriers drift velocities.

#### 2.4.1 Gamma-Ray Arrays: GAMMASPHERE

At present a number of different Gamma-Ray Arrays already exist or are under construction. All of them rely on Compton suppression shielding to enhance the Peak-to-Total (P/T) ratio. BGO is widely used for Compton suppression shielding. Some of the most important arrays are GASP [54], EUROBALL [55], GAMMASPHERE [56] and EXOGAM [57]. These spectrometers have been developed over a period of time and their properties have evolved to take account of new developments. The absolute photopeak efficiency of all of these arrays is relatively low ( $\leq 10\%$  at 1.3 MeV) mainly due to the physical gaps between the active germanium detectors and the BGO which is placed between the active Germanium crystals as suppression shielding. It is for this reason that the new  $\gamma$ -ray tracking concept enters and is destined to play an important role (this topic will be discussed in the APPENDIX A to this thesis).

GAMMASPHERE [56] in its full compliment consists of a spherical shell of 110 large volume, high-purity germanium detectors, each enclosed in a bismuth-germanate Compton-suppression shield in a symmetric geometry. Seventy of the detectors have been electrically segmented into D-shaped halves [58], to improve the determination of the interaction position of the photon in the detector (see Fig. 2.7).

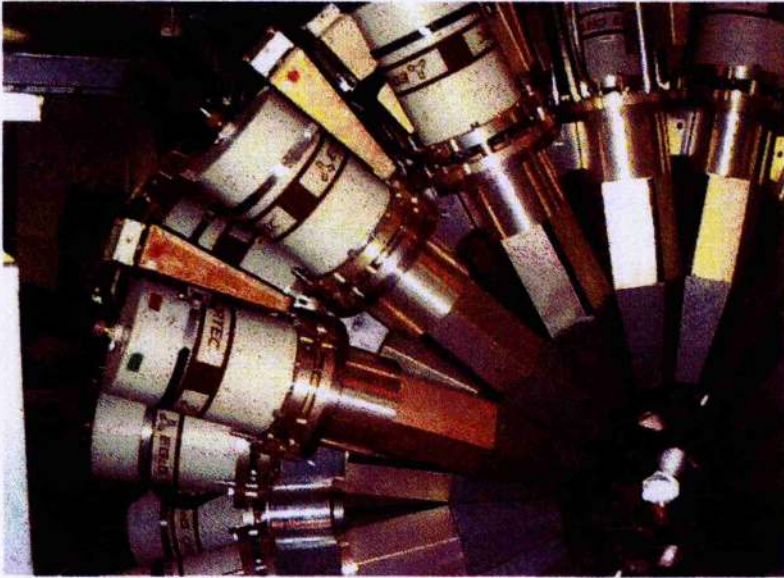


Figure 2.7: Picture showing a quarter of GAMMASPHERE.

### 2.4.2 Doppler Shift and Doppler Broadening Correction

If the precise position of the  $\gamma$  interaction within the detector can not be determined, the uncertainty in the detection angles is limited by the solid angle covered by the detector. When a nucleus travels at velocity  $\beta = v/c$ , where  $c$  is the velocity of light in vacuum, the observed energy,  $E_s$ , in the laboratory frame of a  $\gamma$  ray emitted by a nucleus is subjected to a Doppler shift [59] according to

$$E_s = E_0 \frac{\sqrt{1 - \beta^2}}{1 - \beta \cos \theta} \approx E_0(1 + \beta \cos \theta) \quad (2.45)$$

where  $E_0$  is the energy in the rest frame of the nucleus and  $\theta$  is the emission angle relative to the trajectory of the nucleus in the laboratory frame, see Fig. 2.8. The approximation made is only valid for  $\beta \leq 0.05$ .

The  $\gamma$ -ray energy is Doppler shifted depending on the angle between the nucleus and the  $\gamma$  ray emitted and according to the fact that the germanium detectors have a certain opening angle  $\Delta\theta$ . As a result of the uncertainty in  $\theta$  and in the velocity of the recoil  $\beta$ , the observed  $\gamma$ -ray energy shows an energy broadening  $\Delta E_\gamma$  given

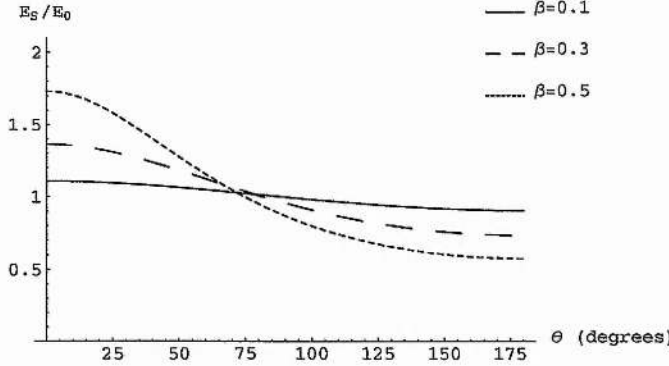


Figure 2.8: Ratio of the energy in the laboratory frame ( $E_s$ ) to energy in the rest frame ( $E_0$ ), versus the laboratory angle  $\theta$ .

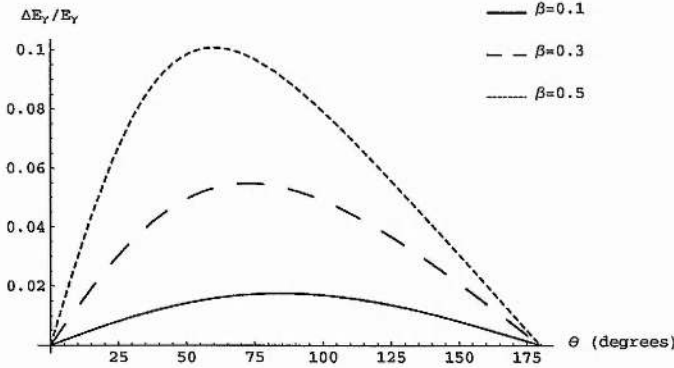


Figure 2.9: Contribution to the energy resolution due to the uncertainty in the scattering angle  $\theta$ , assuming  $\Delta\theta = 10^\circ$ .

by [59]

$$\begin{aligned} \left( \frac{\Delta E_\gamma}{E_\gamma} \right) &= \left( \frac{\beta \sin \theta}{1 - \beta \cos \theta} \right)^2 (\Delta\theta)^2 \\ &- \left( \frac{-\beta + \cos \theta}{(1 - \beta^2)(1 - \beta \cos \theta)} \right)^2 (\Delta\beta)^2 + \frac{(\Delta E_{intr})^2}{(E_\gamma)^2} \end{aligned} \quad (2.46)$$

The above expression includes not only the uncertainty in the photon scattering angle ( $\Delta\theta$ ) but also the effect of a spread in the recoil velocity ( $\Delta\beta$ ) and the effect due to the intrinsic detector resolution ( $\Delta E_{intr}$ ). The contribution of each term can be seen in Figs. 2.9 and 2.10 and the total contribution in Fig. 2.11.

The uncertainty in  $\theta$  can be reduced by electronically segmenting the detectors, thus reducing the Doppler broadening. If a pulse shape analysis is applied (see Refs. [60, 61, 62, 63, 64]), the granularity increases drastically if it is possible to get the

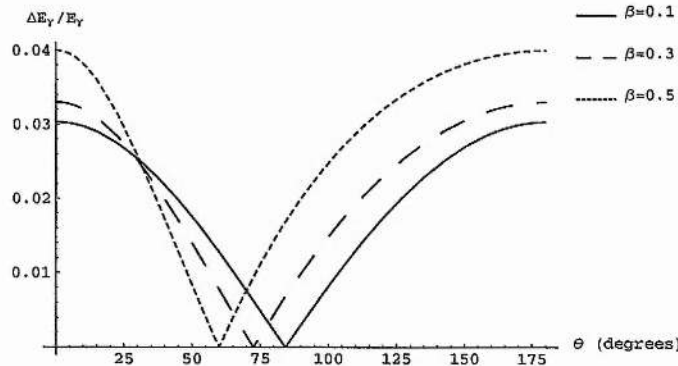


Figure 2.10: Contribution to the energy resolution due to the uncertainty in the beam velocity, assuming  $\Delta\beta = 0.03$ .

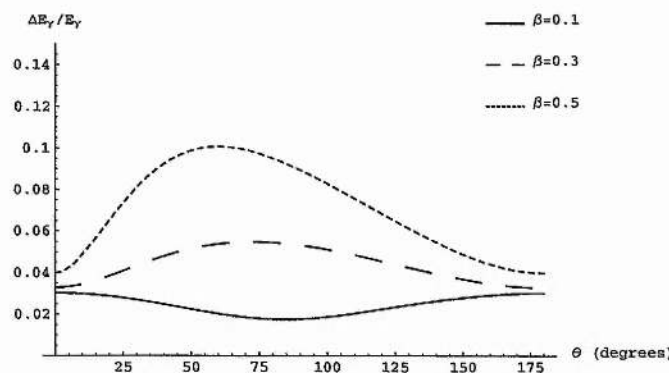


Figure 2.11: The two contributions to the Doppler broadening ( $\Delta\beta$  and  $\Delta\theta$ ) added in quadrature. This plot represents the ultimate energy resolution in an experiment using detectors which have a “perfect” intrinsic energy resolution.

spatial resolution down to 5 mm. These topics are at the heart of the  $\gamma$ -ray tracking concept and they will be discussed in the APPENDIX A to this thesis.

## 2.5 Heavy Ion Detector: CHICO

The CHICO [65] detector consists of 20 separate trapezoidal Parallel Plate Avalanche Counters (PPACs). The essential elements of each PPAC comprise a thin film anode, segmented in two unequal parts, plus a cathode circuit board which is segmented into  $1^\circ$  wide traces of constant polar angle  $\theta$ . There are two identical hemispherical assemblies, each of which houses 10 of the PPACs arranged in a truncated cone coaxial with the beam direction. Figure 2.12 shows one hemisphere of the CHICO detector installed in one half of GAMMASPHERE. The forward assembly, (note that the backward one was not used during the experiment described in this thesis, due to the forward focussed reaction kinematics), has an active  $\theta$  range from  $12^\circ$  to  $85^\circ$ . An individual PPAC covers an azimuthal width of  $28^\circ$  and there is a dead region of  $8^\circ$  in  $\phi$  between each of the PPACs. For the set-up including both hemispheres, this provides  $280^\circ$  of  $\phi$  coverage for both the forward and backward assemblies. The total angular coverage is approximately  $2.8\pi$  sr, corresponding to about 69% of the total solid angle.

CHICO has been designed to measure the azimuthal  $\phi$  and the polar  $\theta$  angles with respect to the beam direction of the scattered nuclei, and the Time-Of-Flight difference ( $\Delta$ TOF).

The azimuthal angle  $\phi$  is measured using the segmentation of the anodes, see Figs. 2.13 and 2.14. To measure  $\phi$  a “binary” scheme [65] was implemented. The anodes are segmented into two sections covering  $1/3$  and  $2/3$  of the total  $\phi$  angle subtended by the individual PPACs. CHICO is used mostly for binary reactions, therefore two-body kinematics demands that the scattered target and beam-like fragments are coplanar to first order (note that the emission of light particles, such as neutrons, will shift the fragments slightly out of plane). The combination of the

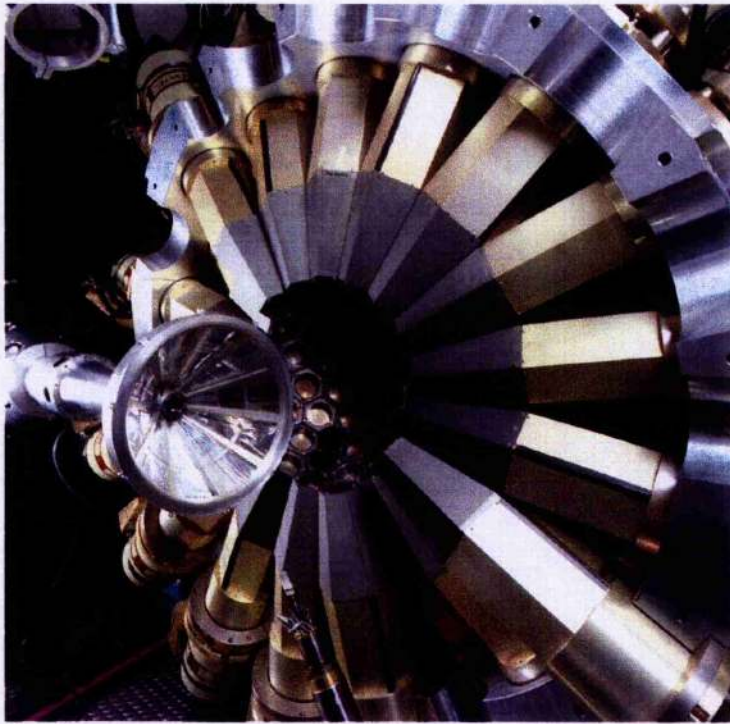


**Figure 2.12:** Sectional view of CHICO within GAMMASPHERE. The target chamber housing the PPACs and the pressure window can be seen. The length of the assembly is 91 cm.

small and large segments in the PPACs define the azimuthal angle  $\phi$ . Figure 2.14 shows the different “shadows” where the coplanar fragments might be detected, thus defining the azimuthal angle. For example if the large section of both anodes trigger, then the reaction plane is in  $\phi$  “shadow” 2. The azimuthal angle  $\phi$  is limited by the angular width of the smaller of the two segments, which is  $9.3^\circ$ .

The polar angle  $\theta$  is measured from the signals read out of the cathode delay line, see Fig. 2.13. The signal generated in the cathode by the incident heavy ion travels in both directions down the delay line. The time difference between the two ends of the line determines the location along the delay line. The angular resolution is about  $1^\circ$ . There is a dip in the count-rate at  $60^\circ$ , due to the shadow of a support rib in the pressure window. This dip provides an internal calibration of the polar angle.

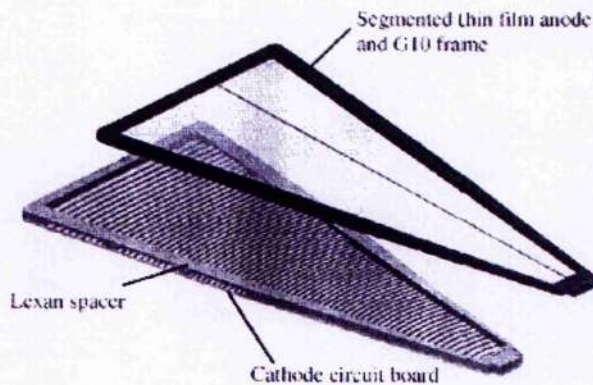


**Figure 2.13:** View of an individual PPAC, taken from [65]. The upper one is the asymmetrically segmented anode and the one below is the cathode board, showing the delay line.

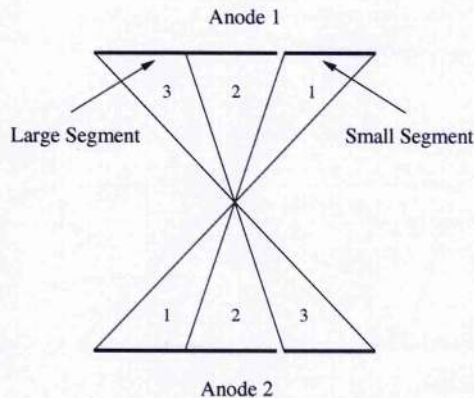


**Figure 2.14:** Segmentation of two coplanar anode pairs.

The  $\Delta\text{TOF}$  is measured using the difference in time between the signals produced by the heavy ions in two coplanar anodes. The time resolution is around 0.7 ns.

For binary reactions it is possible to identify the beam and target-like fragments if they are detected in coincidence, by plotting the scattering angle  $\theta$  versus the  $\Delta\text{TOF}$ . The angular and  $\Delta\text{TOF}$  resolutions are generally sufficient to distinguish between the beam and the target-like fragments.

# Chapter 3

## Analysis of the GAMMASPHERE-CHICO Data

### 3.1 Experimental Procedure

The experiment described in the following pages was performed at Lawrence Berkeley National Laboratory in April 2002. An 850-MeV  $^{136}_{54}\text{Xe}$  beam provided by the 88" cyclotron with an on-target intensity around 1 particle nA, was incident on a thin, ( $420 \mu\text{g cm}^{-2}$ ), self-supporting target of  $^{198}_{78}\text{Pt}$  isotopically enriched to  $> 92\%$ . The Coulomb barrier energy in the laboratory frame for the chosen beam and target was estimated to be,

$$E_{Lab}^{Coulomb} = (1 + A_1/A_2) \frac{1.44Z_1Z_2}{1.16(A_1^{1/3} + A_2^{1/3} + 2)} \approx 680 \text{ MeV} \quad (3.1)$$

The beam energy was chosen to be  $\approx 25\%$  above the Coulomb barrier to enhance the population of high-spin states and had a natural micro-pulsing period of 178 ns. Gamma rays were detected using GAMMASPHERE [56]. The CHICO gas-filled PPAC ancilliary detector [65] was used in combination with GAMMASPHERE to measure the angle of the recoils (both  $\theta$  and  $\phi$ ) and the time-of-flight difference ( $\Delta TOF$ ) between the detection of both recoils.

The experimental master trigger condition required two CHICO elements and at

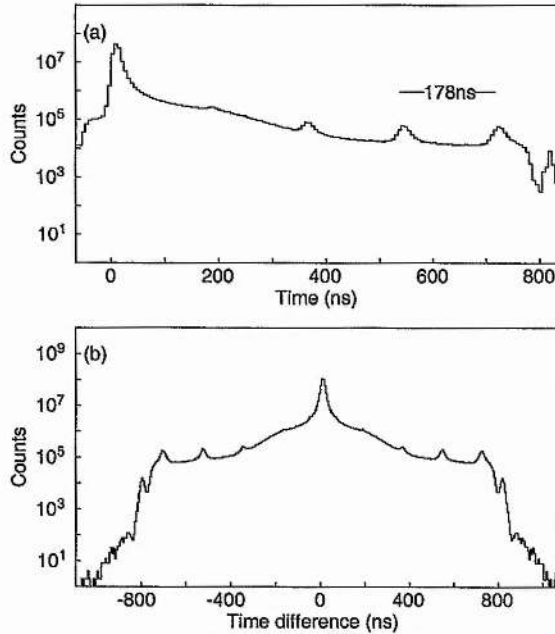


Figure 3.1: Spectrum (a) shows the total time projection of  $\gamma$ -ray events in the current work, note that the time between the cyclotron bursts is 178 ns. Spectrum (b) shows the time difference between pairs of  $\gamma$  rays ( $t_{\gamma_1} - t_{\gamma_2}$ ).

least three germanium detectors to fire. The timing condition was set such that the third (and subsequent) germanium signals could be delayed by up to 670 ns with respect to the first two germanium energies.

During the off-line analysis a software requirement was defined to include only events with at least three prompt  $\gamma$  rays within  $\pm 45$  ns of the binary fragments being detected in CHICO. This allowed a well-defined time reference for all delayed  $\gamma$  rays decaying from isomeric states in the binary fragments to be used in the subsequent analysis. Figure 3.1a shows the sum of time distributions associated with the individual GAMMASPHERE detectors and Fig. 3.1b shows the relative time differences between  $\gamma$  rays measured in coincident events. By setting software gates on these spectra, specific temporal regions could be defined, corresponding to either prompt

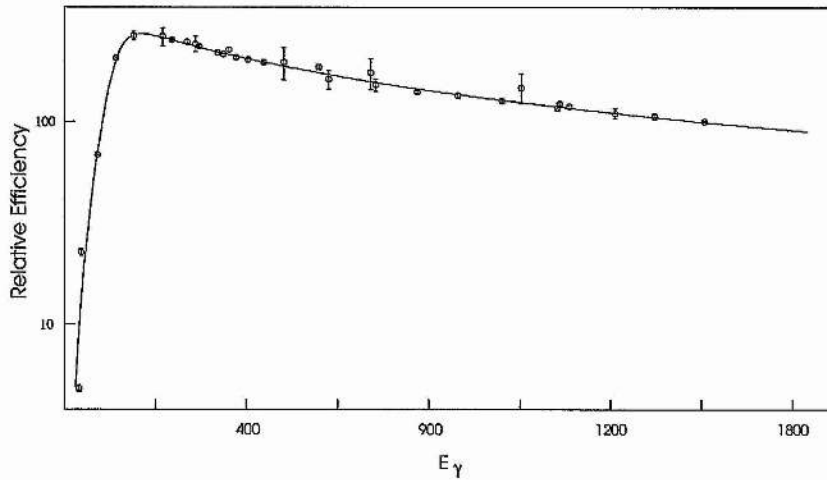


Figure 3.2: Relative efficiency curve for GAMMASPHERE with CHICO. The experimental points correspond to  $^{152}\text{Eu}$  and  $^{133}\text{Ba}$  sources.

$\gamma$  rays which were emitted from the fragments in flight or the decays from isomeric states in nuclei which were stopped in CHICO. The recoiling products stopped in the back of the PPACs, approximately 13 cm from the target position. Subsequent isomeric decays with lifetimes ranging from the nanoseconds to microseconds range were observed with a reasonable efficiency due to the absence of heavy metal collimators on the Ge detectors. The absence of heavy metal collimators also allowed the measurement of the  $\gamma$ -ray fold by recording the number of hits in the BGO elements as well as in the germanium detectors.

### 3.1.1 Efficiency of GAMMASPHERE with CHICO

The energy response of GAMMASPHERE was calibrated using  $^{152}\text{Eu}$  and  $^{133}\text{Ba}$  sources, placed at the target position, inside the reaction chamber of CHICO. CHICO was specifically built using low  $Z$  materials, therefore, the efficiency of the powerful  $\gamma$  array was not significantly degraded by the use of CHICO, see Ref. [65]. The relative efficiency calibration curve obtained is shown in Fig. 3.2.

## 3.2 Data Reduction and Off-line Analysis

### 3.2.1 Particle Identification

As a result of using a thin target, the beam and target-like reaction fragments, BLFs and TLFs respectively, produced in the binary reaction, could be detected using CHICO in coincidence with the  $\gamma$  rays emitted by the nuclei of interest. The  $\Delta\text{TOF}$  measured between the detection of the two fragments and the angular information directly given by the recoil detector allows the separation of the BLFs and TLFs. Figure 3.3 shows the separation between the two binary partners, with the most intense peak lying in the vicinity of the grazing angle [46], which for this particular reaction occurs at the same laboratory angle,  $50^\circ$ , for both the TLFs and BLFs. Figure 3.4 shows the angular correlation of the two coplanar scattered nuclei detected in two opposing PPACs. Figures 3.3 and 3.4 show a cut-off at  $20^\circ$  as a result of the use of a mask to stop the high counting rate at low angles. The reduction in counts in these spectra at  $60^\circ$  occurs as a result of a support rib in the pressure window of CHICO and could be used for internal angular calibration purposes.

Figure 3.3 shows that at low angles for the BLFs distribution and at more backward angles ( $\gtrsim 65^\circ$ ) in the case of the TLFs the statistics decrease abruptly. This does not happen as a result of the reaction mechanism. This effect happens since the TLF recoils at high angles have a low velocity (energy), see Fig. 2.3. These recoils do not always get through the pressure window of CHICO and therefore the detection efficiency of CHICO decreases abruptly at those angles for TLFs. To explain why the efficiency is also very low for BLFs at low angles, even though these recoils have a large velocity (see Fig. 2.3), we recall that the master trigger condition in the experiment required two recoils to be detected in CHICO. The TLFs that are detected at large angles are correlated with the BLFs at low angles (see Equation 2.2), therefore if the TLF recoil at large angles is not detected, then the event is not accepted with the direct consequence of efficiency lost for BLFs (low angles) and TLFs.

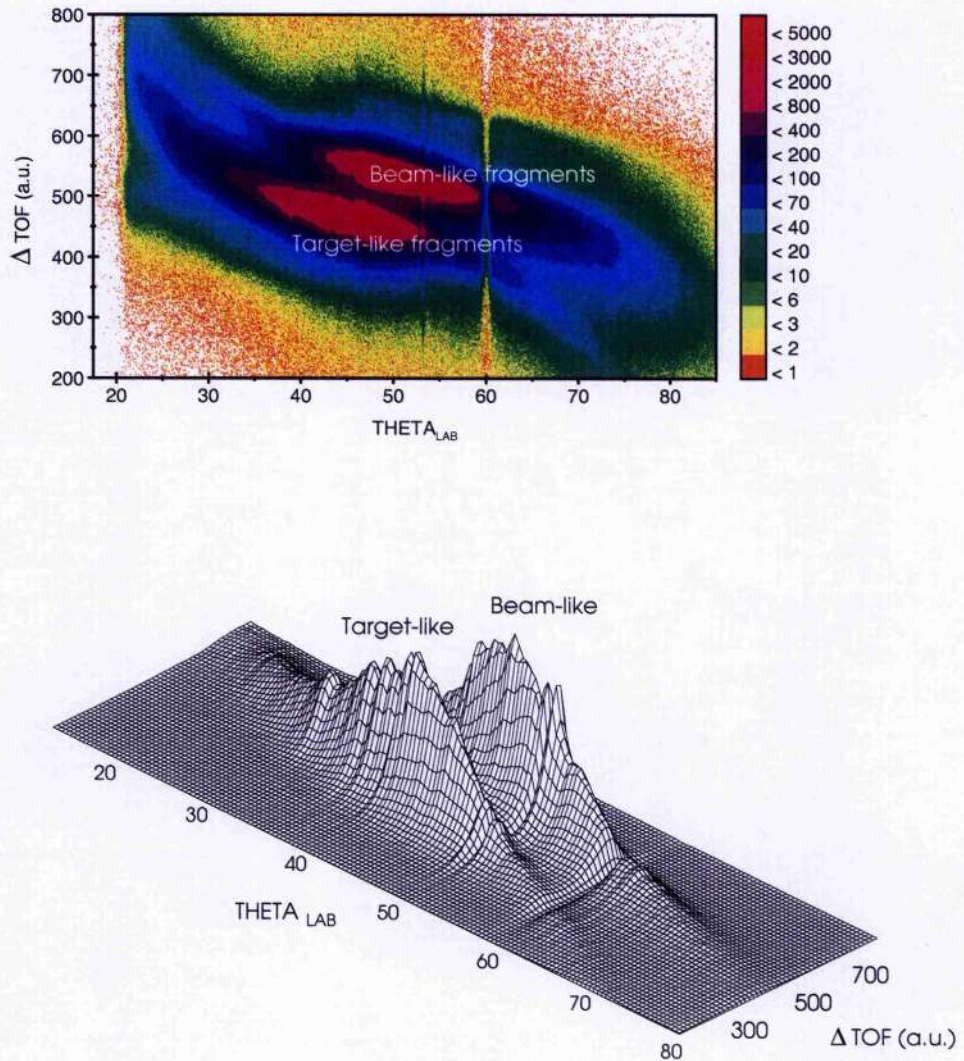


**Figure 3.3:** Particle identification plot for the current work. The measurement of the  $\Delta\text{TOF}$  and scattering angles of the recoils  $\theta$  allows the two binary partners to be cleanly separated.

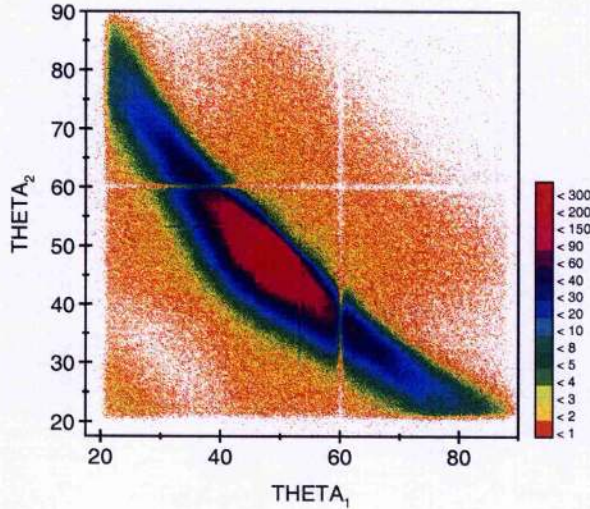


**Figure 3.4:** Angular correlation between the two scattered fragments BLFs and TLFs as measured in CHICO for the reaction of a  $^{136}\text{Xe}$  beam at 850 MeV on a  $^{198}\text{Pt}$  target.

Figure 3.5 shows a two dimensional plot of  $\gamma$ -ray energy versus time relative to the master trigger. For low  $\gamma$ -ray energies one can see the time *jitter* and time *walk* effects [17], indicated by the tail at low energies that extend in time. These effects happen when the number of information carriers that form the signal in the germanium detector is low (*i.e.* for low energy  $\gamma$  rays). Therefore, statistical fluctuations in their number and time of occurrence will also be reflected in the size and shape fluctuations of the pulse in addition to poor charge collection when the interaction happens close to the front contact. The horizontal lines in Fig. 3.5 correspond to the decay of isomeric states.

### 3.2.2 Doppler Correction

The maximum velocities of the binary partners in this reaction are of the order of  $\beta \approx 11\%$ . Therefore the prompt  $\gamma$  rays emitted in flight were heavily Doppler shifted. However, it is possible to correct the prompt  $\gamma$ -ray energies for the Doppler effect on an event-by-event basis using the interaction position of the recoils, as measured by CHICO. Assuming conservation of linear momentum for the

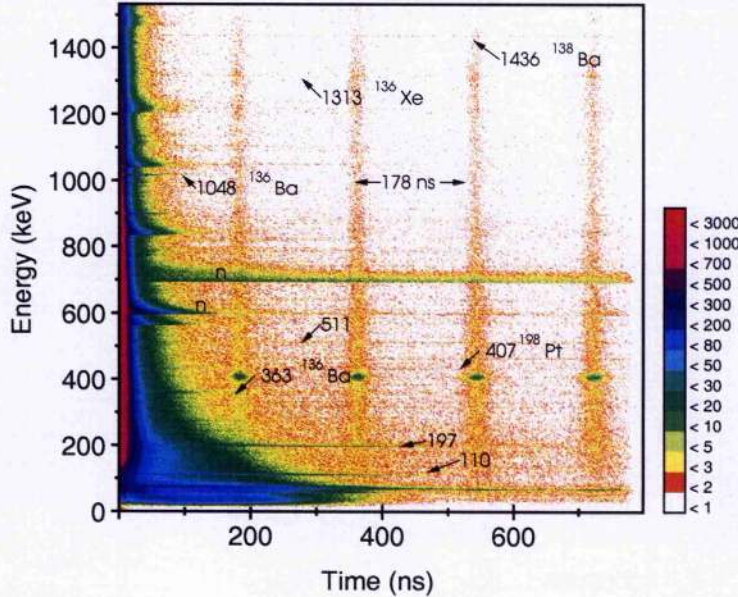


**Figure 3.5:** Two dimensional plot of  $\gamma$ -ray energy versus time relative to the master trigger. The various vertical stripes are the beam pulses, separated by 178 ns. The plot clearly shows the presence of a number of isomeric states (horizontal lines).

scattered beam and target (see previous Chapter),

$$P_{Xe,Pt} = \frac{P_0 \sin(\theta_{Pt,Xe})}{\sin(\theta_{Xe} + \theta_{Pt})} \quad (3.2)$$

where  $P_{Xe} = m_{Xe}\beta_{Xe}c$  and  $P_{Pt} = m_{Pt}\beta_{Pt}c$  are the momenta of the recoiling beam and target nuclei respectively;  $\theta_{Xe}$  and  $\theta_{Pt}$  are the laboratory scattering angles of the recoiling beam and target nuclei respectively and  $P_0$  is the momentum of the incident beam.

The Doppler shifted  $\gamma$  rays are corrected according to [59],

$$E_S = E_0 \frac{\sqrt{1 - \beta^2}}{1 - \beta \cos \Theta} \quad (3.3)$$

where  $E_0$  is the energy in the rest frame of the nucleus and  $\Theta$  is the emission angle relative to the trajectory of the nucleus in the laboratory frame, see Fig. 3.6.

The  $\Theta$  angle can be determined by taking into account the dot product between

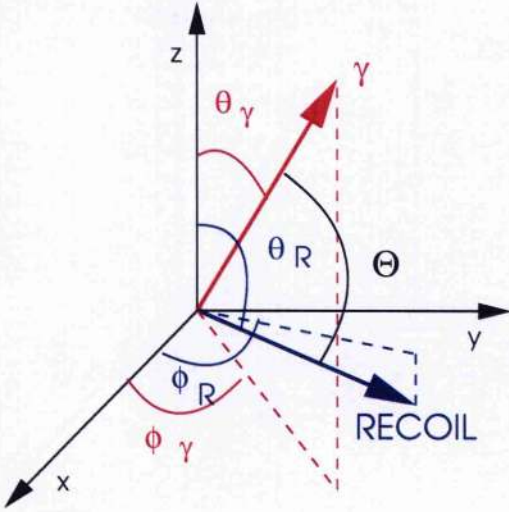


**Figure 3.6:** Schematic view of the angles in spherical coordinates that define the vector position of the recoils and  $\gamma$  rays. It shows the angles involved in the Doppler correction.

the vector position of the recoil ( $\mathbf{r}_R$ ) and  $\gamma$  ray ( $\mathbf{r}_\gamma$ ) in spherical coordinates.

$$\cos \Theta = \frac{\mathbf{r}_R \cdot \mathbf{r}_\gamma}{|\mathbf{r}_R| |\mathbf{r}_\gamma|} \quad (3.4)$$

thus,

$$\cos \Theta = \sin \theta_R \sin \theta_\gamma (\cos \phi_R \cos \phi_\gamma + \sin \phi_R \sin \phi_\gamma) + \cos \theta_R \cos \theta_\gamma \quad (3.5)$$

where  $\theta_R$  and  $\phi_R$  are the scattering angles of the recoils (BLFs and TLFs) and  $\theta_\gamma$  and  $\phi_\gamma$  are the detection angles of the  $\gamma$  rays in GAMMASPHERE. The polar angle  $\theta$  for GAMMASPHERE are listed in Table 3.1.

The  $\gamma$ -ray energies as measured in the laboratory frame can thus be Doppler corrected for the BLFs or TLFs. Note that in each case only the  $\gamma$  rays emitted by the nuclei for which the Doppler correction is made are enhanced in the resulting spectrum, while those with the incorrect Doppler correction will be smeared out (see Fig. 3.7). This technique provides a powerful way of separating the  $\gamma$  rays emitted from the BLFs and TLFs.

Figure 3.7a shows the prompt  $\gamma$  rays which were measured to be within  $\Delta t = \pm 45\text{ ns}$  of the master trigger, with no Doppler correction applied. Figures 3.7b and c show

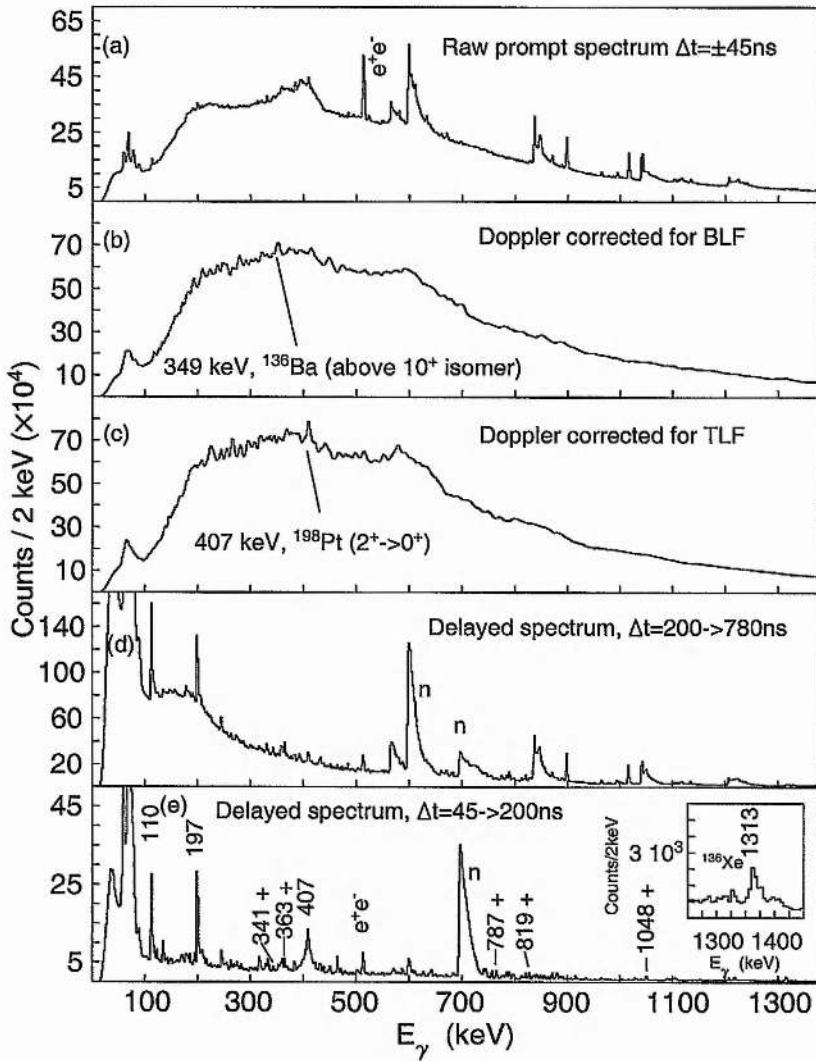


Figure 3.7: Spectrum (a) shows prompt  $\gamma$  rays without any Doppler correction, spectra (b) and (c) show the total projection of prompt Doppler corrected spectra for BLFs and TLFs respectively. The two lower spectra show delayed spectra for two different time ranges. (d) shows delayed  $\gamma$  rays emitted within the time range 200 ns to 780 ns, while (e) shows  $\gamma$  rays emitted within the first 200 ns following the CHICO fragments detection. The peaks marked with a + symbol are  $^{136}\text{Ba}$   $\gamma$  rays which feed into the  $10^+$  isomer.

Table 3.1: Polar angle  $\theta$  for the different rings of the  $\gamma$ -array GAMMASPHERE and the number of working detectors in each ring.

$\theta$ (degrees)	# detectors	$\theta$ (degrees)	# detectors
Forward angles		Backward angles	
17.27	1	99.29	5
31.72	5	100.81	5
37.38	4	110.18	10
50.07	9	121.72	5
58.28	5	129.93	10
69.82	10	142.62	5
79.19	5	148.28	5
80.71	4	162.73	5
90.00	9		

the same spectra Doppler corrected for BLFs and TLFs respectively. Note that the BLF Doppler corrected spectrum (3.7b) shows the prompt 349-keV transition which feeds the  $10^+$  isomer in  $^{136}\text{Ba}$  (see later), while in the TLF Doppler corrected spectrum the 407-keV transition ( $2^+ \rightarrow 0^+$ ) in  $^{198}\text{Pt}$  [66] can be identified. The low-lying prompt transitions from the  $^{136}\text{Xe}$  beam nucleus (*e.g.*,  $E(2^+ \rightarrow 0^+) = 1313$  keV) are not obviously evident in Fig. 3.7b due to the presence of a low-lying  $I^\pi = 6^+$ ,  $t_{1/2} = 3\ \mu\text{s}$  isomeric state in this nucleus [67], which traps most of the prompt feeding.

Figures 3.7d and e show delayed  $\gamma$  rays gated in two different time regimes. Figure 3.7d shows  $\gamma$  rays emitted within the time range 200 ns to 780 ns, while Fig. 3.7e shows  $\gamma$  rays within the first 200 ns of the detection of the binary fragments in CHICO. The latter shows transitions associated with the low-lying states of  $^{136}\text{Ba}$  [68] (see later), the  $2^+ \rightarrow 0^+$  in  $^{198}\text{Pt}$  (407 keV) and the delayed neutron peaks at 596 keV and 691 keV coming from inelastic neutron scattering excitations of  $^{74}\text{Ge}$  and  $^{72}\text{Ge}$  respectively. The two very intense peaks at 110 keV and 197 keV are due

to the  $\gamma$  decay of the  $\frac{5}{2}^+$  state in  $^{19}\text{F}$ , with a half-life  $t_{1/2} = 89.3$  ns [66], which is used in the electrical segmentation process of the HPGe detectors.

### 3.2.3 Pseudo Q-value of the Reaction

Since it is not possible to identify event by event the isotope detected in CHICO, the exact Q-value of the reaction can not be calculated as defined in *Chapter 2*. Instead a pseudo Q-value can be calculated, according to,

$$Q\text{-value}_{pseudo} = \frac{P_t^2}{2m_{Pt}} + \frac{P_p^2}{2m_{Xe}} - \frac{P_0^2}{2m_{Xe}} \quad (3.6)$$

where the specific masses of the scattering BLFs and TLFs have been replaced by the beam  $^{136}\text{Xe}$  and target  $^{198}\text{Pt}$  mass respectively. The momenta  $P_p$  and  $P_t$  are obtained using Equation 3.2.

In Figure 3.8 the pseudo Q-value of the reaction is plotted versus the scattering angle  $\theta$  of the BLFs and TLFs. These two plots have some common characteristics. Firstly the total energy surface that is defined in both cases by a diagonal line going from top-right to bottom-left. This line appears as a result of the energy conservation in the reaction. Thus, in the case of TLFs for more and more inelastic processes, where Q is larger, the scattering angle decreases as a direct consequence. Deep-inelastic reactions begin to occur around the grazing angle and for larger laboratory angles in the case of the BLFs and to smaller angles in the case of TLFs. The events that have pseudo Q-values  $\approx 0$  correspond to Coulomb or quasi-elastic channels in the reaction.

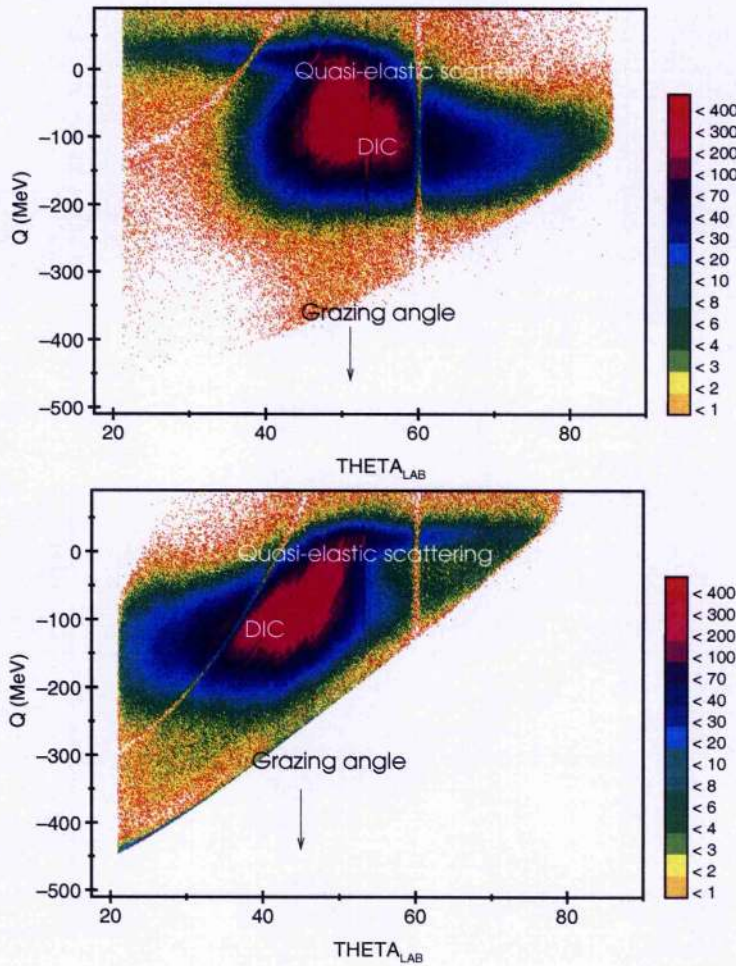


Figure 3.8: Pseudo Q-value versus  $\theta$  gated for BLFs (upper spectrum) and for TLFs (lower spectrum), for the reaction 850 MeV  $^{136}\text{Xe}$  beam,  $^{198}\text{Pt}$  target.

### 3.2.4 Gamma-Ray Fold

In its full complement GAMMASPHERE has a total of 110 HPGe detectors all of which are Compton suppressed, *i.e.* each is surrounded by a high  $Z$ , high density Bismuth Germanate Oxide (BGO) shielding. This shielding improves the Peak-to-Total ratio by reducing the Compton background, but at the same time it can also be used to measure the  $\gamma$ -ray fold for each event. It is possible to derive an estimate of the total  $\gamma$ -ray multiplicity from the measured fold using standard calibration

procedures [69].

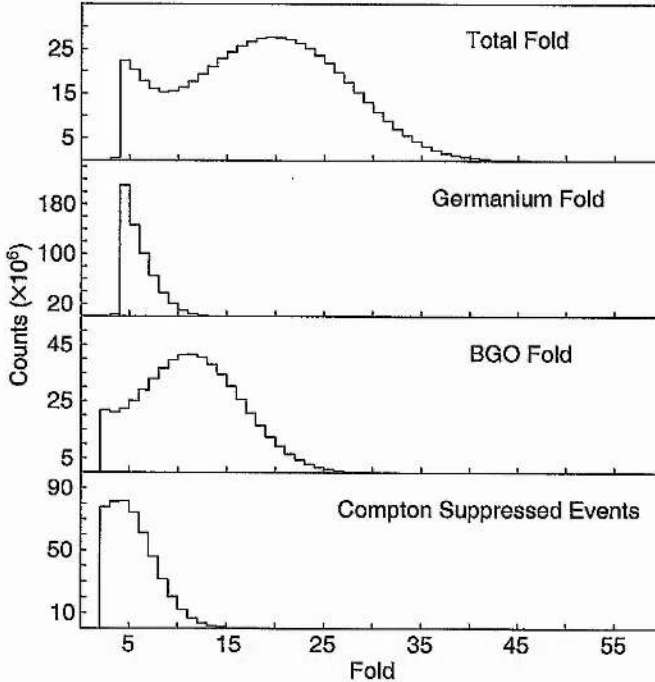


Figure 3.9: Total Fold measured in the reaction (top), lower panels show the different contributions. Note that the total fold ( $F_{tot}$ ) shown in the upper panel is not the direct sum of the three lower panels but the addition of the three contributions ( $F_{BGO}$ ,  $F_{HPGe}$ ,  $F_{CS}$ ) event by event (see text).

The total fold,  $F_{tot}$ , measured in each event was the result of adding the following contributions (see Fig. 3.9),

$$F_{tot} = F_{BGO} + F_{HPGe} + F_{CS} \quad (3.7)$$

where  $F_{BGO}$  is the number of counts detected per event in all the BGO shieldings,  $F_{HPGe}$  is the number of  $\gamma$  rays detected in all the germanium detectors and  $F_{CS}$  are the  $\gamma$  rays that have been Compton suppressed, *i.e.*  $\gamma$  rays that Compton scattered out of the germanium and were detected in the HPGe detector in coincidence with its BGO shielding.

### 3.2.5 Description of Matrix and Cube Analysis

The analysis of these data required a number of different coincidence matrices and cubes to be sorted, which were subsequently analysed using the radware [70] and Ana [71] packages. Those of relevance to the present work are listed in Table 3.2.

Table 3.2: List of the different matrices and cubes used in the analysis of the present work.

Id	Description	Time Gate ( $\Delta t$ [ns])			Additional Conditions
		x-axis	y-axis	z-axis	
I	$\gamma - \gamma$ delayed matrix	45 → 780	45 → 780		
II	$\gamma - \gamma - time$ cube				$t_{\gamma_1} - t_{\gamma_2} = 5$ ns (see Fig. 3.1)
III	$\gamma_{delayed} - \gamma_{prompt} - \Delta t$ cube <sup>a</sup>	45 → 780	±45		$\gamma_{prompt}$ gated on BLFs
IV	$\gamma - \gamma$ prompt matrix <sup>b</sup>	±45	±45		341, 363, 787, 819, 1048 (keV) <sup>c</sup>
V	$\gamma_{delayed} - \gamma_{prompt}$	45 → 780	±45		$\gamma_{prompt}$ gated on BLFs and TLFs
VI	$\gamma_{delayed} - \gamma_{prompt} - \theta_{ring}$ cube <sup>d</sup>	45 → 780	±45		$\gamma_{prompt}$ gated on BLFs
VII	$\gamma_{delayed} - \gamma_{prompt} - \gamma_{prompt}$ cube	45 → 780	±45	±45	$\gamma_{prompt}$ gated on TLFs
VIII	$\gamma_{delayed} - \theta_{scatt} - Fold$ cube <sup>e</sup>	45 → 780			

<sup>a</sup>  $\Delta t$  is defined as  $t_{delayed} - t_{prompt}$ .

<sup>b</sup> Doppler corrected for BLFs.

<sup>c</sup> Delayed  $\gamma$  rays in  $^{136}\text{Ba}$ .

<sup>d</sup>  $\theta_{ring}$  are the polar angles for GAMMASPHERE, see Table 3.1.

<sup>e</sup>  $\theta_{scatt}$  is the scattering angle of the BLFs or TLFs measured by CHICO.

# Chapter 4

## Results and Discussion

### 4.1 Isomers Populated

A large number of isomeric states populated in the reaction (850 MeV  $^{136}\text{Xe}$  beam,  $^{198}\text{Pt}$  target) have been identified in the beam and target-like regions. Figure 4.1 shows the different isomers populated that range from  $^{118}_{50}\text{Sn}$  to  $^{140}_{58}\text{Ce}$  for BLFs while for TLFs the isomers range from  $^{180}_{73}\text{Ta}$  to  $^{206}_{84}\text{Po}$ . This figure also shows the  $N/Z$  equilibration line for the BLFs and TLFs. The majority of nuclei populated in the reaction lie above the  $N/Z$  equilibration line, while not many nuclei have been populated below the  $N/Z$  equilibration line. A number of previously unreported isomers populated in the target-like region have been observed in  $^{201}\text{Tl}$ ,  $^{195}\text{Au}$ ,  $^{198}\text{Pt}$ ,  $^{194}\text{Os}$ ,  $^{192}\text{Os}$ ,  $^{191}\text{Os}$  and  $^{184}\text{W}$ , while new isomers populated in the beam-like region include those in  $^{139}\text{La}$ ,  $^{136}\text{Ba}$ ,  $^{131}\text{I}$ ,  $^{133}\text{I}$  and  $^{127}\text{Sb}$ . The following sections will concentrate mainly on the structure of  $^{136}_{56}\text{Ba}$ ,  $^{184}_{74}\text{W}$ ,  $^{198}_{78}\text{Pt}$  and  $^{194}_{76}\text{Os}$ .

Figures 4.2 and 4.3 show the background subtracted  $\gamma$ -ray spectra for some selected isomers populated in the beam-like and target-like regions respectively. Also shown are the fitted half-life curves for those decays. Figures 4.4 and 4.5 show the background subtracted  $\gamma$ -ray spectra for some isomers in the beam-like and target-like regions whose exact half-lives could not be determined but it was possible to put a limit to their half-lives. The experimental set-up used was sensitive to half-lives

## Chapter 4. Results and Discussion

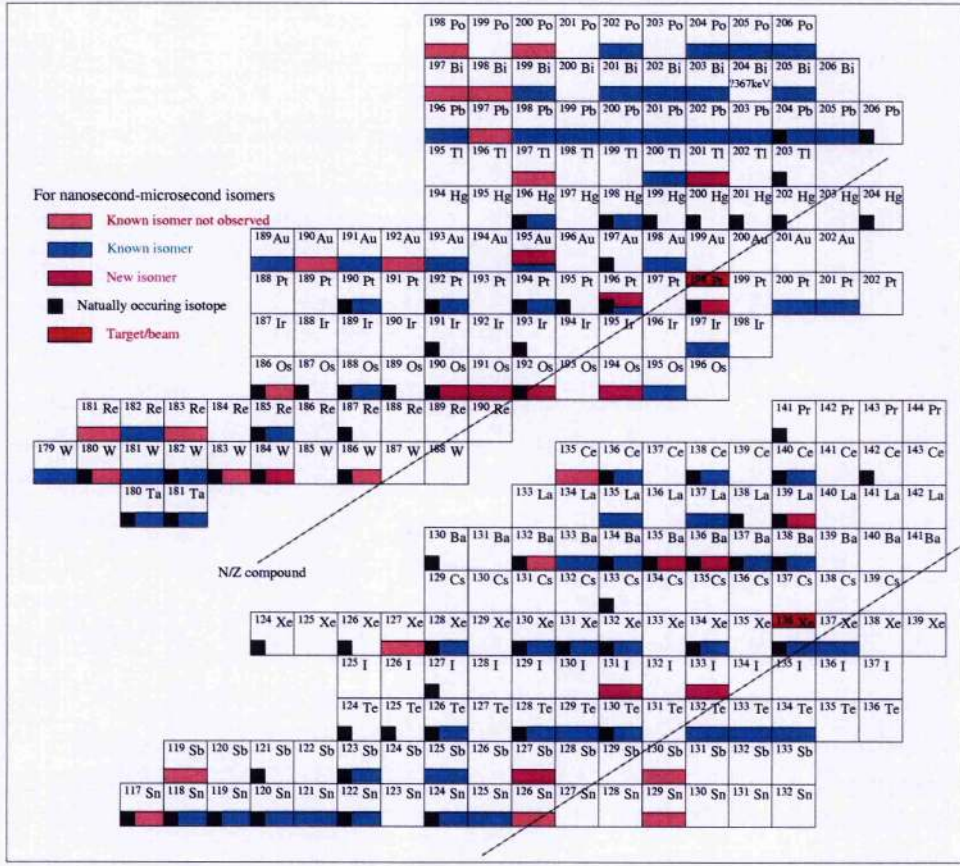


**Figure 4.1:** Summary of isomers identified in the reaction (850 MeV  $^{136}\text{Xe}$  beam,  $^{198}\text{Pt}$  target). The  $N/Z$  equilibration line has been plotted for both BLFs and TLFs. Note that the isomers marked in magenta (colour code), are newly observed isomers.

ranging from a few tens of  $ns$  to around 1  $\mu\text{s}$ . Figure 4.6 shows two characteristic time spectra for nuclei where a half-life could not be measured due to low statistics, or because the half-life was too short or too long. A lower limit of 1  $\mu\text{s}$  was put for  $^{139}\text{La}$  and an upper limit of 110 ns was obtained for  $^{190}\text{Os}$ . Table 4.1 summarizes the half-lives for all the identified isomers. For those previously reported, a comparison with values in the literature is made. The agreement of the measured half-lives with those previously reported supports the reliability of this analysis.

**Table 4.1:** Half-lives of the isomers measured in the present work and a comparison with previous works.

Isotope	$J^\pi$	$E_x$ (keV)	$t_{1/2}$ (ns)	
			Current work	Previous works
$^{127}\text{Sb}$		2326	< 1000	
$^{128}\text{Te}$	$10^+$	2791	$337 \pm 59$	$370 \pm 30$ [72]
$^{130}\text{Te}$	$(7^-)$	2146	$186 \pm 11$	$115 \pm 8$ [73]
$^{131}\text{I}$		2352	$43 \pm 1$	
$^{133}\text{I}$		2436	$780 \pm 160$	
$^{132}\text{Xe}$	$7^-$	2214	$86 \pm 3$	$90 \pm 10$ [74]
$^{136}\text{Xe}$	$6^+$	1892		$3000 \pm 300$ [67]
$^{136}\text{Ba}$	$10^+$	3357	$91 \pm 2$	
$^{138}\text{Ba}$	$6^+$	2091	$1250 \pm 250$	$800 \pm 100$ [75]
$^{137}\text{La}$	$\frac{19}{2}^-$	1870	$342 \pm 25$	$360 \pm 40$ [76]
$^{139}\text{La}$		1712	> 1000	
$^{184}\text{W}$	$(15^-)$	3714	$188 \pm 38$	
$^{185}\text{Re}$	$(\frac{21}{2}^-)$	2124	$164 \pm 10$	$120 \pm 15$ [77]
$^{190}\text{Os}$		(1666)	< 110	
$^{191}\text{Os}$		2640	$61 \pm 4$	
$^{192}\text{Os}$		4115	$190 \pm 96$	
$^{194}\text{Os}$	$(10^+)$	2540	< 90	
$^{195}\text{Os}$	$(\frac{27}{2}^-)$	2229	$26 \pm 9$	$26 \pm 2$ [79]
$^{192}\text{Pt}$	$(10^-)$	2172	$235 \pm 47$	$250 \pm 30$ [80]
$^{196}\text{Pt}$	$(12)$	(3304)	< 50	
$^{198}\text{Pt}$	$(12)$	3019	$36 \pm 2$	
$^{193}\text{Au}$	$\frac{31}{2}^+$	2486	$165 \pm 12$	$150 \pm 50$ [81]
$^{195}\text{Au}$		2294	< 50	
$^{201}\text{Tl}$	$(\frac{15}{2}^+)$	1962	< 60	

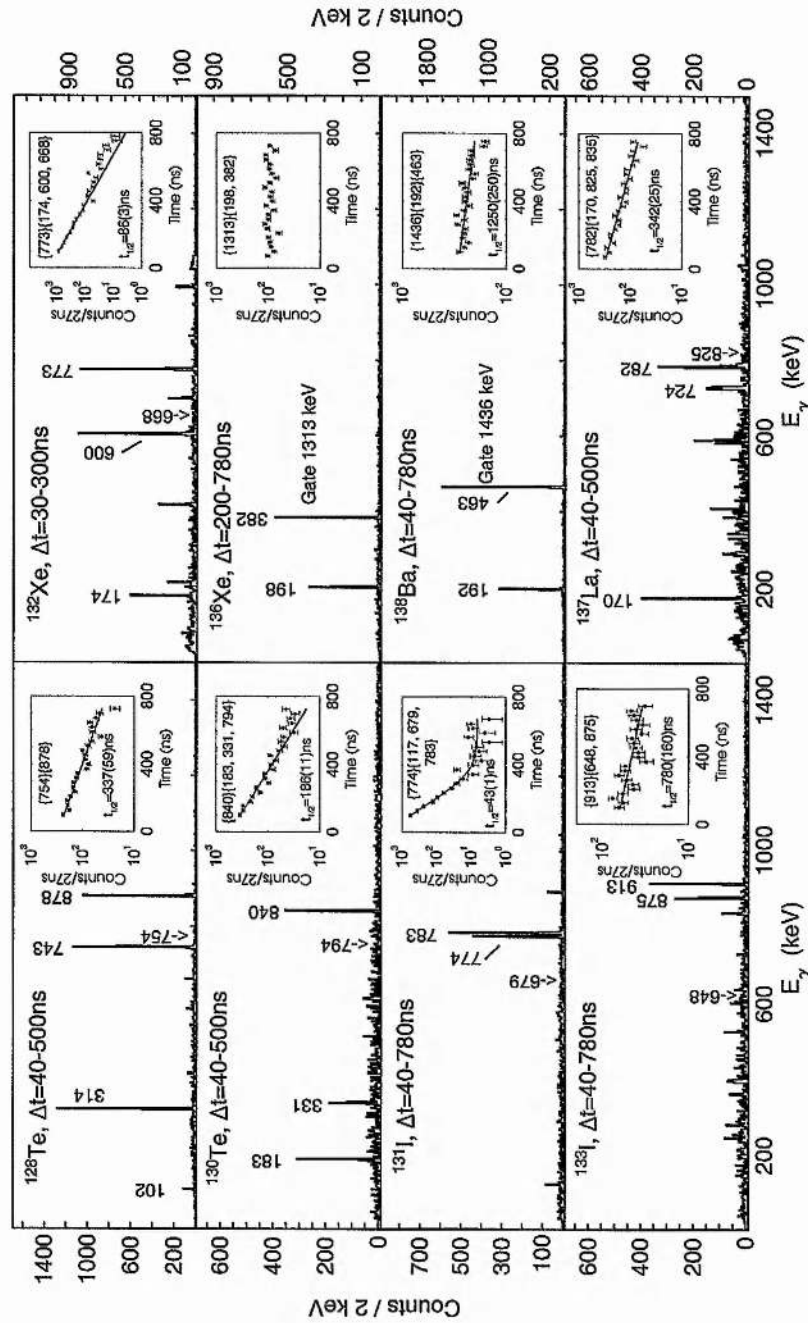


Figure 4.2: Background subtracted  $\gamma$ -ray spectra for selected isomeric states in BLFs populated in the reaction  $^{136}\text{Xe}$  beam at 850 MeV impinging on a  $^{198}\text{Pt}$  target. The insets show the fitted half-life curves obtained in this work and the pairs of double  $\gamma$ -ray gates used to obtain the half-life curve are given in braces. The isomers identified in  $^{131}\text{I}$  and  $^{133}\text{I}$  have not previously been reported.

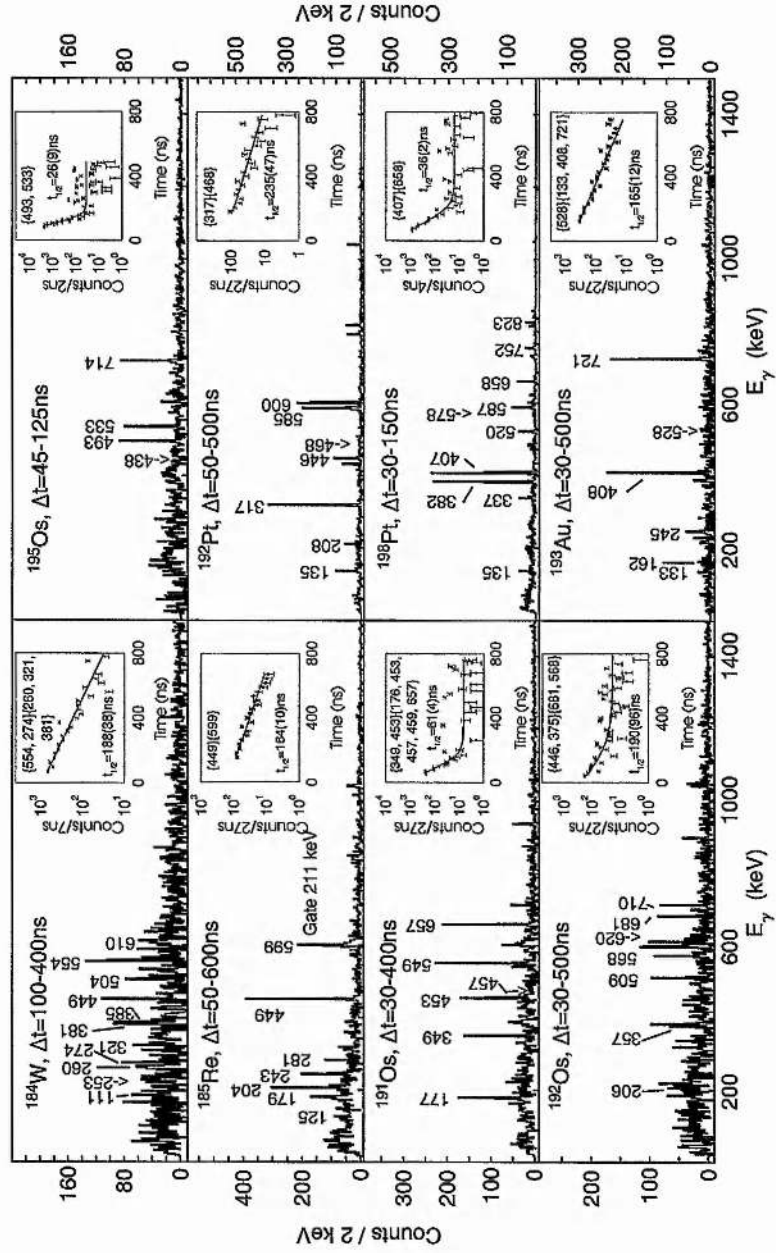


Figure 4.3: Background subtracted  $\gamma$ -ray spectra for selected isomeric states in TLFs populated in the reaction  $^{136}\text{Xe}$  beam at 850 MeV impinging on a  $^{198}\text{Pt}$  target. The insets show the fitted half-life curves obtained in this work and the pairs of double  $\gamma$ -ray gates used to obtain the half-life curve are given in braces. The isomers identified in  $^{184}\text{W}$ ,  $^{191}\text{Os}$ ,  $^{192}\text{Os}$  and  $^{198}\text{Pt}$  have not previously been reported.

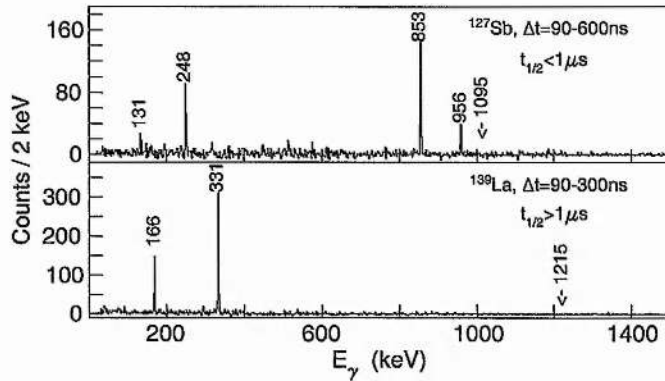


Figure 4.4: Background subtracted  $\gamma$ -ray spectra for selected isomeric states in BLFs populated in this reaction. A limit on the half-life has been obtained for each of the reported isomers.

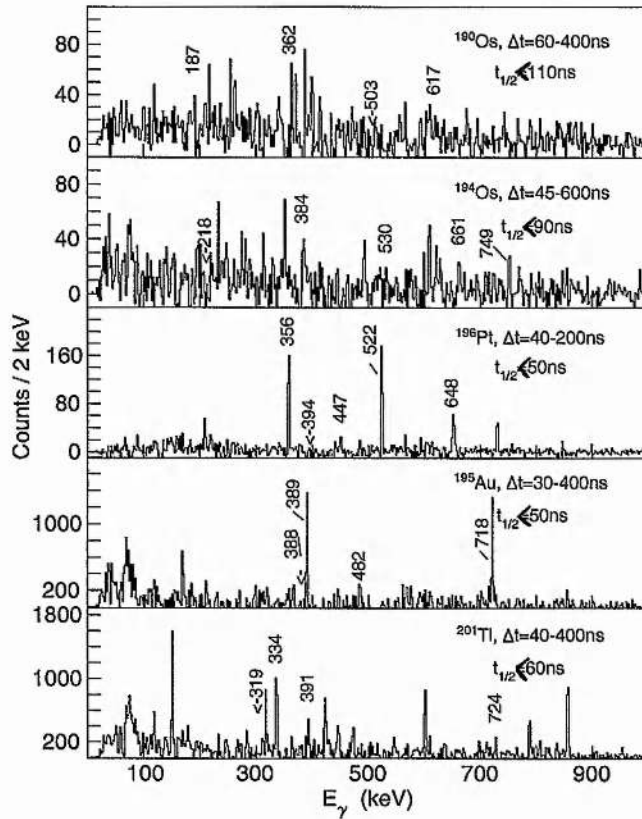


Figure 4.5: Background subtracted  $\gamma$ -ray spectra for selected isomeric states in TLFs populated in this reaction. A limit on the half-life has been obtained for each of the reported isomers.

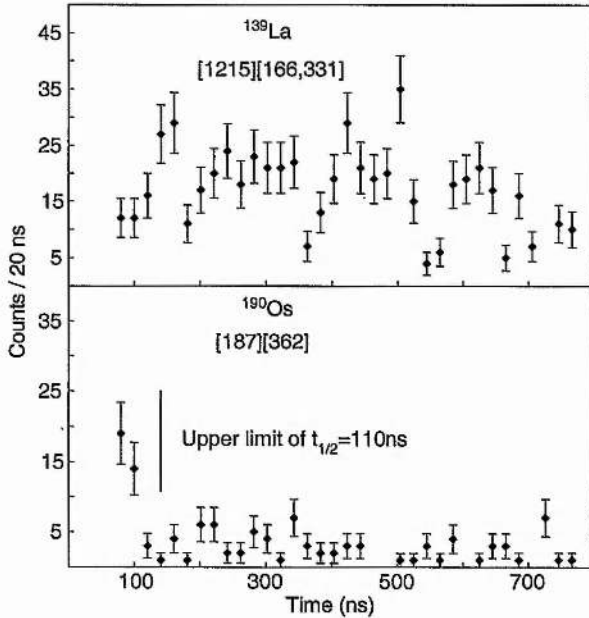


Figure 4.6: Gamma-ray decay curves for the isomers identified in  $^{139}\text{La}$  (upper) and  $^{190}\text{Os}$  (lower). Due to experimental constraints precise values for the half-lives could not be obtained but limits of  $t_{1/2} > 1 \mu\text{s}$  and  $t_{1/2} < 110 \text{ ns}$  respectively have been estimated.

## 4.2 Isomeric $(\nu h_{\frac{11}{2}})^{-2}_{10^+}$ State in $^{136}_{56}\text{Ba}$

Nuclei in the vicinity of the doubly-closed-shell nucleus  $^{132}_{50}\text{Sn}_{82}$  [82] give information on the basic single particle structure and interactions between pairs of nucleons occupying the valence states. In particular, the evolution of structure in the  $N = 80$  isotones can be used to identify the pertinent role of the unnatural-parity  $h_{\frac{11}{2}}$  neutron orbital which has a major influence on the make-up of the high-spin states in this region. Isomeric  $I^\pi = 10^+$  states have been reported in all the even- $A$ ,  $N = 80$  isotones from  $^{130}_{50}\text{Sn}$  up to  $^{148}_{68}\text{Er}$  [83, 84, 85, 86, 87, 88], with the exception of the  $Z = 56$  isotope,  $^{136}_{56}\text{Ba}$ . In the recent paper by Genevey *et al.*, [84] the significant reduction of the  $B(E2)$  between the yrast  $10^+$  isomeric state and the first  $8^+$  state in the  $Z \geq 58$ ,  $N = 80$  isotones [85, 86, 87, 88] compared to their  $Z \leq 54$  counterparts [83, 84] has been discussed in terms of a significant component

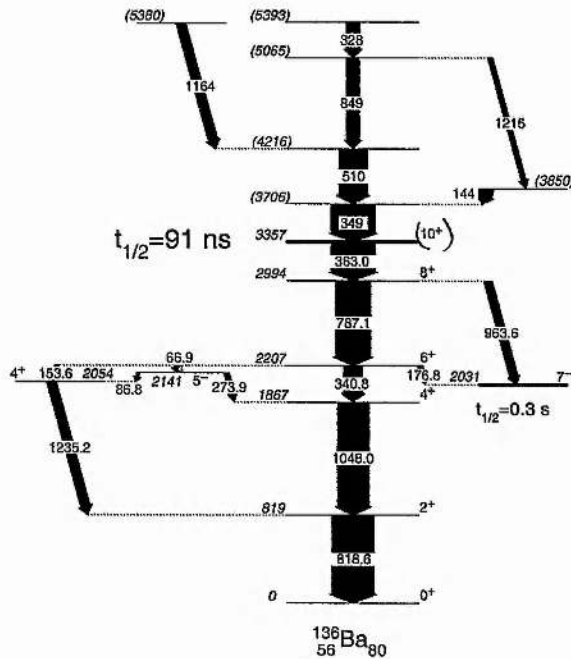


Figure 4.7: Level scheme of  $^{136}\text{Ba}$  deduced from the present work with the  $91 \pm 2$  ns  $I^\pi = 10^+$  isomer. The widths of the arrows are proportional to the relative  $\gamma$ -ray intensities. Note that all the energies are given in keV.

of the neutron  $(\nu h_{\frac{11}{2}})^{-2}$  configuration in the wavefunction of the  $8^+$  state in the lighter systems.

The magnetic moment measurements of the yrast  $I^\pi = 10^+$  isomers in  $^{138}_{58}\text{Ce}$  and  $^{140}_{60}\text{Nd}$  [86] are all consistent with near-spherical, maximally-aligned two neutron-hole,  $(\nu h_{\frac{11}{2}})^{-2}$  configurations. Similar, two-neutron-hole  $I^\pi = 10^+$  states have also been observed in the lighter barium isotopes,  $^{132}_{56}\text{Ba}$  [89] and  $^{134}_{56}\text{Ba}$  [90].

Prior to this study, the medium-to-high-spin data on  $^{136}\text{Ba}$  were restricted due to the  $\beta$ -stable nature of  $^{136}\text{Ba}$ , which makes it difficult to populate with heavy-ion induced fusion-evaporation reactions. The  $N = 80$  isotone lies between the lighter barium isotopes which can be readily populated using this method [91] and heavier, neutron-rich isotopes which have been studied as residues from spontaneous fission [92, 93, 94]. To date, the data on the near-yrast states in  $^{136}\text{Ba}$  comes from work using  $\beta$  decay [95],  $(n, \gamma)$  reactions [68], Coulomb excitation [96] and light-ion ( $^9\text{Be}$ )

induced fusion reactions [97]. As a result, prior to this work, the highest spin state known was the yrast  $8^+$  state identified by Dragulescu *et al.* [97].

The level scheme deduced from the present work for  $^{136}\text{Ba}$  is shown in Fig. 4.7 and was obtained by examining background subtracted spectra from:

- i) an out-of-beam matrix, constructed from delayed  $\gamma - \gamma$  coincidences (see Table 3.2) for the levels below the the  $10^+$  isomer.
- ii) an in-beam prompt matrix, constructed from  $\gamma - \gamma$  coincidences gated on delayed transitions in  $^{136}\text{Ba}$  and Doppler corrected for the BLFs (see Table 3.2). This enabled the identification of prompt transitions which feed the  $10^+$  isomer.
- iii) a prompt-delayed matrix which corresponded to pairs of  $\gamma$  rays in which the first one came as a prompt, in-flight decay, while the delayed transition was measured between 45 and 780 ns later (see Table 3.2).

#### 4.2.1 Transitions below the $10^+$ isomer in $^{136}\text{Ba}$

The observation of the 819 keV ( $2^+ \rightarrow 0^+$ ) transition in  $^{136}\text{Ba}$  in the delayed spectrum shown in Fig. 4.8 demonstrates the presence of an isomer in this nucleus. Figure 4.8 shows all the transitions up to the previously reported  $8^+$  state, together with a transition at 363 keV, which is interpreted to be the direct decay from a  $10^+$  isomer. The excitation energy of this isomer is established from the  $\gamma - \gamma$  coincidence relationships to be 3357 keV.

Spins and parities have been established for the levels in  $^{136}\text{Ba}$  up to the  $I^\pi = 8^+$  state at 2994 keV [68, 97]. The  $I^\pi = 8^+$  [97] state at 2994 keV which decays to the  $I^\pi = 6^+$  state via a  $\gamma$  ray of energy 787 keV, is observed in the present work together with a previously unreported branch which decays to the  $I^\pi = 7^-$  isomeric state at 2031 keV [68] via a 964 keV transition.

The multipolarity of the 363 keV transition could be  $E1$ ,  $E2$  or  $M1$ , from the intensity balance across the 2994 keV state.

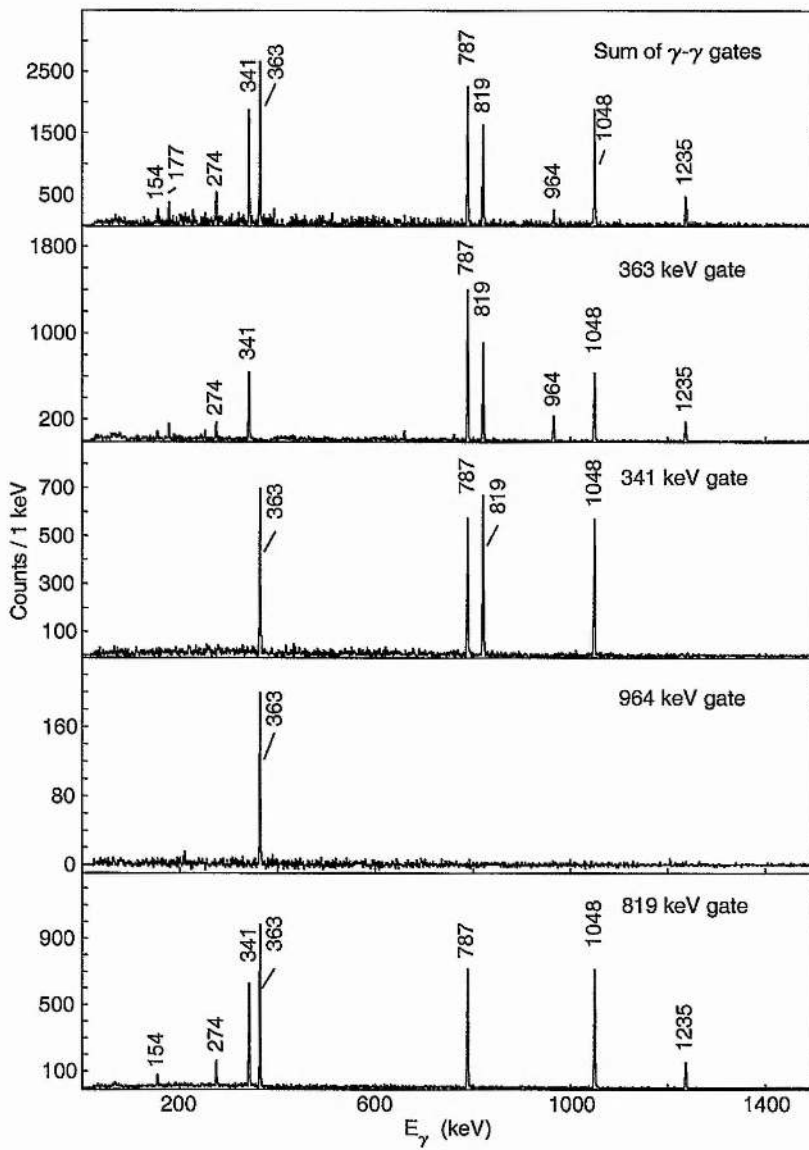


Figure 4.8: Background subtracted delayed  $\gamma$ -ray spectra from the decay of the  $I^\pi = 10^+$  isomer in  $^{136}\text{Ba}$ . The time condition is that the  $\gamma$  rays are observed in the time range  $\Delta t=100\text{-}600$  ns with respect to the master trigger.

Assignments of  $8^\pm$  and  $9^-$  can be ruled out for the 3357 keV level on the basis of non-observation of direct decay branches to the  $7^-$  isomeric state at 2031 keV. Spins of  $11 \hbar$  and higher for the state can be ruled out on the basis of the electron conversion associated with such high-multipole decays (the electron conversion coefficients for the 363 keV transition are  $\alpha(E3) = 0.09$  and  $\alpha(M3) = 0.40$ ) and the measured intensity balance across the 2994 keV state, see Table 4.2. Of the remaining spin/parity assignments  $9^+$ ,  $10^+$  and  $9^-$ , the  $10^+$  is strongly favoured on the basis of both the systematics of the even-Z,  $N = 80$  isotones and the shell-model calculations (see later).

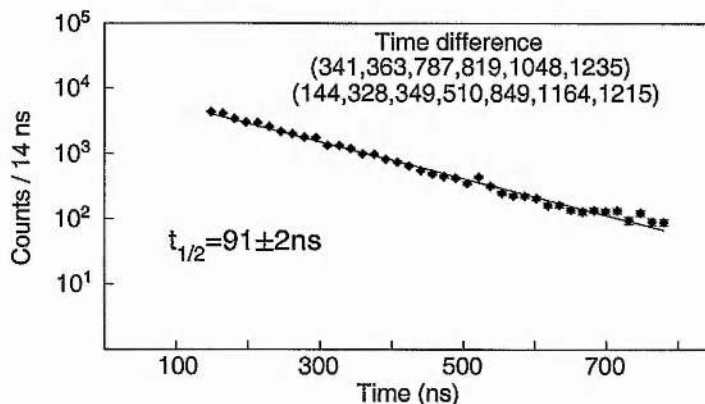


Figure 4.9: Time difference  $\gamma - \gamma$  spectrum obtained by gating above and below the isomeric  $10^+$  state to determine the half-life of the  $10^+$  state in  $^{136}\text{Ba}$  ( $91 \pm 2\text{ ns}$ ).

A half-life of  $t_{1/2}=91\pm 2$  ns, see Fig. 4.9, was obtained for the decay of the  $10^+$  state by measuring the time difference between prompt and delayed transitions feeding in and out of the proposed  $10^+$  state. Assuming an electric quadrupole nature for the 363 keV transition, the  $B(E2 : 10^+ \rightarrow 8^+)$  for  $^{136}\text{Ba}$  is calculated to be  $0.97 \pm 0.02 \text{ } e^2 \text{ fm}^4 = 0.0231 \pm 0.0005 \text{ W.u.}$  Figure 4.10a shows the delayed transition below the isomer, gated on the prompt 144, 328, 349, 510 keV transitions in  $^{136}\text{Ba}$  (see later). The energies and intensities of the delayed transitions observed in  $^{136}\text{Ba}$  are given in Table 4.2.

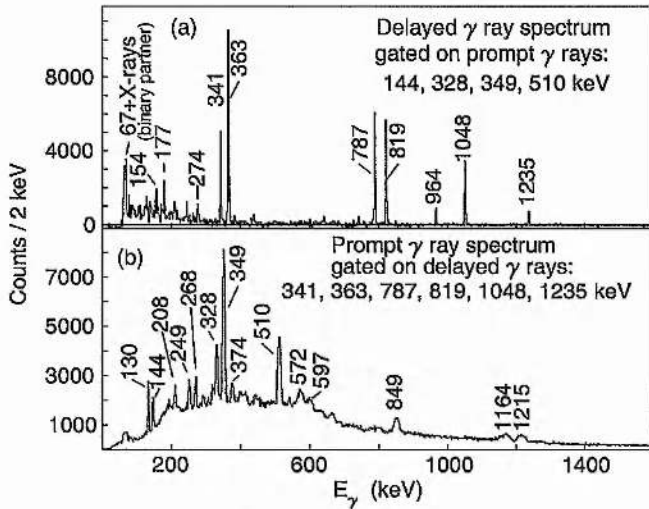


Figure 4.10: Upper spectrum (a) shows the background subtracted delayed  $\gamma$ -ray spectra gated by prompt transitions above the proposed  $10^+$  isomer in  $^{136}\text{Ba}$ . Lower spectrum (b) shows the background subtracted prompt  $\gamma$ -ray spectra gated by delayed transitions placed below the proposed  $10^+$  isomer.

#### 4.2.2 Transitions above the $10^+$ isomer in $^{136}\text{Ba}$

Prompt transitions which form a cascade feeding into the proposed  $I^\pi = 10^+$  isomer were deduced using a  $\gamma - \gamma$  prompt matrix Doppler corrected for BLFs and single-gated by the yrast delayed  $\gamma$  rays observed below the isomer in  $^{136}\text{Ba}$  (see Table 3.2).

Figure 4.10b shows the prompt transitions above the isomer, gated on the delayed 341, 363, 787, 819, 1048 and 1235 keV  $\gamma$  rays in  $^{136}\text{Ba}$ . Figure 4.11 shows a selection of coincidence spectra for  $\gamma$  rays above the isomer. The energies and intensities of the prompt transitions observed above the isomer are given in Table 4.3.

The prompt  $\gamma - \gamma$  coincident spectra for states above the  $10^+$  isomer show evidence for a cascade involving the 349, 510, 849 and 328 keV transitions which are mutually coincident. The ordering of these transitions above the isomer is based on the intensity measurements and the identification of a side-feeding transitions with an energy of 1164 keV which is in prompt coincidence with the 349 and 510 keV transitions and appears to bypass the higher-lying members of the cascade.

**Table 4.2:** Energies, assignments and relative out-of-beam intensities, for transitions observed in  $^{136}_{56}\text{Ba}$ . The uncertainties in the transition energies are  $\pm 0.2$  keV.

$E_\gamma$ (keV)	$E_i$	$E_f$	$I_i^\pi$	$I_f^\pi$	$I_\gamma$ (delayed)
66.9	2207	2141	$6^+$	$5^-$	70(4)
86.8	2141	2054	$5^-$	$4^+$	33(7)
153.6	2207	2054	$6^+$	$4^+$	40(6)
176.9	2207	2031	$6^+$	$7^-$	67(5)
273.9	2141	1867	$5^-$	$4^+$	69(5)
340.8	2207	1867	$6^+$	$4^+$	242(10)
363.0	3357	2994	$10^+$	$8^+$	566(20)
787.1	2994	2207	$8^+$	$6^+$	460(20)
818.6	819	0	$2^+$	$0^+$	551(20)
963.6	2994	2031	$8^+$	$7^-$	112(11)
1048.0	1867	819	$4^+$	$2^+$	410(22)
1235.2	2054	819	$4^+$	$2^+$	126(12)
1312.0					15(3)

The cross-over branch associated with the 144 and 1215 keV  $\gamma$  rays appears to feed directly into the proposed 3706 keV level which is depopulated by the 349 keV transition. The ordering of the 144 keV and 1215 keV transitions is established in the current work on the basis of measured  $\gamma$ -ray intensity.

The ordering of the structure built on top of the  $10^+$  isomeric state as presented in the current work should be taken as tentative. Specifically, the intense transition at 130 keV is in mutual coincidence with the cascade of 349, 510, 849 and 328 keV transitions (see Fig. 4.11), although it does not appear to be in coincidence with the 1164 keV transition which is assumed to feed into the proposed level at 4216 keV. This situation suggests that the 130 keV transition lies above the 849 and 1215 keV transitions, but the large, measured  $\gamma$ -ray intensity for the 130 keV line (see Table

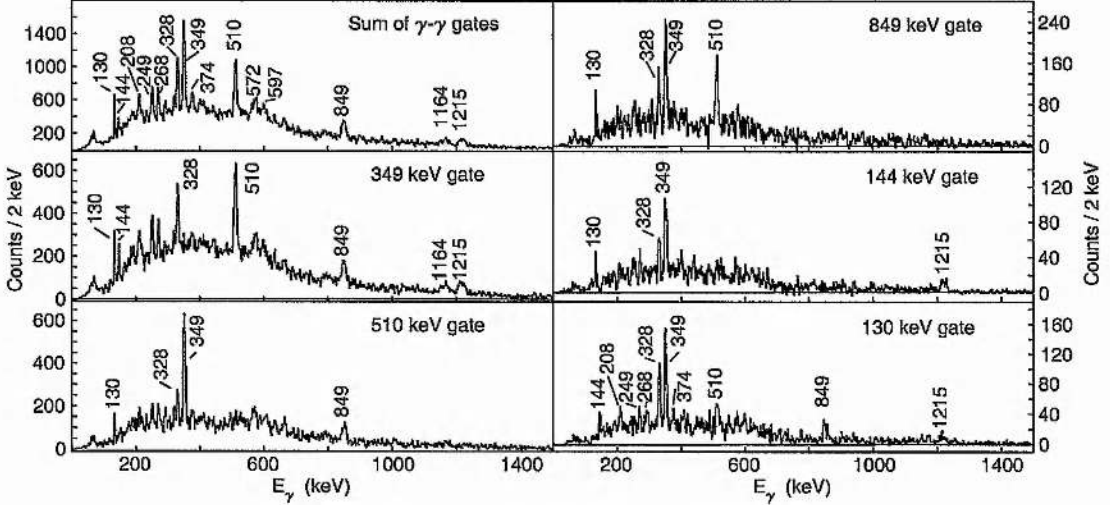


Figure 4.11: Background subtracted prompt  $\gamma$ -ray spectra single-gated by the delayed 341, 363, 787, 819, 1048, 1235 keV transitions placed below the  $10^+$  isomer in  $^{136}\text{Ba}$ . The time condition is that the prompt  $\gamma$  rays are observed within  $\Delta t = \pm 45$  ns of the master trigger.

4.3) presents a potential problem. If it is placed above the proposed 5065 keV level, not all of the decay flux can be accounted for, in the present work, and other non-observed decay branches for the decay flux must be present. It is noted that the 130 keV transition is in coincidence with the unplaced lines at 208, 249, 264 and 374 keV, which may account for some of this ‘missing’ intensity. While the quality of the spectra used for the prompt  $\gamma\gamma$  coincidences above the  $10^+$  isomer can demonstrate a number of mutual coincidences (see Fig. 4.11), they are not of sufficient statistical significance to preclude a different ordering of the lines. One alternative could be that the 130 keV line lies lower in the cascade, *i.e.* either directly feeding into the isomeric state or into the proposed level at 3357 keV. Ultimately the decay scheme above the isomer should be interpreted as a ‘best guess’ on the basis of the available data from the current work.

**Table 4.3:** Energies, relative in-beam intensities and  $A_2$  coefficients for transitions observed in  $^{136}_{56}\text{Ba}$  above the  $10^+$  isomer. The energy resolution for prompt  $\gamma$  rays is approximately 1%.

$E_\gamma$ (keV)	$E_i$	$E_f$	$I_\gamma$ (prompt)	$A_2$
130			598(24)	-0.31(12)
144	(3850)	(3706)	332(15)	-0.08(36)
208			109(8)	
249			110(6)	
268			94(5)	
328	(5393)	(5065)	176(9)	-0.21(9)
349	(3706)	(3357)	566(10)	-0.22(10)
374			94(5)	
510	(4216)	(3706)	372(10)	-0.17(15)
849	(5065)	(4216)	166(8)	-0.06(10)
1164	(5380)	(4216)	126(9)	-0.09(18)
1215	(5065)	(3850)	121(9)	+0.06(34)

### Gamma-ray angular distributions

In order to extract some limited information with regard to the multipolarities [24] of the transitions above the 3357 keV isomer,  $\gamma$ -ray angular distributions for these  $\gamma$  rays have been measured. A  $\gamma_{\text{delayed}} - \gamma_{\text{prompt}} - \theta_{\text{ring}}$  cube (see Table 3.2) was constructed to investigate the angular distributions of prompt  $\gamma$  rays with respect to the beam-target reaction plane. Rings of GAMMASPHERE detectors located at angles of  $\theta$ :  $34.5^\circ$ ,  $59.4^\circ$ ,  $79.9^\circ$ ,  $90.0^\circ$ ,  $103.4^\circ$ ,  $131.4^\circ$  and  $155.5^\circ$  with respect to the beam direction were used to compare prompt  $\gamma$ -ray intensities. The angle-gated intensities for each ring were corrected for their respective  $\gamma$ -ray detection efficiencies as determined from standard  $^{152}\text{Eu}$  and  $^{133}\text{Ba}$  calibration sources placed at the target

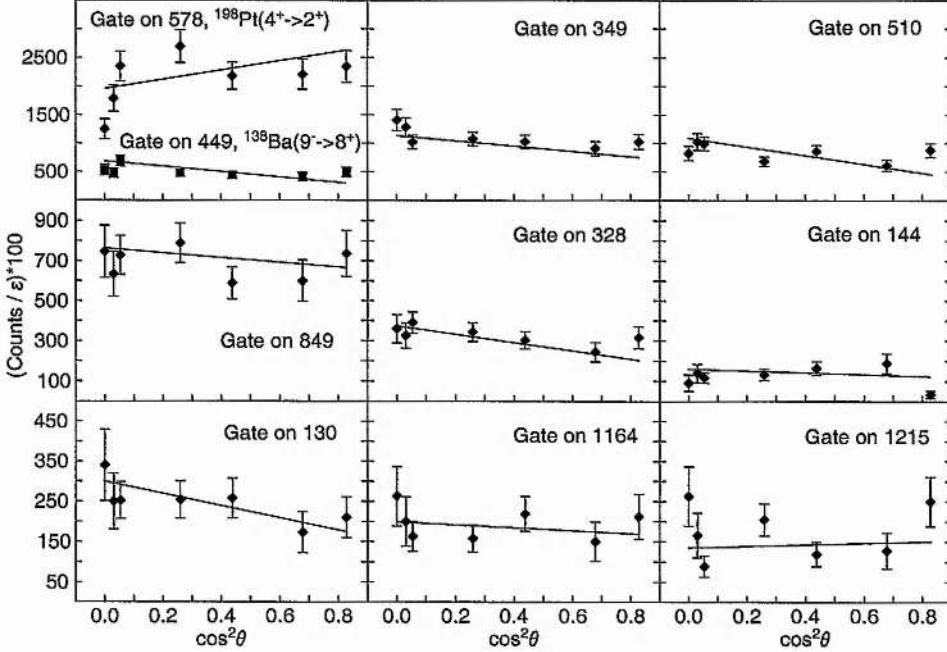


Figure 4.12: Gamma-ray angular distributions. The top-left panel shows angular distributions for known transitions,  $^{198}\text{Pt}$  ( $4^+ \rightarrow 2^+$ ) ( $E2$  transition) and  $^{138}\text{Ba}$  ( $9^- \rightarrow 8^+$ ) ( $E1$  transition), the other panels show the angular distributions for the  $\gamma$  rays above the  $10^+$  isomer in  $^{136}\text{Ba}$ .

position. The  $\gamma$ -ray angular distribution method for deep inelastic collisions has been used previously [72, 98] with thick targets to obtain limited information about the multipolarities of the emitted  $\gamma$  rays. However, as discussed by Zhang *et al.* [72], the alignment of the products from such binary collisions is clearly much reduced compared to highly aligned fusion-evaporation reactions. Naïvely this is what one would expect since the angular momentum of the initial system formed is shared between the two fragments.

To check the level of reliability for the angular distribution analysis in the current work, tests were made with transitions of known multipolarity. The results from two known prompt transitions are shown in Fig. 4.12, for  $^{198}\text{Pt}$  ( $4^+ \rightarrow 2^+$ ) (578 keV,  $E2$  transition) [99] and  $^{138}\text{Ba}$  ( $9^- \rightarrow 8^+$ ) (449 keV,  $E1$  transition) [100]. The angular distribution coefficients  $A_2$  (the  $A_4$  coefficient is neglected in the fit) were deduced to

be  $A_2 = 0.21 \pm 0.18$  and  $A_2 = -0.18 \pm 0.14$  respectively for these transitions. These angular distributions are consistent with previous findings, supporting the current analysis, at least at the  $1\sigma$  level. The fitted curves for the prompt  $\gamma$  rays above the proposed  $10^+$  isomer in  $^{136}\text{Ba}$  are shown in Fig. 4.12. The angular distribution coefficients  $A_2$  (the  $A_4$  coefficient is neglected in the fit) found from fitting the slope of the intensities as a function of  $\cos^2 \theta$  are listed in Table 4.3.

The spin and parity assignments for the states identified above the isomer are somewhat problematic due to the significant uncertainties in the measured angular distributions. These result in making most values consistent with no measurable anisotropy at the  $2\sigma$  level. However, the data suggests that the 349 keV is consistent with a dipole decay at the  $1\sigma$  level.

#### 4.2.3 Discussion of $^{136}\text{Ba}$

The nucleus  $^{136}_{56}\text{Ba}$  has six valence protons outside the closed shell at  $Z = 50$  and 2 neutron holes with respect to the closed shell at  $N = 82$ . It was pointed out in 1973 by Meyer-Lévy and Lopac [101] that many of the low-lying properties of the  $N = 80$  isotones might be explained by the simple coupling of the two-neutron holes to a quadrupole vibrator core. The authors of Ref. [101] also noted that the spectral pattern of the  $N = 80$  isotones from  $^{132}_{52}\text{Te}$  up to  $^{140}_{60}\text{Nd}$  were rather similar with the presence of a two-phonon, quadrupole vibrational triplet established for  $^{136}\text{Ba}$  and its neighbour,  $^{138}\text{Ce}$ . This work ignored any effects from the proton particles and allowed couplings of neutron-hole states from the  $d_{\frac{3}{2}}$ ,  $s_{\frac{1}{2}}$ ,  $h_{\frac{11}{2}}$ ,  $d_{\frac{5}{2}}$  and  $g_{\frac{7}{2}}$  orbitals to a vibrational core. While this approach gave a reasonable prediction for the energies of the low-lying negative-parity states and the first  $2^+$  and  $4^+$  levels, it predicted that the yrast  $6^+$  and  $8^+$  states lay above the yrast  $10^+$  level. This clearly pointed to the need to include *both* proton and neutron degrees of freedom in the calculations for such apparently simple, two-neutron hole systems.

### Shell Model and Pair-Truncated Shell Model Calculations for $^{136}\text{Ba}$

In order to understand the structure of  $^{136}\text{Ba}$ , a shell model approach such as the one described in Ref. [4] has been carried out in the present work. To truncate the model space, the proton single-particle orbitals involved in the calculations are restricted to the three orbitals,  $0g_{\frac{7}{2}}$ ,  $1d_{\frac{5}{2}}$  and  $0h_{\frac{11}{2}}$ , which have initial single-particle energies of 0.0, 0.963 and 2.760 MeV respectively. The neutron single-particle orbitals include all of the five orbitals between the  $N = 50$  and 82 shell, *i.e.* the  $1d_{\frac{3}{2}}$ ,  $0h_{\frac{11}{2}}$ ,  $2s_{\frac{1}{2}}$ ,  $1d_{\frac{5}{2}}$  and  $0g_{\frac{7}{2}}$  which have single-particle energies of 0.0, 0.242, 0.332, 1.655 and 2.434 MeV respectively. Those single-particle energies are extracted from experiment.

The effective shell-model hamiltonian is written as,

$$H = H_\nu + H_\pi + H_{\nu\pi}, \quad (4.1)$$

where  $H_\nu$ ,  $H_\pi$ , and  $H_{\nu\pi}$  represent the neutron-neutron interaction, the proton-proton interaction and the neutron-proton interaction respectively. The interaction among like nucleons  $H_\tau$  ( $\tau = \nu$  or  $\pi$ ) consists of spherical single-particle energies, a monopole-pairing interaction ( $MP$ ), a quadrupole-pairing interaction ( $QP$ ), a quadrupole-quadrupole interaction ( $QQ$ ), a hexadecapole-pairing ( $HP$ ) and a hexadecapole-hexadecapole ( $HH$ ) interaction. The strengths of these interactions are determined so as to reproduce the corresponding experimental energies of the singly-closed-shell nuclei,  $^{138}_{56}\text{Ba}_{82}$  and  $^{130}_{50}\text{Sn}_{80}$ . A quadrupole-quadrupole interaction is the only term in  $H_{\nu\pi}$ , the strength of which is adjusted to reproduce the excitation energy of the  $10^+$  isomer. A detailed description of these interactions can be found in Ref. [4]. The determined strengths of the interactions, in MeV, are  $G_{0\nu} = 0.145$ ,  $G_{2\nu} = 0.016$ ,  $\kappa_\nu = 0.035$ ,  $G_{4\nu} = 0.700$ ,  $\kappa_{4\nu} = 1.600$ ,  $G_{0\pi} = 0.180$ ,  $G_{2\pi} = 0.010$ ,  $\kappa_\pi = 0.055$ ,  $G_{4\pi} = 0.600$ ,  $\kappa_{4\pi} = 0.300$  and  $\kappa_{\nu\pi} = -0.165$ . The definitions of the  $HP$  and  $HH$  interactions are extensions of the  $QP$  and the  $QQ$  interactions from angular momentum coupling two to four, but no radial dependence is assumed. These hexadecapole interactions are necessary for a better fit, since the number of valence protons and neutrons is small in  $^{136}\text{Ba}$  and quadrupole collectivity is still

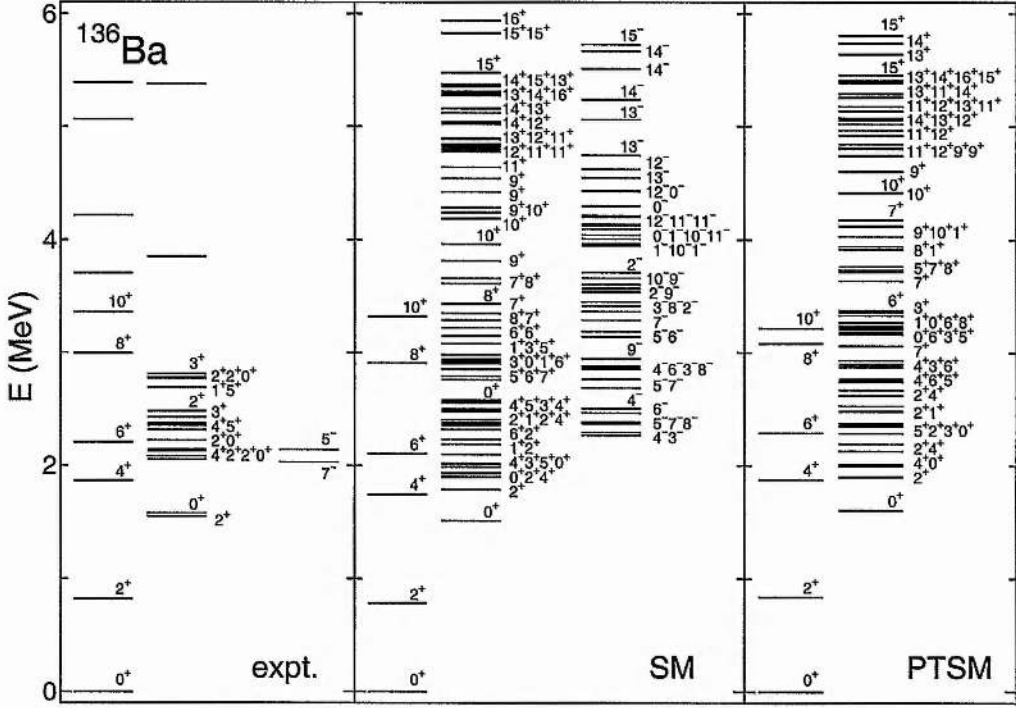


Figure 4.13: Comparison of the experimental energy spectra (left panel) with the results of the shell-model calculation (middle panel) and the pair-truncated shell-model calculations (right panel) for  $^{136}\text{Ba}$  (see text for details). Note that in the middle and right panel the states are separated into columns for the yrast states up to  $10^+$ , the positive-parity states and the negative-parity states.

not dominant compared to other interactions. In the central panel of Fig. 4.13 the results of the shell-model calculations are shown compared with the experimental decay scheme for  $^{136}\text{Ba}$  as deduced in the current work. The comparison for the even-spin yrast sequence up to the proposed  $10^+$  isomer is rather impressive, with the calculations reproducing the ordering of the even-spin yrast sequence.

To study the basic structure of the levels in  $^{136}\text{Ba}$  and to keep the basis to a reasonable truncation, the pair-truncated shell model (PTSM) approach, which is described in Ref. [5], has also been used. This approach is very similar to the interacting boson model (IBM) [6] in concept, but the bosons are now replaced by correlated nucleon pairs to treat Pauli effects explicitly. In addition to the  $S: J = 0$

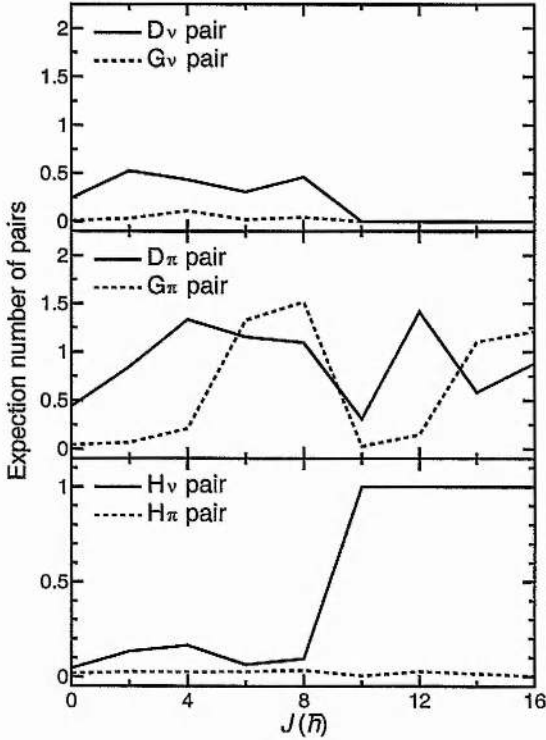


Figure 4.14: The upper panel shows the expectation numbers of neutron  $D_\nu$  and  $G_\nu$  pairs, the middle panel shows the expectation numbers of proton  $D_\pi$  and  $G_\pi$  pairs calculated in the PTSM. The lower panel shows the expectation numbers of neutron and proton  $H_{\nu,\pi}$  pairs calculated in the PTSM. The expectation numbers are for the positive yrast states.

pairs, the truncated valence space only allows pair excitations of the following type,  $D$ :  $J = 2$ ,  $G$ :  $J = 4$  and  $H$ . Note that the calculation is limited to a single  $H$  pair that can only be formed by the coupling of two  $h_{\frac{11}{2}}$  proton particles or neutron holes to angular momentum  $J = 0, 2, 4, 6, 8, 10$ . In contrast, the other pairs in this model space are collective and can be made from linear combinations of other angular momentum couplings between pairs of nucleons in different single-particle orbitals. All these pairs have positive parity so that only positive parity states are predicted. In the right panel of Fig. 4.13 the results of the PTSM are shown in comparison with the shell-model and experimental results.

**Table 4.4:** The expectation numbers of  $D$ ,  $G$  and  $H$  pairs calculated in the PTSM for the yrast  $8_1^+$  state and the second  $8_2^+$  state.

$J^\pi$	$D_\nu$	$G_\nu$	$H_\nu$	$D_\pi$	$G_\pi$	$H_\pi$
$8_1^+$	0.4577	0.0431	0.0938	1.0948	1.5163	0.0331
$8_2^+$	0.0012	0.0068	0.9911	0.2213	0.0272	0.0043

Figure 4.14 shows the expectation number of pairs for the yrast positive-parity sequence in  $^{136}\text{Ba}$  from the PTSM calculations. From the upper two panels in Fig. 4.14, one can see that the predicted wavefunctions of the positive-parity yrast states up to spin  $8^+$  are mostly dominated by proton  $D$  and  $G$  pair couplings. On the contrary, as shown in the lowest panel of Fig. 4.14, the yrast  $10^+$  state is dominated by a neutron  $H$  pair, corresponding to the maximally coupled  $(\nu h_{\frac{11}{2}})^{-2}$  configuration. The dramatic alteration in the number and character of pairs between the  $10^+$  isomeric state and the  $8^+$  state is responsible for the isomeric nature of the  $10^+$  state and also for the large reduction in the  $B(E2)$  transition rate (see below). The shell-model calculations (see Fig. 4.13) predict that a second  $8_2^+$  state lies just below the yrast  $10^+$  isomer. This is predominantly the non-maximally coupled  $(\nu h_{\frac{11}{2}})^{-2}_{8^+}$  configuration. As shown in Table 4.4 the wavefunction of the second  $8_2^+$  state is dominated by a  $H_\nu$  pair, meanwhile the yrast  $8_1^+$  state is dominated by  $D_\pi$  and  $G_\pi$  pairs.

Using the resulting shell-model wavefunctions,  $B(E2)$  values are predicted using effective charges with the conventional relation,  $e_\nu = -\delta e$  and  $e_\pi = 1 + \delta e$  as in [102]. Note that the effective charge for the neutron is negative since neutrons are treated as holes in this scheme. The  $\delta$  value is determined to give the experimental  $B(E2 : 2_1^+ \rightarrow 0_1^+)$  value. The adopted effective charges are  $e_\nu = -0.82e$  and  $e_\pi = +1.82e$ . The calculations predict a value for the decay from this isomer of  $B(E2 : 10_1^+ \rightarrow 8_1^+) = 0.04 \text{ e}^2\text{fm}^4$ , somewhat smaller than the experimentally deduced result of  $0.97(2) \text{ e}^2\text{fm}^4$ . Table 4.5 lists the calculated and experimental  $B(E2)$  values for the yrast

Table 4.5: Comparison of the yrast  $B(E2)$  values in the shell model (SM) with the measured values in  $e^2\text{fm}^4$ . The experimental values have been taken from [103, 104] and the present work.

$J_i^\pi \rightarrow J_f^\pi$	SM	expt.
$2_1^+ \rightarrow 0_1^+$	802	801(6)
$4_1^+ \rightarrow 2_1^+$	1093	
$6_1^+ \rightarrow 4_1^+$	251	38.6(9)
$8_1^+ \rightarrow 6_1^+$	932	
$10_1^+ \rightarrow 8_1^+$	0.04	0.97(2)

sequence in  $^{136}\text{Ba}$ . Note that the theoretical staggering of  $B(E2)$  values is caused by the alternation of the number of proton  $D$  pairs and  $G$  pairs and the neutron  $H$  pair.

The shell-model calculations also predict the observed low-lying negative-parity states with spin/parity  $5^-$  and  $7^-$  and intriguingly also predict an  $8^-$  state at a similar energy. There is no obvious evidence for this predicted  $8^-$  negative-parity yrast trap in the current data. Such a state might however be very long lived, particularly if it lies below the well known  $t_{1/2}=0.3$  s,  $I^\pi = 7^-$  isomer [66]. However, as shown in Fig. 4.10, there is a weakly populated peak at 1312 keV which is not identified with decays from known states in the present work. This may be a candidate for an  $M2$  decay from the  $10^+$  isomer directly to the predicted (long-lived) yrast  $I^\pi = 8^-$  state. There is no evidence in the current work for the population of the second  $2^+$  state at 1551 keV corresponding to the  $n = 2$  phonon vibration [66].

With regard to the comparison between the calculations and the data for the states above the  $10^+$  isomer, it is noteworthy that the yrast states which are predicted to lie above the isomer all have negative parity and thus must be comprised partly from a  $\nu h_{\frac{11}{2}}$  component in their wavefunction. Indeed the calculations do not predict a positive-parity state of spin 11 or higher until approximately 1.5 MeV

above the isomeric  $10^+$  state. However, the calculations predict a  $10^-$  state which lies a few hundred keV above the  $10^+$  isomer and both  $11^-$  and  $12^-$  states a few hundred keV above that.

### Comparison with $N = 80$ isotones

All the even-Z,  $N = 80$  isotones (see Fig. 4.15) from  $^{130}_{50}\text{Sn}$  to  $^{148}_{68}\text{Er}$  exhibit  $10^+$  isomeric states [83, 84, 85, 86, 87, 88]. In  $^{130}_{50}\text{Sn}$  [83],  $^{132}_{52}\text{Te}$  [84],  $^{134}_{54}\text{Xe}$  [84],  $^{138}_{58}\text{Ce}$  [85] and  $^{140}_{60}\text{Nd}$  [86] this  $10^+$  isomer has been associated with a  $(\nu h_{\frac{11}{2}})^{-2}_{10^+}$  configuration. In  $^{138}\text{Ce}$  and  $^{140}\text{Nd}$  [86] the magnetic dipole moment measurements yielding values of  $g = -0.176(10)$  and  $g = -0.192(12)$  respectively suggest that the configurations for these two  $10^+$  isomers are consistent with the  $(\nu h_{\frac{11}{2}})^{-2}_{10^+}$  configuration being the major component. In  $^{142}_{62}\text{Sm}$  and  $^{144}_{64}\text{Gd}$  [87], two  $10^+$  states have been observed with the lower-lying one being isomeric. This has been interpreted [87] as competing  $(\nu h_{\frac{11}{2}})^{-2}$  and  $(\pi h_{\frac{11}{2}})^2$  configurations. In  $^{142}_{62}\text{Sm}$ , the (lower-lying) isomeric  $10^+$  state is mainly two neutron holes in the  $h_{\frac{11}{2}}$  shell, meanwhile for  $^{144}_{64}\text{Gd}$  the isomeric  $10^+$  state is proposed to be mainly a two proton configuration. For the heavier isotones,  $^{146}_{66}\text{Dy}$  [88, 105] and  $^{148}_{68}\text{Er}$  [88, 106], the  $10^+$  isomeric states are both thought to have predominantly  $(\pi h_{\frac{11}{2}})^2_{10^+}$  configurations, since according to the systematics the  $(\nu h_{\frac{11}{2}})^{-2}$  states (see Fig. 4.15) are expected around 3.7 MeV and have not been reported in these nuclei to date [88].

Figure 4.16c shows the systematics of the  $B(E2 : 10^+ \rightarrow 8^+)$  for the even-Z,  $N = 80$  isotones from  $^{130}\text{Sn}$  to  $^{142}\text{Sm}$ . There is an obvious retardation in the decay from the isomeric  $10^+$  state for  $^{136}\text{Ba}$ ,  $^{138}\text{Ce}$  [85] and  $^{142}\text{Sm}$  [87] compared to the lighter isotones. Lach *et al.* [87] suggest that such large hindrances require a high configuration forbiddenness and suggested a seniority four configuration for the yrast  $8^+$  state in  $^{142}\text{Sm}$ .

The sudden decrease in the  $B(E2 : 10^+ \rightarrow 8^+)$  value at  $^{136}\text{Ba}$  as compared to the lighter  $N = 80$  isotones can be understood qualitatively in terms of the likely components of the wavefunctions of the yrast  $10^+$  and  $8^+$  states. As discussed above

## Chapter 4. Results and Discussion

---

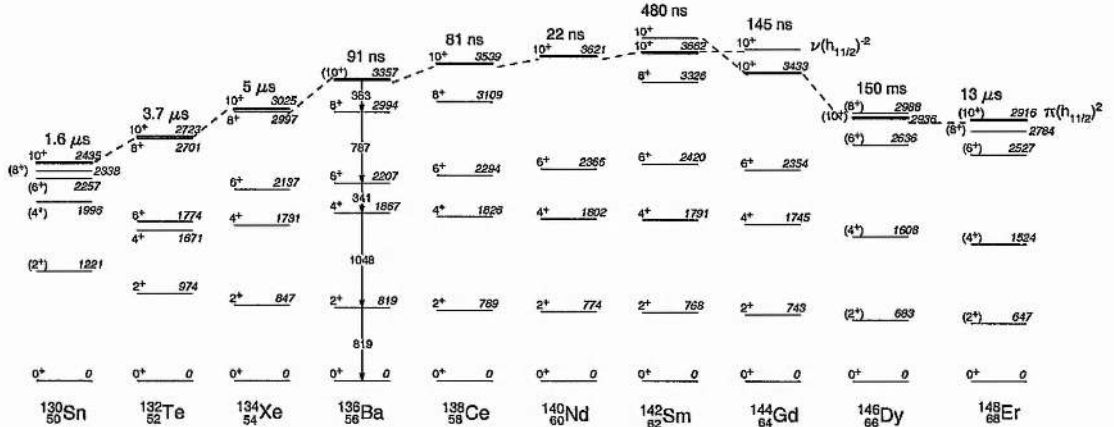


Figure 4.15: Energy systematics for the  $N = 80$  isotones. The predominantly  $(\nu h_{11/2})^{-2}$  or  $(\pi h_{11/2})^2$  configuration character of the  $10^+$  state is indicated for each isotope.

from  $g$ -factor measurements and energy systematics, the nature of the yrast isomeric  $10^+$  state is predominantly  $(\nu h_{11/2})^{-2}$  in character in all the even- $Z$ ,  $N = 80$  isotones between  $^{130}\text{Sn}$  and  $^{142}\text{Sm}$ . For  $^{130}\text{Sn}$ , the closed shell nature of the  $Z = 50$  core gives rise to a ‘textbook’ two-hole single- $j$  shell multiplet, implying that the yrast  $8^+$  state is predominantly of  $(\nu h_{11/2})^{-2}$  character. By a similar argument, the two-proton system,  $^{132}\text{Te}$  can have only seniority two couplings in the  $Z > 50$  valence space used. Neglecting excitations into the proton  $h_{11/2}$  orbitals (which is reasonable since these orbitals are at the top of the shell) the two valence protons alone could only generate a maximum angular momentum of  $6^+$  from  $(\pi g_{7/2})^2$ . Hence states of spin  $8^+$  or more, must have seniority four, or incorporate the neutron pair with  $J > 0$ , since breaking the  $Z = 50$  core would be energetically less favourable. For  $Z > 54$  however, angular momenta of 8 and above can also be generated in the proton space. The development of an increasing proton component in the yrast  $8^+$  state would then explain the observed decrease in the  $B(E2)$  from the predominantly 2-neutron  $10^+$  state.

The smoothly increasing excitation energy of the  $10^+$  isomeric state (and by inference the  $(\nu h_{11/2})^{-2}$  configuration) appears as a standard feature of the  $N = 80$

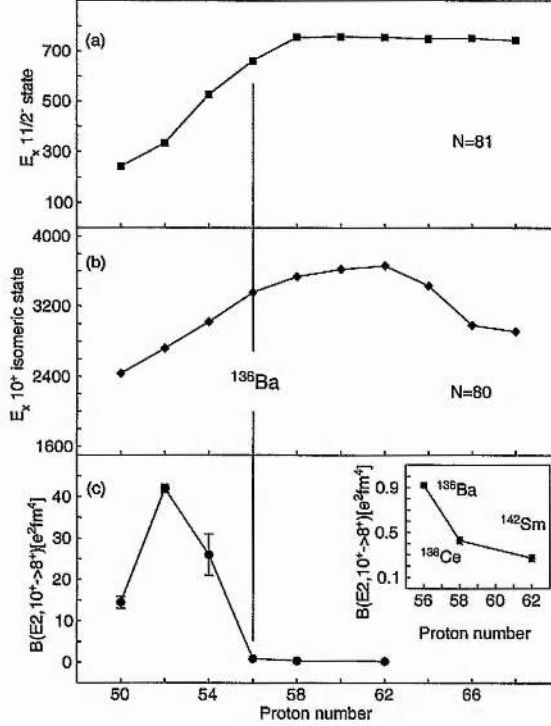


Figure 4.16: Upper panel (a) shows the energies of the  $I^\pi = \frac{11}{2}^-$  single-particle states for the  $N = 81$  isotones, taken from [66]. Panels (b) and (c) show the excitation energy of the  $I^\pi = 10^+$  isomer and the  $B(E2 : 10^+ \rightarrow 8^+)$  transitions rates for the  $N = 80$  isotones respectively, taken from [84, 85, 87].

isotones from tin to samarium. This can be understood from Fig. 4.16a, which shows the excitation energy of the lowest-lying  $I^\pi = \frac{11}{2}^-$  single-hole state in the odd- $A$ ,  $N = 81$  isotones. The single-particle excitation energy of the  $h_{\frac{11}{2}}$  neutron orbital is observed to increase with proton number. This increase in single-particle energy is responsible for an increase of more than 1 MeV in the excitation energy of the yrast  $10^+$  state between  $^{130}_{50}\text{Sn}$  and  $^{140}_{60}\text{Nd}$  (see Fig. 4.16b). This increased excitation energy means that the seniority four configurations which include the proton configurations can begin to compete energetically with the seniority two  $(\nu h_{\frac{11}{2}})^{-2}_{8+}$  configuration in the  $N = 80$  isotones at the barium isotope and for heavier elements. This results in a reduction of the  $(\nu h_{\frac{11}{2}})^{-2}$  component in the wavefunction of the yrast  $8^+$  states, which in turn gives rise to the dramatic reduction in the  $B(E2 : 10^+ \rightarrow 8^+)$  value

at  $^{136}\text{Ba}$ .

### Discussion of $^{136}\text{Ba}$ in the Seniority Scheme

To understand the nuclear structure of the  $10^+$  barium isomers, the transition probabilities can be discussed in terms of the seniority scheme (see *Chapter 1*). The seniority quantum number is, in principle, only a good quantum number for spherical or near-spherical nuclei, nevertheless it may persist even when both valence protons and neutrons are present. However, in such cases, it is likely to give way to collective correlations rather quickly with increasing numbers of valence protons and neutrons [8]. This section discusses the  $B(E2, 10^+ \rightarrow 8^+)$  values for the barium ( $Z = 56$ ) isotopes in terms of the seniority scheme. However, before discussing the barium isotopes, the semi-magic tin isotopes, which have a closed shell at  $Z = 50$  are discussed by investigating the energy systematics and the  $B(E2)$  values with the filling of the high-j  $h_{\frac{11}{2}}$  neutron shell.

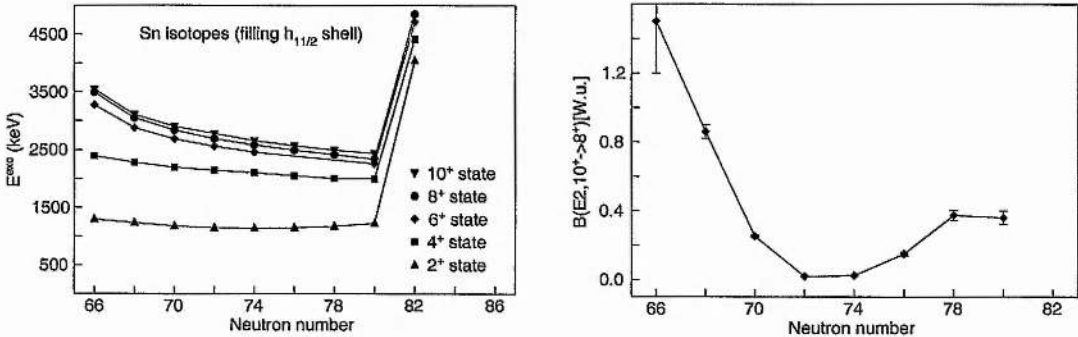


**Figure 4.17:** The left panel shows the energy systematics for the yrast  $2^+, 4^+, 6^+, 8^+, 10^+$  states in the tin isotopes, from  $^{116}\text{Sn}$  to  $^{130}\text{Sn}$ . The right panel shows the  $B(E2)$  value systematics with the filling of the  $h_{\frac{11}{2}}$  orbital for the  $10^+ \rightarrow 8^+$  transition.

Figure 4.17 (left) shows the energy systematics for the  $2^+, 4^+, 6^+, 8^+, 10^+$  for the isotopes  $^{116}\text{Sn}$  [107],  $^{118}\text{Sn}$  [107],  $^{120}\text{Sn}$  [107],  $^{122}\text{Sn}$  [32],  $^{124}\text{Sn}$  [32],  $^{126}\text{Sn}$  [108],  $^{128}\text{Sn}$  [83],  $^{130}\text{Sn}$  [83] and  $^{132}\text{Sn}$  [66]. This plot shows that the energies are quite regular

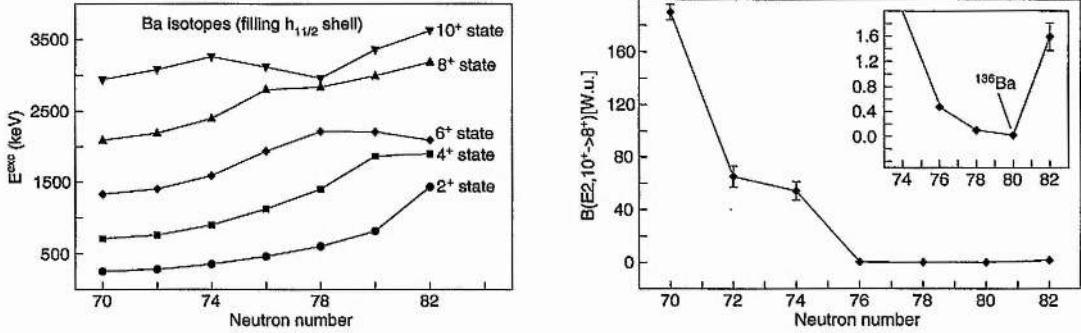


Figure 4.18: The left panel shows the energy systematics for the yrast  $2^+$ ,  $4^+$ ,  $6^+$ ,  $8^+$ ,  $10^+$  states in the barium isotopes, from  $^{126}\text{Ba}$  to  $^{138}\text{Ba}$ . The right panel shows the  $B(E2)$  value systematics with the filling of the  $h_{11/2}$  orbital for the  $10^+ \rightarrow 8^+$  transition.

with a steep increase in the energies of the levels for the magic number  $N = 82$ . Figure 4.17 (right) shows the  $B(E2)$  systematics as the  $h_{11/2}$  orbital is filled, for the  $10^+ \rightarrow 8^+$  transition. Broda *et al.* [32] studied the dependence of the  $E2$  transition rates in terms of a sub-shell occupation number for tin isotopes <sup>a</sup>. It is found that the half filling of the  $h_{11/2}$  shell happens at  $N = 73$ , *i.e.* for  $^{123}\text{Sn}$ .

Figure 4.18 (left) shows the energy systematics for the  $2^+$ ,  $4^+$ ,  $6^+$ ,  $8^+$ ,  $10^+$  for the isotopes  $^{126}\text{Ba}$  [109],  $^{128}\text{Ba}$  [110],  $^{130}\text{Ba}$  [111],  $^{132}\text{Ba}$  [112],  $^{134}\text{Ba}$  [113],  $^{136}\text{Ba}$ ,  $^{138}\text{Ba}$  [100]. In this case, unlike the tin isotopes the energy systematics for the  $10^+$  state are not as regular, and vary both up and down with increasing neutron number. This suggests that the configuration of the  $10^+$  state for barium isotopes changes as the neutron number increases. Figure 4.18 (right) shows the  $B(E2)$  value systematics with the filling of the  $h_{11/2}$  orbital for the  $10^+ \rightarrow 8^+$  transition. The inset shows the  $B(E2)$  values around  $^{136}\text{Ba}$ , where the  $B(E2 : 10^+ \rightarrow 8^+)$  minimum value is observed around ( $N = 80$ ).

<sup>a</sup>Note that the errors given in this paper for the  $B(E2)$  transition rates in the Sn isotopes  $^{128}\text{Sn}$  and  $^{130}\text{Sn}$  are misleading, since the  $B(E2)$  value with its errors should be 14.4 (1.3) and 14.5 (1.4)  $e^2 \text{fm}^4$  respectively.

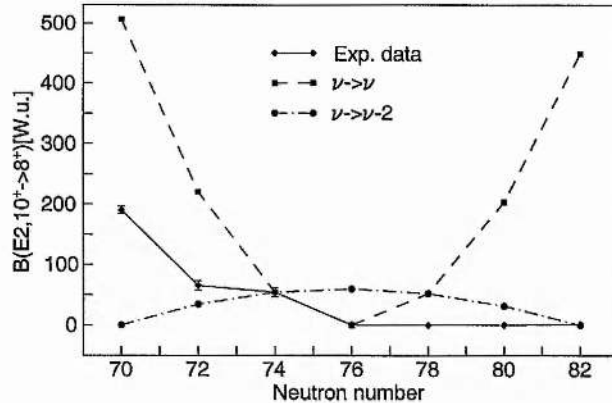


Figure 4.19: Comparison of the experimental  $B(E2)$  values (solid line) for barium isotopes filling the  $h_{\frac{11}{2}}$  shell with the theoretical  $B(E2)$  values obtained in the seniority scheme framework, for transitions that connect states with  $\Delta\nu = \pm 2$  (dashed-dotted line) and for transitions that do not change seniority (dashed line).

A calculation of the  $B(E2)$  values in the seniority scheme framework has been performed using Equations 1.6 and 1.7, for transitions that connect states with  $\Delta\nu = \pm 2$  and for transitions that do not change seniority  $\Delta\nu = 0$  respectively, see Fig. 4.19. The theoretical  $B(E2)$  values have been normalised to the experimental value for  $^{130}\text{Ba}$  ( $N = 74$ ). In order to calculate the  $B(E2)$  transition rates it has been considered that the variable  $n$  (number of neutrons in the  $h_{\frac{11}{2}}$  shell, see Equations 1.6 and 1.7) is assumed to be  $n = 0$  for  $^{126}\text{Ba}$  and continues to increase along the heavier barium isotopes, up to  $n = 12$  for  $^{138}\text{Ba}$ .

From Fig. 4.19 it can be concluded that seniority is not a good quantum number for the barium isotopes,  $Z = 56$ . The experimental values do not agree with the seniority scheme predictions for the  $\Delta\nu = 0$  or  $\Delta\nu = 2$  transitions. The experimental  $B(E2)$  values follow the parabolic trend, given by  $\Delta\nu = 0$ , for light barium isotopes but it flattens for heavier isotopes, instead of increasing as would be expected for a non-seniority changing transition. In the case of  $^{136}\text{Ba}$  the  $B(E2, 10^+ \rightarrow 8^+)$  transition rate is given by the difference in structure of the  $10^+$  isomeric state and the  $8^+$  state. The  $10^+$  state is dominated by two neutron holes in the  $h_{\frac{11}{2}}$  orbital, while the  $8^+$  state is dominated by proton configurations. In addition it should be

remembered that the  $\beta_2$  ground state deformation parameter for barium isotopes are predicted to range from 0.233 for  $^{126}\text{Ba}$  to -0.108 for  $^{134}\text{Ba}$  [114].

## 4.3 A Multi-Quasiparticle Isomeric State in $^{184}_{74}\text{W}$

In the reaction studied in this thesis, high spin states were populated in the neutron-rich  $^{184}_{74}\text{W}$  isotope, which were fed via an isomer. Previous to this study, 2-quasiparticle states up to  $7 \hbar$  including an  $t_{1/2} = 8.3 \mu\text{s}$ ,  $K^\pi = 5^-$  state were observed [115, 116].

### 4.3.1 Decay Scheme of $^{184}\text{W}$

Looking at delayed  $\gamma$ - $\gamma$  coincidences, the level scheme shown in Fig. 4.20 was obtained. The spectrum gated by the 253 keV ( $4^+ \rightarrow 2^+$ ) transition in the ground-state band of  $^{184}\text{W}$  is shown in Fig. 4.21.

The newly observed transitions at 1227 and 554 keV link the newly observed structure at 2480 keV to members of the ground-state and  $\gamma$  bands respectively, for which the spins and parities have been established [66]. The states are fed by an isomer at 3862 keV with a measured half-life of  $t_{1/2} = 188 \pm 38$  ns (see Fig. 4.22). This isomeric level de-populates via a series of  $\gamma$  rays, some of which are regularly spaced in energy, characteristic of a strongly coupled band structure. The regular spacing of the 260, 321 and 381 keV transitions and tentative evidence for cross-over transitions of 581 ( $= 260 + 321$ ) and 702 ( $= 321 + 381$ ) keV has lead to their placement in a band structure, directly above the 2480 keV level. The 260, 321 and 381 keV transitions are assumed to be mixed  $M1/E2$  (in the case of being  $E2$  transitions, the low energy spacing between the levels would lead to an unrealistically large deformation  $\beta_2$ ).

The placement of the 274 keV transition in the level scheme has not been uniquely determined, but is thought to be the second decay below the isomer in the scheme largely because the 148 keV transition is favoured as the direct isomer decay due to its low energy. However, it is noted that an alternative placement directly above

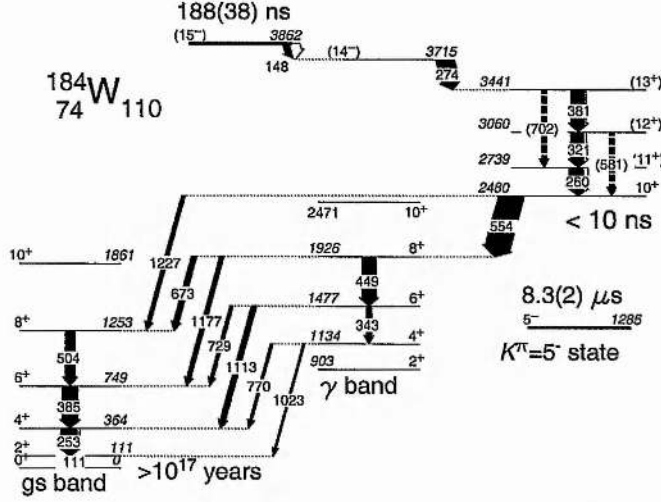


Figure 4.20: Partial level scheme for  $^{184}_{74}\text{W}_{110}$  showing the newly observed 4-quasiparticle isomer at  $E_x = 3862$  keV (this work) together with the previously known 2-quasiparticle isomer at 1285 keV [115, 116]. It is also shown two  $10^+$  levels at 1816 and 2471 keV from which no decay has been observed in the current work [66]. The widths of the arrows are proportional to the relative  $\gamma$ -ray intensity (black) and electron conversion intensity (white) except for the tentative transitions (dashed arrows). Preferred tentative spin and parity assignments are given in parentheses, though there are typically several other possible labels for each of these levels (see text).

the 2480 keV level is possible for the 274 keV transition.

Assuming that the direct decay from the isomer is via the 148 keV  $\gamma$ -ray transition, the possible multipolarities from the Weisskopf single-particle estimates are given in Table 4.6. Under such an assumption, the 148 keV decay is restricted to  $E1$ ,  $M1$  or  $E2$  character for  $F_W > 1$  ( $F_W = \frac{t_{1/2}^\gamma(\text{expt.})}{t_{1/2}^\gamma(\text{Weiss.})}$ ) The large  $F_W$  factor for an  $M1$  transition is also consistent with  $M1$  transition rates for other decays from 4-quasiparticle intrinsic states in this mass region, *e.g.* in  $^{180}\text{W}$  [118]. A similar constraint is achieved by balancing the intensity of the 148 keV transition with the 274 keV strength. The resulting total electron conversion coefficient for the 148 keV transition is  $\alpha_T(\text{expt.}) = 4.3 \pm 2.4$ . The large uncertainty arises from the subtraction

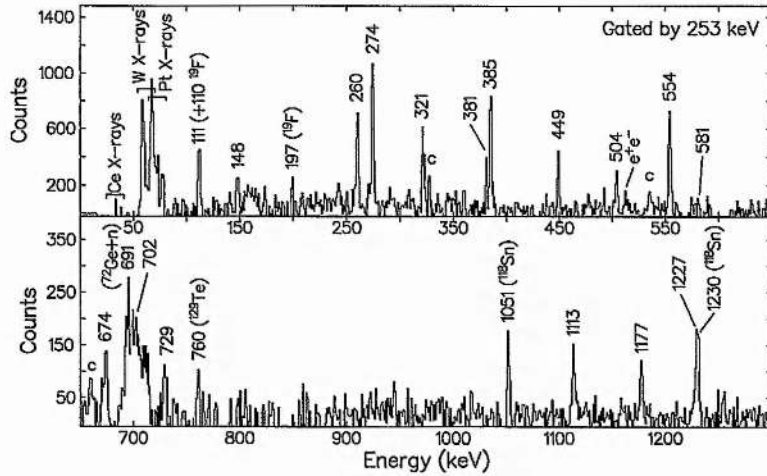


Figure 4.21: Gamma-ray coincidence spectrum gated by the delayed 253 keV transition in the ground-state band of  $^{184}\text{W}$ . The transitions labelled only by energy are assigned to  $^{184}\text{W}$ . Known contaminants in coincidence with the 253 keV are indicated and those which are unknown are labelled by ‘c’. Intense X-rays from the platinum target are due to ‘time-walk’ into the delayed spectra. X-rays from the cerium binary partner nuclei are due to coincident isomeric decays and/or timewalk.

of the background, which is considerable at low energies. However, this is consistent (within 2 standard deviations) only with  $E1$ ,  $M1$  and  $E2$  character (see  $\alpha_T$  in Table 4.6) and (marginally) favours  $M1$ .

As was pointed out previously it is not possible to extract any angular-distribution information about the transition multipolarities since the alignment is lost when the recoils are implanted in CHICO. However, considering the direct feeding of the  $I^\pi = 8^+$  states in both the ground-state and  $\gamma$  bands and the absence of any direct decays to the corresponding  $I^\pi = 6^+$  levels, possible spins and parities for the 2480 keV state are  $I^\pi = 8^-, 9^+, 9^-$  and  $10^+$ . Here,  $E1$ ,  $M1$  and  $E2$  multipolarities have been considered as those which are consistent with the absence of a significant half-life for the initial (2480 keV) state. It is noteworthy that no 619 keV transition to the  $I^\pi = 10^+$  level in the ground-state band (parallel to the 1227 keV decay to the  $I^\pi = 8^+$  member) has been observed. A generous upper limit of  $10\text{ ns}$  has been assigned to the half-life of the 2480 keV state. The absence of a significant half-life

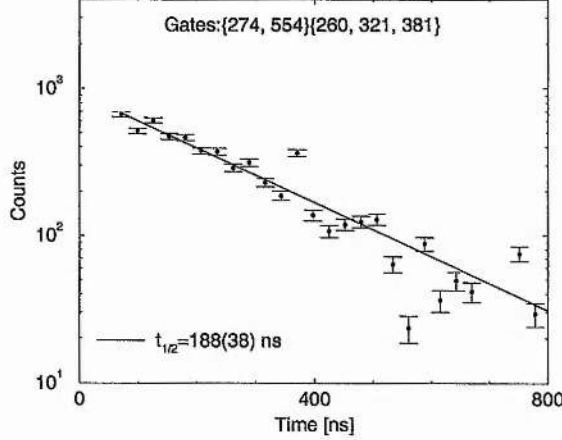


Figure 4.22: Time spectrum showing the  $188 \pm 38$  ns half-life and an exponential fit to the data (solid line) for the 3862 keV isomer in  $^{184}\text{W}$ . It has been obtained from pairs of double  $\gamma$ -ray gates.

in the 2480 keV state is surprising, since the 554 keV transition to the  $\gamma$  band and the 1227 keV transition to the ground state band are highly  $K$  forbidden. Depending on the spin and parity assignment for the 2480 keV state, it can be obtained  $\Delta K = 6, 7, 8, 9, 10$ . In the 180 mass region, there are some examples of half-lives of the order of  $ns$  [119] for similar  $K$ -forbidden transitions. However, the absence of a half-life might be explained by the mixing of states with the same  $I^\pi$ , close in energy. That might be the case if a spin and parity  $I^\pi = 10^+$  is assigned to the 2480 keV state, which lies 9 keV apart from the  $I^\pi = 10^+$  (2471 keV) state in the  $\gamma$  band [120]. The half-life limit of the 2480 keV state was used to determine the mixing matrix element, *i.e.* the strength of the interaction.

The theoretical  $B(E2)$  reduced transition rates within a rotational band can be estimated from [7],

$$B(E2 : I \rightarrow I - 2) = \frac{5}{16\pi} e^2 Q_0^2 |\langle I2K0 | I - 2K \rangle|^2 \quad (4.2)$$

where  $Q_0$  is the intrinsic quadrupole moment and  $\langle I2K0 | I - 2K \rangle$  is a Clebsch Gordan coefficient.

Using the above Equation a  $B(E2 : 10^+ \rightarrow 8^+) = 13158 e^2 fm^2$  is obtained

Table 4.6: Weisskopf single-particle estimates for a 148 keV transition in  $^{184}\text{W}$ . The relevant electron conversion coefficients [22] ( $\alpha_T$ ) are quoted together with the corresponding partial  $\gamma$ -ray half-life.

Mult.	$\alpha_T$	$t_{1/2}^\gamma(\text{expt.})$	$t_{1/2}^\gamma(\text{Weiss.})$	$F_W = \frac{t_{1/2}^\gamma(\text{expt.})}{t_{1/2}^\gamma(\text{Weiss.})}$
[ $M\lambda$ ]		[ns]		
E1	0.137	215(45)	0.66 <sup>a</sup>	325(70)
M1	1.62	490(100)	$6.9 \times 10^{-3}$	$7.1(14) \times 10^4$
E2	0.893	360(70)	126	2.9(5)
M2	10.4	2140(430)	$1.4 \times 10^4$	0.15(4)
E3	10.7	2200(450)	$3.8 \times 10^8$	$5.8(12) \times 10^{-6}$

<sup>a</sup> Including an extra factor of  $10^4$  hindrance, typical for E1 transitions [117].

for the 546 keV transition in the  $\gamma$  band, *i.e.* the half-life of the 2471 keV level is obtained to be  $t_{1/2} = 0.9$  ps. The mixing amplitude  $\beta$  as defined in Equation 1.17 can be calculated from the  $B(E2)$  reduced transition probabilities, if a small mixing is considered (*i.e.* the mixing amplitude  $\alpha^2 \approx 1$ ), as  $\beta = \sqrt{\frac{B(E2)_K}{B(E2)_\gamma}} = \sqrt{\frac{t_{1/2}^\gamma E_\gamma^6}{t_{1/2}^K E_K^6}} > 0.000945$ , where  $B(E2)_K$  and  $B(E2)_\gamma$  are the transition rates of the 2480 and 2471 keV states respectively. The lower limit given for the  $\beta$  value is a consequence of the upper limit for the half-life of the 2480 keV state. Using Equation 1.17 the interaction strength,  $V$ , that causes the mixing can be calculated. The lower limit obtained for the interaction strength is  $V > 0.08$  keV, the upper limit is given by the half of the energy spacing of the measured levels, 4.5 keV. Therefore with a small mixing strength it is possible to account for the absence of half-life in the 2480 keV state.

Considering the previous discussion on the absence of a half-life in the 2480 keV state and recalling that deep-inelastic reactions are known to populate preferentially yrast and near-yrast states [121, 122], therefore, the favoured assignment for the 2480 keV state is  $10^+$ .

When examining coincidences across the new isomeric state in  $^{184}\text{W}$ , no promi-

inent peaks were identifiable. Also, from the prompt data, while transitions in  $^{184}\text{W}$  are clearly visible it was not possible to extract further spectroscopic data, mainly due to the large number of nuclei produced in this reaction and the weak nature of the  $^{184}\text{W}$  channel. The requirement of delayed coincidences dramatically enhances the sensitivity to weak decays.

From the available experimental evidence it is clear that the spin and parity assignments (and ordering) of the observed states above 2.4 MeV are tentative. However, assuming that the 260, 321 and 381 keV transitions can be assigned as ( $\Delta I = 1$ ) in-band transitions, leads to a spin assignment for the 3441 keV level of  $I = 13$ . A higher-lying (274 keV)  $E1$ ,  $M1$  or  $E2$  multipole, in the absence of an intermediate half-life ( $\geq 2$  ns) results in an  $I = 14$  or 15 state at 3715 keV, and an isomeric state at 3862 keV with  $I = 15$ , 16 or 17. While covering a relatively large spin range these possibilities are discussed below.

### 4.3.2 Discussion of $^{184}\text{W}$

The energy systematics of 2- and 4-quasiparticle states in nearby even-even nuclei are shown in Table 4.7. The energies of both the  $K^\pi = 8^-, 9^-$  and  $10_{2\nu}^+$  states in the tungsten and osmium isotopes shown in Table 4.7 have excitation energies close to that of the 2480 keV level observed in  $^{184}\text{W}$ . (The subscript  $2\nu$  indicates the 2-quasineutron  $\{\frac{11}{2}^+[615], \frac{9}{2}^+[624]\}$  configuration (two ( $i_{13/2}$ ) orbitals). However, it is the  $K^\pi = 10_{2\nu}^+$  configuration that matches most closely, especially when taking into account the increase in the energy of the  $K^\pi = 10^+$  arrangement with increasing neutron number ( $N$ ). For  $\Delta N = +2$ ,  $\Delta E_{10_{2\nu}^+} \approx 200$  keV for  $^{184}\text{Os} \rightarrow ^{186}\text{Os}$ . For the same neutron numbers in the tungsten isotopes one might naively expect an energy of  $E_{10_{2\nu}^+} \approx 2430$  keV in  $^{184}\text{W}$ . Note that the energy of the first  $\Delta I = 1$  transition in the  $K^\pi = 10^+$  band in  $^{182}\text{W}$  is 262 keV [123], very close to the 260 keV transition observed in the present work. However, there are some concerns regarding alignment with increasing spin which could be due to mixing with the ground state or the  $\gamma$  band.

## Chapter 4. Results and Discussion

---

**Table 4.7:** Energy systematics in the  $A \approx 184$  region for 2- and 4-quasiparticle states. Energies in brackets indicate tentative assignments. Where multiple states of the same spin and parity are known the energy of the lowest lying state is quoted.

Nucl.	Excitation energy									
	[keV]									
	8 <sup>-</sup>	9 <sup>-</sup>	10 <sup>+</sup> <sub>2ν</sub>	12 <sup>+</sup>	14 <sup>-</sup>	15 <sup>+</sup>	15 <sup>-</sup>	16 <sup>+</sup>	17 <sup>-</sup>	
<sup>180</sup> <sub>74</sub> W <sub>106</sub> <sup>a</sup>	1529				3263	3388	3744	3546		
<sup>182</sup> <sub>74</sub> W <sub>108</sub> <sup>b</sup>	2120			2230 (3415)		3754		3893	4040	
<sup>184</sup> <sub>74</sub> W <sub>110</sub> <sup>c</sup>			(2480)				3862)			
<sup>186</sup> <sub>74</sub> W <sub>112</sub> <sup>d</sup>			(2118)					(3544)		
<sup>184</sup> <sub>76</sub> Os <sub>108</sub> <sup>e</sup>	2046	2301	2367		(3792)					
<sup>186</sup> <sub>76</sub> Os <sub>110</sub> <sup>f</sup>		2166	2564	3187		3732				

References: <sup>a</sup> [118], <sup>b</sup> [123], <sup>c</sup> This work, <sup>d</sup> [133, 124], <sup>e</sup> [119, 125], <sup>f</sup> [134].

Considering the 4-quasiparticle energy systematics in Table 4.7 the  $I = 15$  and  $16$  configurations are closest to the 3862 keV energy of the isomer reported here.

To enable comparisons between the experimental data and the calculated configurations (Table 4.8), the rotational model expressions [127, 128] can be used to extract  $g$  factors for the rotational bands. However, this analysis was unable to discriminate between the different 2-quasiparticle configurations assuming a strongly coupled band structure built on the 2480 keV state, since only upper limits on the intensities of the 581 and 702 keV transitions are available. Both of the  $\Delta I = 2/\Delta I = 1$  branching ratios are  $< 0.38$ . Such an analysis is consistent with the  $K^\pi = 10_{2\nu}^+, 9^-$  and  $8^-$  configurations given in Table 4.8.

**Table 4.8:** Low-lying 2- and 4-quasiparticle states in  $^{184}\text{W}$ . The calculated energy from the blocked BCS calculations is  $E_{qp}$  (see text for details),  $E_{res}$  is the residual nucleon-nucleon interaction energy [132] and  $E_{calc} = E_{qp} + E_{res}$  is directly comparable with the experimentally determined energies. Experimental energies quoted in parentheses are states observed in the current work for which the spins and parities are uncertain. All other values of  $E_{expt}$  are from Ref.[66]. A ‘–’ sign in front of a  $\frac{1}{2}^-$ [510] orbital indicates a configuration with a less than maximal  $K$  coupling.

$K^\pi$	Configuration	Energy (keV)				
		$\pi$	$E_{qp}$	$E_{res}$	$E_{calc}$	$E_{expt}$
$\nu$						
2 <sup>+</sup>	$\frac{3}{2}^-$ [512], $\frac{1}{2}^-$ [510]			1167	-150	1017
3 <sup>+</sup>	$\frac{7}{2}^-$ [503], $-\frac{1}{2}^-$ [510]			1567	-150	1417
4 <sup>-</sup>	$\frac{9}{2}^+$ [624], $-\frac{1}{2}^-$ [510]			2107	-150	1957
5 <sup>-</sup>	$\frac{11}{2}^+$ [615], $-\frac{1}{2}^-$ [510]			1458	-150	1308
5 <sup>+</sup>	$\frac{7}{2}^-$ [503], $\frac{3}{2}^-$ [512]			1762	-188	1574
6 <sup>+</sup>		$\frac{7}{2}^+$ [404], $\frac{5}{2}^+$ [402]	1740	-154	1586	—
6 <sup>-</sup>	$\frac{9}{2}^+$ [624], $\frac{3}{2}^-$ [512]			2105	-150	1955
7 <sup>-</sup>	$\frac{11}{2}^+$ [615], $\frac{3}{2}^-$ [512]			1655	-150	1505
7 <sup>-</sup>		$\frac{9}{2}^-$ [514], $\frac{5}{2}^+$ [402]	1560	+200	1760	—
$8_{2\pi}^-$		$\frac{9}{2}^-$ [514], $\frac{7}{2}^+$ [404]	2395	-123	2272	—
8 <sup>-</sup>	$\frac{9}{2}^+$ [624], $\frac{7}{2}^-$ [503]			2320	+184	2504
9 <sub>1</sub> <sup>-</sup>	$\frac{11}{2}^+$ [615], $\frac{7}{2}^-$ [503]			2067	+184	2251
9 <sub>2</sub> <sup>-</sup>	$\frac{11}{2}^+$ [615], $\frac{7}{2}^-$ [514]			2655	-93	2562
10 <sub>2\nu</sub> <sup>+</sup>	$\frac{11}{2}^+$ [615], $\frac{9}{2}^+$ [624]			2244	+200	2444 (2480) (-36)
10 <sup>-</sup>	$\frac{11}{2}^+$ [615], $\frac{9}{2}^-$ [505]			2790	-184	2606
$10_{2\pi}^+$		$\frac{11}{2}^-$ [505], $\frac{9}{2}^-$ [514]	2966	+200	3166	—
11 <sup>+</sup>	$\frac{11}{2}^+$ [615], $\frac{9}{2}^+$ [624] $\frac{3}{2}^-$ [512], $-\frac{1}{2}^-$ [510]			2902	-250	2652
12 <sup>+</sup>	$\frac{11}{2}^+$ [615], $-\frac{1}{2}^-$ [510]	$\frac{9}{2}^-$ [514], $\frac{5}{2}^+$ [402]	3018	-91	2927	—
13 <sup>+</sup>	$\frac{11}{2}^+$ [615], $\frac{1}{2}^-$ [510]	$\frac{9}{2}^-$ [514], $\frac{5}{2}^+$ [402]	3036	-44	2992	—

Chapter 4. Results and Discussion

---

Table 4.8 — continued

$K^\pi$	Configuration	Energy (keV)					
		$\nu$	$\pi$	$E_{qp}$	$E_{res}^a$	$E_{calc}$	$E_{expt}$
13 <sup>-</sup> $\frac{11}{2}^+$ [615], $\frac{3}{2}^-$ [512]			$\frac{7}{2}^+$ [404], $\frac{5}{2}^+$ [402]	3396	-339	3057	—
14 <sup>+</sup> $\frac{11}{2}^+$ [615], $\frac{3}{2}^-$ [512]			$\frac{9}{2}^-$ [514], $\frac{5}{2}^+$ [402]	3215	-63	3152	—
14 <sup>-</sup> $\frac{11}{2}^+$ [615], $\frac{7}{2}^-$ [503] $\frac{7}{2}^-$ [514], $\frac{3}{2}^-$ [512]				3940	-168	3772 (3715) (+57)	
15 <sup>+</sup> $\frac{11}{2}^+$ [615], $\frac{9}{2}^+$ [624] $\frac{7}{2}^-$ [503], $\frac{3}{2}^-$ [512]				3500	+80	3580	
15 <sup>-</sup> $\frac{11}{2}^+$ [615], $\frac{7}{2}^-$ [503]			$\frac{7}{2}^+$ [704], $\frac{5}{2}^+$ [402]	3808	-66	3742 (3862) (-120)	
16 <sup>+</sup> $\frac{11}{2}^+$ [615], $\frac{7}{2}^-$ [503]			$\frac{9}{2}^-$ [514], $\frac{5}{2}^+$ [402]	3627	-87	3540	—
17 <sup>-</sup> $\frac{11}{2}^+$ [615], $\frac{9}{2}^+$ [624]			$\frac{9}{2}^-$ [514], $\frac{5}{2}^+$ [402]	3804	-42	3762 (3862) (-100)	
17 <sup>+</sup> $\frac{11}{2}^+$ [615], $\frac{9}{2}^-$ [505]			$\frac{9}{2}^-$ [514], $\frac{5}{2}^+$ [402]	4350	-70	4280	—
18 <sup>-</sup> $\frac{11}{2}^+$ [615], $\frac{9}{2}^+$ [624]			$\frac{9}{2}^-$ [514], $\frac{7}{2}^+$ [404]	4639	-8	4631	—
18 <sup>+</sup> $\frac{11}{2}^+$ [615], $\frac{9}{2}^+$ [624] $\frac{9}{2}^-$ [505], $\frac{7}{2}^-$ [503]				4651	+274	4925	—
19 <sup>-</sup> $\frac{11}{2}^+$ [615], $\frac{7}{2}^-$ [503]			$\frac{11}{2}^-$ [505], $\frac{9}{2}^-$ [514]	5034	-44	4990	—
20 <sup>+</sup> $\frac{11}{2}^+$ [615], $\frac{9}{2}^+$ [624]			$\frac{11}{2}^-$ [505], $\frac{9}{2}^-$ [514]	5211	+45	5256	—

<sup>a</sup> Residual interaction energies are taken from Ref.[132].

<sup>b</sup> Calculated energy minus experimental energy.

Blocked BCS Nilsson-type, multi-quasiparticle calculations, as described by Jain *et al.* [129], have been performed for  $^{184}\text{W}$ . The neutron and proton monopole pairing strengths were chosen as  $G_\nu = 21.5 \text{ MeV}/A$  and  $G_\pi = 23.1 \text{ MeV}/A$  respectively. The neutron value is that used for the even-even isotope  $^{186}\text{Os}$  [134] and the proton value is chosen to be 1.6 MeV/A higher, consistent with Ref. [129]. Deformation parameters of  $\varepsilon_2=0.216$  and  $\varepsilon_4=0.061$  [130] have been used, and an axially symmetric potential assumed. The single-particle energies were adjusted to reproduce the 1-quasineutron energies in  $^{183}_{74}\text{W}_{109}$  and  $^{185}_{74}\text{W}_{111}$  and the 1-quasiproton energies in  $^{183}_{73}\text{Ta}_{110}$  and  $^{185}_{75}\text{Re}_{110}$  [66, 131]. The averages of these single-particle energies were used for  $^{184}_{74}\text{W}_{110}$ . Residual nucleon-nucleon interactions using the Gallagher-

Moskowsky coupling rules [15, 16, 132] are included. The results for the most energetically favoured 2- and 4-quasiparticle states are shown in Table 4.8.

In Table 4.8 the energy of the 2480 keV state is (tentatively) compared with the energy of the  $K^\pi = 10^+_{2\nu}$  state, which has a calculated energy closest to that observed experimentally. Note that there are no plausible 2-quasiparticle arrangements available to make an energetically favoured  $K^\pi = 9^+$  configuration. The lowest predicted  $K^\pi = 9^+$  state lies at 3501 keV, more than 1 MeV above the observed 2480 keV level. Both  $K^\pi = 8^-$  and  $9^-$  configurations would lead to energy disparities of  $-208$  and  $-229$  keV (or  $+82$  keV for the  $K^\pi = 9^-_{2\nu}$  configuration) though cannot be ruled out.

There are several 4-quasiparticle states for which the measured excitation energy of 3862 keV lies within  $<150$  keV of the calculated configurations, specifically the  $K^\pi = 15^-$  and  $17^-$  arrangements. The calculated  $K^\pi = 14^-$  and  $15^-$  states have energies corresponding approximately to those of the 3715 and 3862 keV levels in Fig 4.20 and could be linked by a low-energy  $M1$  transition.

The observation of the 3862 keV,  $t_{1/2} = 188(38)$  ns isomer in  $^{184}\text{W}$  completes the tungsten 4-quasiparticle isomer systematics which now span the well-deformed prolate region ranging from  $^{176}_{74}\text{W}_{102}$  to  $^{186}_{74}\text{W}_{112}$  [133, 66, 118, 123, 135]. In order to quantify the trends across this range, blocked BCS calculations have been performed for the even-even tungsten isotopes,  $A = 176 \rightarrow 190$  with fixed monopole pairing strengths of  $G_\nu = 0.1236$  MeV and  $G_\nu = 0.1291$  MeV (equivalent to  $G_\nu = 22.5$  MeV/ $A$  and  $G_\pi = 23.5$  MeV/ $A$  for  $^{182}\text{W}$ ). These pairing strengths were chosen to reproduce the 4-quasiparticle energies in  $^{182}\text{W}$ , the heaviest W isotope for which firm configuration assignments have been made [123]. Deformation parameters have been taken from Ref. [130] and no adjustment of the single-particle energies was made. The results for the most yrast 4-quasiparticle isomers are shown in Fig 4.23. Note that residual nucleon-nucleon interactions have been included.

The overall trends and magnitudes in the excitation energies are well reproduced by the calculations, across the whole range spanned by the experimental data. Even

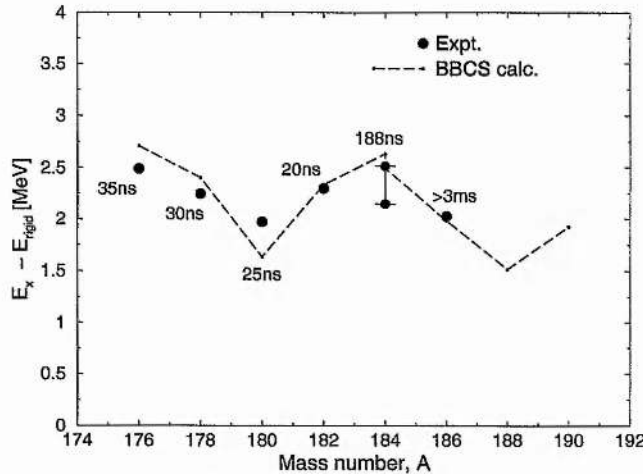


Figure 4.23: Tungsten low-lying 4-quasiparticle isomer systematics for  $A = 176 \rightarrow 190$ . Filled circles represent experimental energies, and the dotted line denotes the corresponding energies from the blocked BCS calculations (see text for details). A rigid rotor reference energy (appropriate for the deformation) has been subtracted in all cases. For  $^{184}\text{W}$  both the data and calculation cover 2 scenarios for  $K = 15$  and  $K = 17$ . Measured half-lives are quoted for all of the experimentally observed states.

for  $^{176}\text{W}$ , 6 mass units from  $^{182}\text{W}$  for which the pairing strengths were chosen, the calculated and experimental energies agree within 220 keV. Though making extrapolations always has inherent uncertainties, these results imply the existence of energetically favoured 4-quasiparticle states in the neutron-rich nucleus  $^{188}\text{W}$  and also, though somewhat less favoured, in the more exotic  $^{190}\text{W}$  nuclide. The states in question are  $K^\pi = 15^-$ ,  $E_{calc} = 2832$  keV ( $^{188}\text{W}$ ) and  $K^\pi = 17^-$ ,  $E_{calc} = 3586$  keV ( $^{190}\text{W}$ ). The possibility of long-lived yrast traps existing in  $^{188}\text{W}$  and  $^{190}\text{W}$  is topical as these nuclei are now within reach of current experimental facilities, via, for example, multi-nucleon transfer from osmium targets, or relativistic fragmentation [136].

## 4.4 Study of $^{198}_{\text{Pt}}$

The heaviest  $\beta$ -stable platinum isotope,  $^{198}\text{Pt}$ , was used as a target for the reaction studied in this thesis to populate neutron-rich nuclei around mass 190. This nucleus was studied looking at both in-beam and out-of-beam  $\gamma$ - $\gamma$  coincidences. The former allowed the study of the highest spins populated and the latter allowed the identification of a new high spin isomer.

### 4.4.1 Prompt $\gamma$ Rays in $^{198}\text{Pt}$

Figure 4.24 shows the level scheme for  $^{198}\text{Pt}$  obtained by looking at  $\gamma$ - $\gamma$  prompt coincidences. Some selected gates of the prompt Doppler corrected  $\gamma$  rays for  $^{198}\text{Pt}$  are shown in Fig. 4.25. All the levels for which spin-parity assignments are given in Fig. 4.24, have been observed earlier [99], with the exception of the 802 and 813 keV transitions.

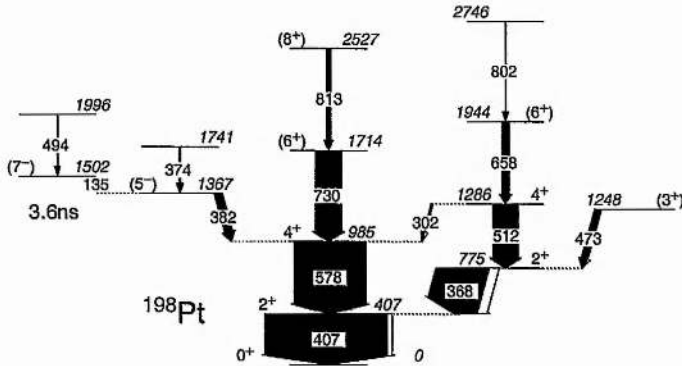


Figure 4.24: Level scheme of  $^{198}\text{Pt}$ , obtained by looking at prompt  $\gamma$ - $\gamma$  coincidences, including the previously unreported 813 and 802 keV transitions. The widths of the arrows are proportional to the observed relative  $\gamma$ -ray intensity (black) and the electron conversion intensity (white).

Prior to this work the highest spin reported for  $^{198}\text{Pt}$  in the ground band was ( $6^+$ ) at 1714 keV excitation energy [137]. The spin and parity assignments for the 1714 keV level were deduced from the comparison of the experimental data with theoretical results obtained using the interacting boson model approximation and

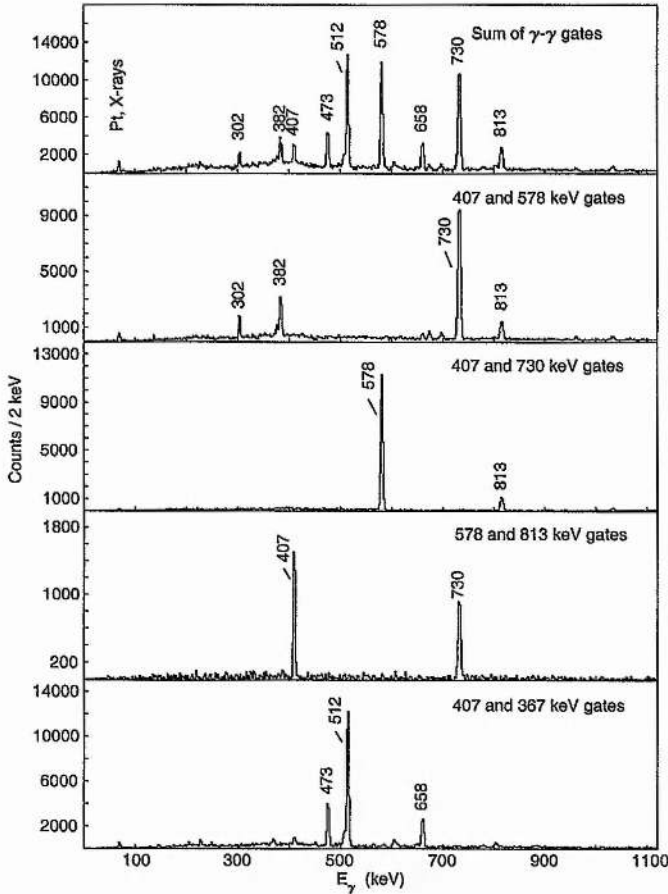


Figure 4.25: Background subtracted prompt  $\gamma$ -ray spectra for  $^{198}\text{Pt}$ . These spectra are software gated with a condition on the time range  $\Delta t = \pm 45\text{ns}$  with respect to the detection of the recoils.

systematics of the even platinum isotopes [137]. In the current work the 813 keV transition has been identified to de-excite the proposed highest spin state identified, which has been assigned tentatively a spin-parity of  $(8^+)$ .

As in the case of  $^{136}\text{Ba}$  some  $\gamma$  multipolarity information could be extracted for the prompt 813 keV transition, from the angular distribution. The  $A_2$  coefficient (the  $A_4$  coefficient is neglected in the fit), see Equation 1.34, for the 813 keV transition is  $0.22 \pm 0.09$ , from which it can be concluded that it is a quadrupole transition within one standard deviation. The 2746 keV level decaying via a 802 keV  $\gamma$ -ray is reported for the first time in the current work and is observed to be in coincidence with the

**Table 4.9:** Energies, assignments and relative in-beam intensities, for the transitions observed in  $^{198}\text{Pt}$ . The FWHM of the Doppler corrected transition energies is approximately 1%.

$E_\gamma$ (keV)	$E_i$	$E_f$	$I_i^\pi$	$I_f^\pi$	$I_\gamma$ (delayed)
134.7	1502	1367	(7 <sup>-</sup> )	(5 <sup>-</sup> )	3(1)
301.5	1286	985	4 <sup>+</sup>	4 <sup>+</sup>	5(1)
367.6	775	407	2 <sup>+</sup>	2 <sup>+</sup>	136(5)
374.3	1741	1367		(5 <sup>-</sup> )	4(1)
382.1	1367	985	(5 <sup>-</sup> )	4 <sup>+</sup>	21(2)
407.2	407	0	2 <sup>+</sup>	0 <sup>+</sup>	320(8)
473.4	1248	775	(3 <sup>+</sup> )	2 <sup>+</sup>	17(1)
494.0	1996	1502		(7 <sup>-</sup> )	2(1)
511.7	1286	775	4 <sup>+</sup>	2 <sup>+</sup>	67(2)
577.9	985	407	4 <sup>+</sup>	2 <sup>+</sup>	185(6)
657.8	1944	1286	(6 <sup>+</sup> )	4 <sup>+</sup>	19(1)
729.5	1714	985	(6 <sup>+</sup> )	4 <sup>+</sup>	83(3)
801.8	2746	1944			2(1)
812.6	2527	1714	(8 <sup>+</sup> )	(6 <sup>+</sup> )	11(1)

658 and 512 keV transitions that belong to the  $\gamma$  band. Unfortunately, it was not possible to conclude anything about the multipolarity of the 802 keV prompt transition, from the study of the angular distributions. For the 658 keV transition, the  $A_2$  coefficient was found to be  $0.23 \pm 0.09$ , which is in good agreement with a quadrupole transition within one standard deviation. The energies and intensities of the prompt transitions observed are given in Table 4.9.

#### 4.4.2 Isomeric State in $^{198}\text{Pt}$

Examining delayed  $\gamma - \gamma$  coincidences an isomer has been identified in  $^{198}\text{Pt}$ . Figure 4.26 shows all the transitions below the isomer, the known contaminants have been indicated next to the  $\gamma$ -ray transition energy. The 813 keV transition, decaying from the proposed  $(8^+)$ , can be clearly identified in Fig. 4.26.

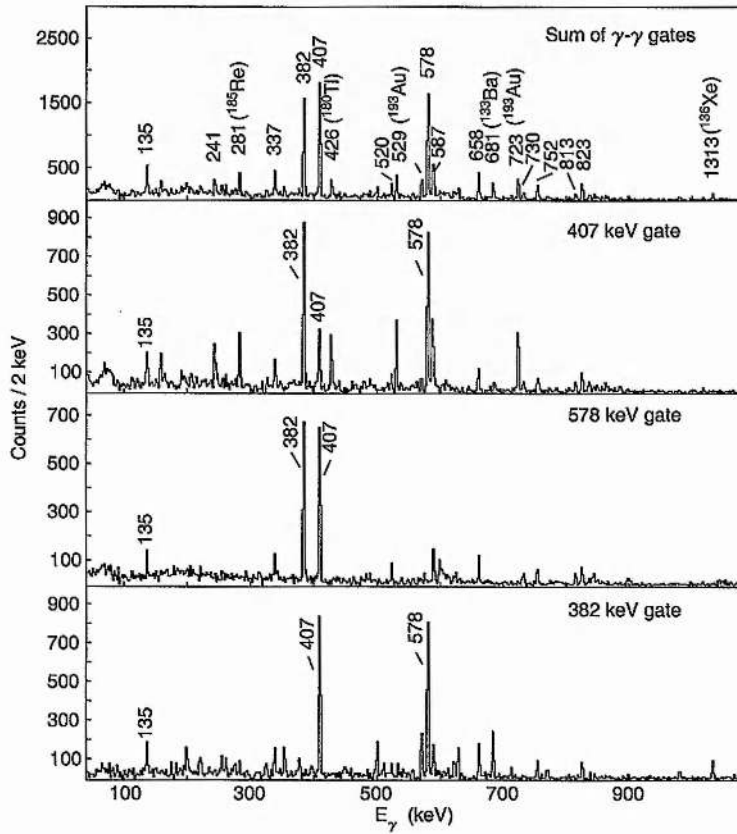


Figure 4.26: Background subtracted delayed  $\gamma$ -ray spectra for  $^{198}\text{Pt}$ . The time condition is that the  $\gamma$  rays are observed in the time range  $\Delta t = 30 - 150$  ns with respect to the detection of the two binary fragments.

Figure 4.27 shows the level scheme that has been deduced in the present work, two new bands have been built on the top of the  $(7^-)$  isomeric state, which has a half-life of 3.6 ns [99]. The 752 keV transition connects the two bands, aiding with the experimental ordering of the levels. The structure above the  $(7^-)$  isomer

## Chapter 4. Results and Discussion

---

is connected to the ground-state band via a 385 keV transition, in addition to the previously known 382 keV transition. Unfortunately the lack of angular distribution information for delayed  $\gamma$  rays, prevents a solid interpretation for the structure of these states. The spin and parities assigned are tentative. Although for example in the case of the 658 keV transition, the energy is consistent with collective  $E2$  transitions but the following transitions 520 and 337 keV are given a tentative  $\Delta I = 1$ .

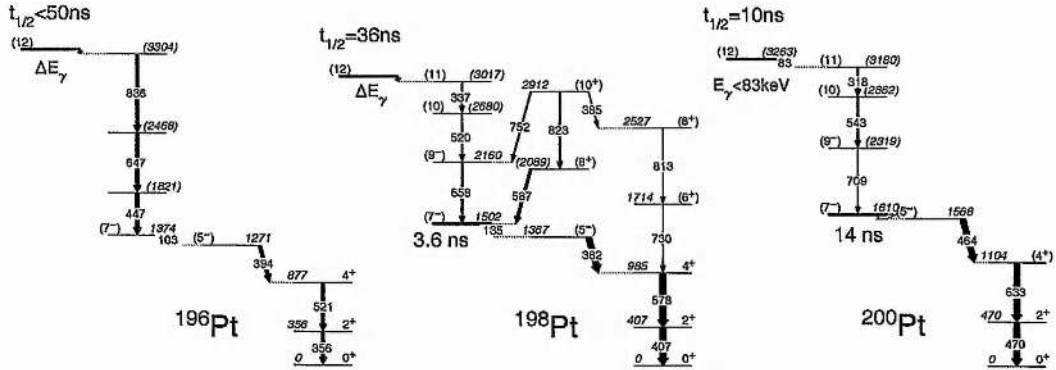


Figure 4.27: Level scheme of  $^{196}\text{Pt}$  (left). Level scheme of  $^{198}\text{Pt}$  (middle), obtained from delayed  $\gamma - \gamma$  coincidences. It shows the  $36 \pm 2$  ns isomer. The widths of the arrows are proportional to the relative  $\gamma$ -ray intensity. Level scheme of  $^{200}\text{Pt}$  (right), taken from [139].

Figure 4.27 shows the level scheme for  $^{198}\text{Pt}$  (middle), for  $^{196}\text{Pt}$  (left) [138] and for  $^{200}\text{Pt}$  (right) studied via fragmentation [139]. The level scheme for  $^{196}\text{Pt}$ , up to the 3304 keV state, is presented as the authors proposed it more than 30 years ago [138], although the 447, 647 and 836 keV transitions could be reordered in principle. The  $^{198}\text{Pt}$  data presents an isomer with a half-life of  $36 \pm 2$  ns (see Fig. 4.28), which was obtained by fitting an exponential decay curve plus a constant background to germanium TDC spectra double gated by transitions following the de-excitation of the isomeric state. The excitation energy of the isomer in  $^{198}\text{Pt}$  is suggested to be above the 3017 keV state, see Fig. 4.27. The isomeric nature of the state in  $^{198}\text{Pt}$  can be explained if it decays by one or more low energy transitions, not observed in experiment, to the 3017 and 2912 keV states. This would follow the same pattern

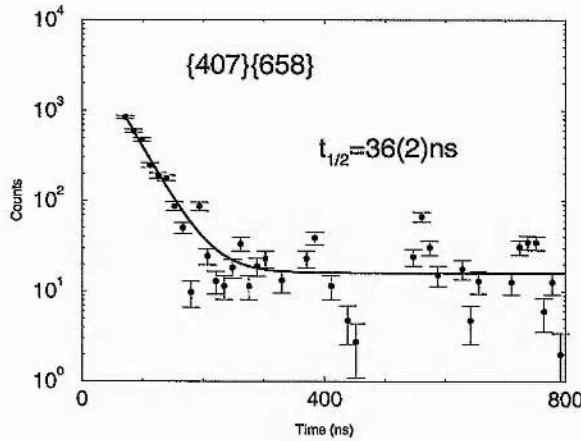


Figure 4.28: Gamma-ray decay curve used to determine the half-life of the ( $I^\pi = 12^+$ ) isomeric state in  $^{198}\text{Pt}$  ( $t_{1/2} = 36 \pm 2$  ns), gated by pairs of double  $\gamma$ -ray gates.

as in  $^{200}\text{Pt}$ . In previous studies of  $^{196}\text{Pt}$  [138], the 447, 647 and 836 keV transitions were not found to be coming from the de-excitation of an isomeric state, which crudely breaks the platinum systematics for  $^{198}\text{Pt}$ ,  $^{196}\text{Pt}$  and  $^{200}\text{Pt}$ . However, this can be explained because in the case of the  $\beta$  decay of  $^{196}\text{Ir}$  feeding excited states in  $^{196}\text{Pt}$ , the highest energy state populated was the 3304 keV level, therefore the isomer would not be populated. In the current work an isomer has been observed in  $^{196}\text{Pt}$  with an upper limit of the half-life  $t_{1/2} < 50$  ns, the delayed  $\gamma$  ray spectra can be seen in Fig. 4.5. An isomeric state very close in energy to the 3304 keV state is suggested, the decay is predicted to be via a low energy transition to the 3304 keV state, equivalent to that proposed in  $^{198}\text{Pt}$ . The energies and intensities of the transitions observed are given in Table 4.10.

#### 4.4.3 Discussion of $^{198}\text{Pt}$

Since  $^{198}\text{Pt}$  is a near spherical nucleus (the ground state  $\beta_2$  deformation parameter is predicted to be -0.133 [114]) BBCS calculations can not be carried out. The negative parity states ( $7^-$ ) and ( $5^-$ ) in the even platinum isotopes have been previously interpreted as semi-decoupled states of a fully aligned  $i_{13/2}$  neutron and a poorly aligned low- $j$  neutron orbital [78, 140]. Even if no calculations to interpret this nu-

Table 4.10: Energies, assignments and relative out-of-beam intensities, for the transitions observed in  $^{198}\text{Pt}$ . The uncertainties in the transition energies are  $\pm 0.2$  keV.

$E_\gamma$ (keV)	$E_i$	$E_f$	$I_i^\pi$	$I_f^\pi$	$I_\gamma$ (delayed)
134.6	1502	1367	(7 $^-$ )	(5 $^-$ )	15(3)
336.5	3017	2680	(12 $^+$ )	(11 $^-$ )	18(2)
381.8	1367	985	(5 $^-$ )	4 $^+$	86(5)
384.5	2912	2527	(10 $^+$ )	(8 $^+$ )	11(2)
407.2	407	0	2 $^+$	0 $^+$	96(7)
520.1	2680	2160	(11 $^-$ )	(9 $^-$ )	20(2)
577.8	985	407	4 $^+$	2 $^+$	96(7)
586.8	2089	1502	(8 $^+$ )	(7 $^-$ )	40(3)
658.2	2160	1502	(9 $^-$ )	(7 $^-$ )	28(3)
729.2	1714	985	(6 $^+$ )	4 $^+$	15(3)
752.0	2912	2160	(10 $^+$ )	(9 $^-$ )	18(2)
813.1	2527	1714	(8 $^+$ )	(6 $^+$ )	10(2)
823.1	2912	2089	(10 $^+$ )	(8 $^+$ )	26(2)

cleus can be done, still a few interesting speculations can be made. Reference [139] reported a high-spin ( $I \approx 12$ ) configuration for  $^{200}\text{Pt}$  (see Fig. 4.27). It is argued that the systematic observation of  $I^\pi = 12^+$  nanosecond isomers [66, 141] based upon two rotation-aligned neutrons in  $i_{\frac{13}{2}}$ ,  $(\nu i_{\frac{13}{2}})^2$  and the high excitation energy of the isomeric state, in less neutron-rich platinum and mercury nuclei, supports a similar interpretation in the case of  $^{198}\text{Pt}$ . Looking at the systematics of the platinum isotopes, see Fig. 4.27, clear similarities can be observed in the level schemes. Therefore an  $I^\pi = (12^+)$  character is tentatively assigned to the isomeric state in  $^{198}\text{Pt}$ .

## 4.5 Study of Complementary Fragments

In a binary reaction, the  $\gamma$  rays detected in each event can come from one or both of the fragments and a priori, there is no way to assign a  $\gamma$  ray to a specific fragment. In the case of prompt  $\gamma$  rays it is possible to distinguish whether the  $\gamma$  ray comes from TLFs or BLFs, (see *Section 3.2.2*). Therefore it is possible to study the distribution of the binary partners using delayed-prompt coincidences. An isomer in one of the binary partners and prompt feeding in the other is needed, a situation which is quite likely for the region of nuclei populated in the reaction studied. Here the way to proceed is to gate on delayed  $\gamma$ -ray transitions from well-known isomers and project the prompt  $\gamma$  rays from the binary fragment. For this purpose a delayed-prompt matrix was produced, where the prompt  $\gamma$  rays are Doppler corrected for TLFs, see Table 3.2.

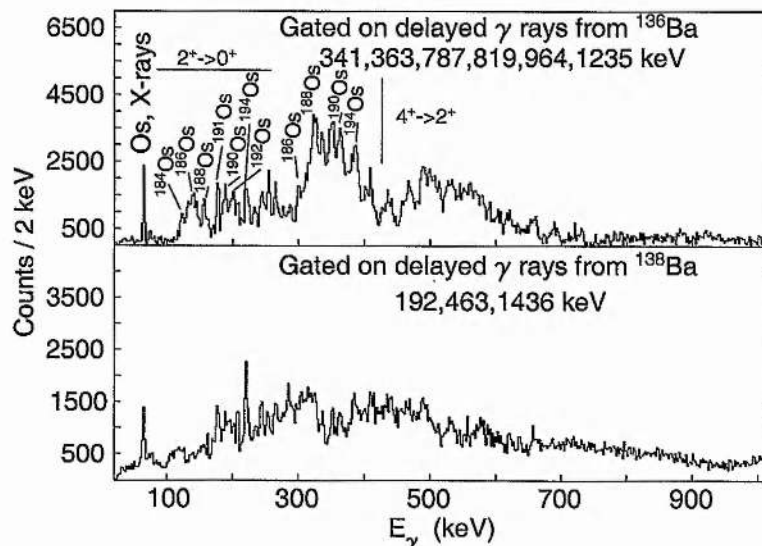


Figure 4.29: Background subtracted prompt  $\gamma$ -ray spectra for osmium isotopes, gated on delayed barium  $\gamma$  rays. The upper panel is gated by  $^{136}\text{Ba}$  delayed  $\gamma$  rays, whose binary partner is  $^{198}\text{Os}$  and the lower panel is gated by  $^{138}\text{Ba}$  delayed  $\gamma$  rays, whose binary partner is  $^{196}\text{Os}$ .

Figure 4.29 shows background subtracted prompt  $\gamma$ -ray spectra for osmium isotopes, gated on the delayed  $\gamma$  rays of the barium binary partner. The delayed gates

have been chosen carefully, so that there is no contamination from other nuclei at these energies. The osmium X-rays are clearly visible in the spectra and there are no other obvious X-ray lines from other nuclei. Therefore the gates taken to create the spectra are clean and it is mainly prompt Doppler corrected osmium  $\gamma$  rays which are projected. The large background in the spectra is due to delayed  $\gamma$  rays that have been Doppler corrected with the incorrect  $\beta$  value and are thus smeared out.

Figure 4.30 shows background subtracted prompt  $\gamma$ -ray spectra for platinum isotopes, gated on delayed  $\gamma$  rays of the xenon binary partner. The platinum X-rays are clearly visible in all the spectra. The upper spectrum is very clean in terms of the platinum isotopes, where the most prominent peak is the  $2^+ \rightarrow 0^+$  transition from the target nucleus,  $^{198}\text{Pt}$ .

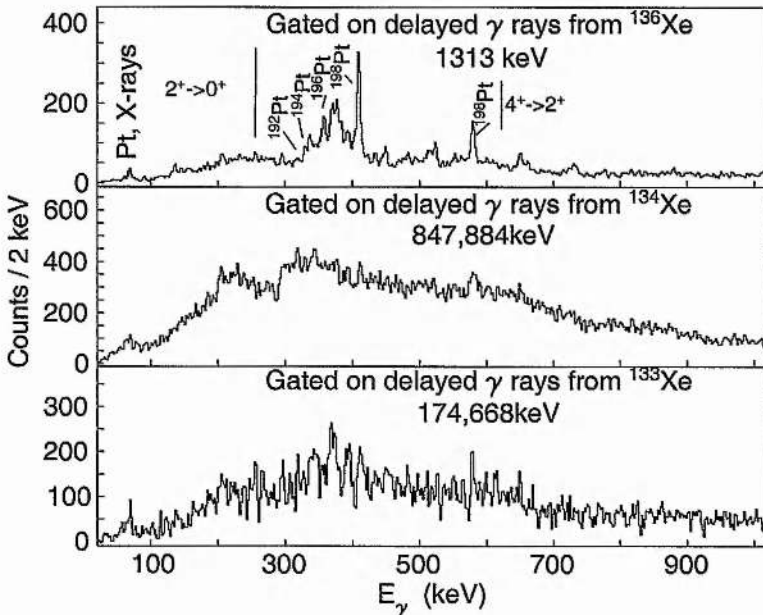


Figure 4.30: Background subtracted prompt  $\gamma$ -ray spectra for platinum isotopes, gated by delayed xenon  $\gamma$  rays. The upper panel is gated by  $^{136}\text{Xe}$  delayed  $\gamma$  rays, whose binary partner is  $^{198}\text{Pt}$ . The middle panel is gated by  $^{134}\text{Xe}$  delayed  $\gamma$  rays, whose binary partner is  $^{200}\text{Pt}$  and the lower panel is gated by  $^{133}\text{Xe}$  delayed  $\gamma$  rays, whose binary partner is  $^{201}\text{Pt}$ . Note that xenon and platinum are binary partners.

Figures 4.29 and 4.30 show characteristic  $\gamma$  rays from a range of osmium and

platinum isotopes respectively. The intensity of each of these  $\gamma$  rays is, a priori, related to the probability of neutron evaporation from the hot binary fragment produced after the reaction. This can be quantified using the *Relative Yield* parameter, calculated using the efficiency and internal conversion corrected intensity of the  $2^+ \rightarrow 0^+$   $\gamma$  ray for each even-even osmium isotope. In the case of  $^{191}\text{Os}$  the intensity of the  $11/2^+ \rightarrow 9/2^-$ ,  $E1$   $\gamma$  ray has been used. Each value has been normalised such that the *Relative Yield* for the  $^{194}\text{Os}$  isotope has a value of 10.

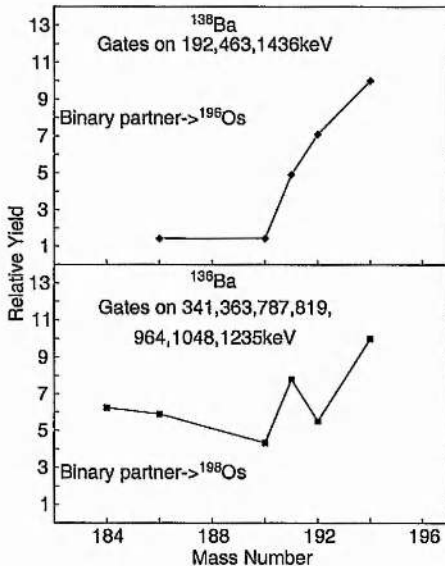


Figure 4.31: Relative Yield for osmium isotopes. The upper panel shows the Relative Yield for osmium isotopes gated by  $^{138}\text{Ba}$ , whose binary partner is  $^{196}\text{Os}$  which is unknown. The lower panel shows the Relative Yield for osmium isotopes gated on  $^{136}\text{Ba}$ , whose binary partner is  $^{198}\text{Os}$ .

The study of the *Relative Yield* parameter was used first in fission experiments [142, 143] to study the isotopes produced in the fission process and to identify the isotopes of interest. Figure 4.31 shows the *Relative Yield* for different osmium isotopes, ranging from  $^{184}\text{Os}$  to  $^{194}\text{Os}$ , gated on delayed  $\gamma$  rays from  $^{138}\text{Ba}$  (upper panel) and  $^{136}\text{Ba}$  (lower panel). The plots show the maximum yield for  $^{194}\text{Os}$ . Unfortunately heavier osmium isotopes could not be investigated, since their  $\gamma$  ray transitions are not known in the literature. If heavier isotopes could be identified a

peak would be expected centred on the most populated isotope. In this manner one could determine the most likely number of evaporated neutrons.

The *Relative Yield* calculated should not be taken as strictly defined probabilities of neutron evaporation of the excited fragments, since most of these osmium isotopes, for example  $^{190}\text{Os}$ ,  $^{191}\text{Os}$ ,  $^{192}\text{Os}$  and  $^{194}\text{Os}$ , have isomers. Therefore the intensity trapped in these isomers, which is not known, reduces the *Relative Yield*, thus biasing the results. It could be possible to do the same *Relative Yield* analysis for the platinum isotopes. However, in this case the Yield due to Coulomb scattering for the  $^{198}\text{Pt}$  isotope should be included. In addition, some of the platinum isotopes have isomers (e.g.  $^{192}\text{Pt}$  and  $^{198}\text{Pt}$ ), therefore detailed information on the average neutron evaporation could not be extracted, clearly in the current work.

#### 4.5.1 $^{196}\text{Os}$ or Not $^{196}\text{Os}$ , That Is the Question.

Figure 4.29 shows a strong transition at 283 keV from one of the osmium isotopes. This energy happens to be in the energy range expected for the  $2^+ \rightarrow 0^+$  transition for  $^{196}\text{Os}$ , which was measured to be  $300 \pm 20\text{keV}$  [144], and it might be expected in this spectrum, see Fig. 4.32 (left). The  $^{196}\text{Os}$  isotope was previously studied via two proton pickup on  $^{198}\text{Pt}$  [144], using the reaction  $^{198}\text{Pt}(^{14}\text{C}, ^{16}\text{O})^{196}\text{Os}$ .

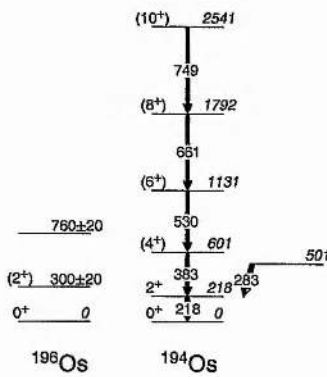


Figure 4.32: Level scheme of  $^{196}\text{Os}$ , taken from [144] (left) and level scheme for  $^{194}\text{Os}$ , taken from [145], including the new 283 keV transition deduced from the present work (right).

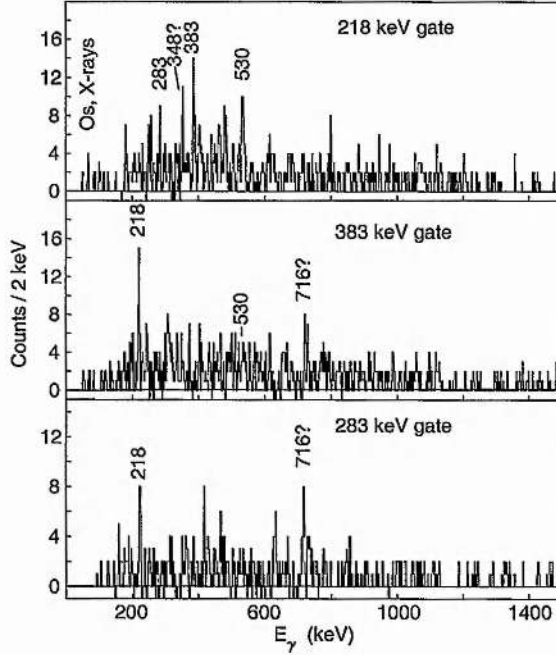


Figure 4.33: Background subtracted prompt  $\gamma$ -ray spectra for  $^{194}\text{Os}$ . These spectra have been obtained by looking at  $\gamma$ - $\gamma$  prompt coincidences. The  $\gamma$ - $\gamma$  prompt matrix has been gated on the delayed 192, 463 and 1436 keV  $\gamma$  rays from the binary partner  $^{138}\text{Ba}$ .

A delayed-prompt-prompt cube, where the prompt  $\gamma$  rays are Doppler corrected for TLFs (see Table 3.2), was produced to elucidate whether the 283 keV transition corresponds to the  $2^+ \rightarrow 0^+$  transition in  $^{196}\text{Os}$ . Figure 4.33 shows background subtracted prompt  $\gamma$ -ray spectra gated on the delayed 192, 463 and 1436 keV  $\gamma$  rays from the binary fragment  $^{138}\text{Ba}$ . The top panel in Fig. 4.33 shows the  $\gamma$ -ray spectra gated on the prompt 218 keV,  $2^+ \rightarrow 0^+$  transition in  $^{194}\text{Os}$  and shows the 383 keV  $4^+ \rightarrow 2^+$ , the 530 keV  $6^+ \rightarrow 4^+$  and the unplaced 283 keV transitions. The middle panel of the former figure shows the  $\gamma$ -ray spectra gated on the prompt 383 keV,  $4^+ \rightarrow 2^+$  transition in  $^{194}\text{Os}$  which shows the 218 keV  $2^+ \rightarrow 0^+$  and the 530 keV  $6^+ \rightarrow 4^+$  transitions but not the unplaced 283 keV transition. The lower panel shows the  $\gamma$ -ray spectra gated on the prompt unplaced 283 keV transition. This gate is in coincidence with the 218 keV transition from  $^{194}\text{Os}$ . Therefore the conclusion

is that the 283 keV transition probably belongs to  $^{194}\text{Os}$  and not to  $^{196}\text{Os}$ .

The final level scheme for  $^{194}\text{Os}$  deduced in the current work can be seen in Fig. 4.32 (right). Figure 4.33 shows  $\gamma$  rays at energies 348 and 716 keV that due to lack of statistics could not be placed in the current level scheme. The highest spin state observed in the current work for  $^{194}\text{Os}$  is the ( $10^+$ ) 2541 keV state, previously reported by Wheldon *et al.* [145]. This state has been found to be isomeric in the current work and an upper limit to the half-life has been obtained namely  $t_{1/2} < 90\text{ns}$ .  
*(or fed by an isomer)*

## 4.6 Angular Momentum Transfer Determination

The knowledge of entry spin distributions and the related angular momentum population in deep inelastic reactions has a significant bearing on the potential for using such reactions in the study of high-spin states in neutron-rich nuclei. While some effort was made in this area in the 1970s (*e.g.* [40]), there have been only limited recent studies which utilise the power of large-scale  $\gamma$ -ray arrays for channel selection in attacking this problem (*e.g.* [35, 146]). In order to better understand multinucleon transfer reactions and the transition between quasi-elastic and deep-inelastic processes, a study has been made of the average fold distribution versus the laboratory recoil scattering angle for various reaction products. To study the angular distribution of the fold in the reaction for different nuclei, two Ana cubes were created. The cubes created were delayed  $\gamma$  rays versus recoil scattering angle  $\theta$ , gated for either TLFs or BLFs versus Fold (see Table 3.2). To select the nuclei of interest, delayed  $\gamma$  rays from the nucleus of interest were used. Since the nuclei in this region have a number of well known isomeric states, this allows the study of a broad number of reaction channels, both close to and further from the beam and target nuclei.

The average fold for each angle, once gates for the nuclei of interest have been

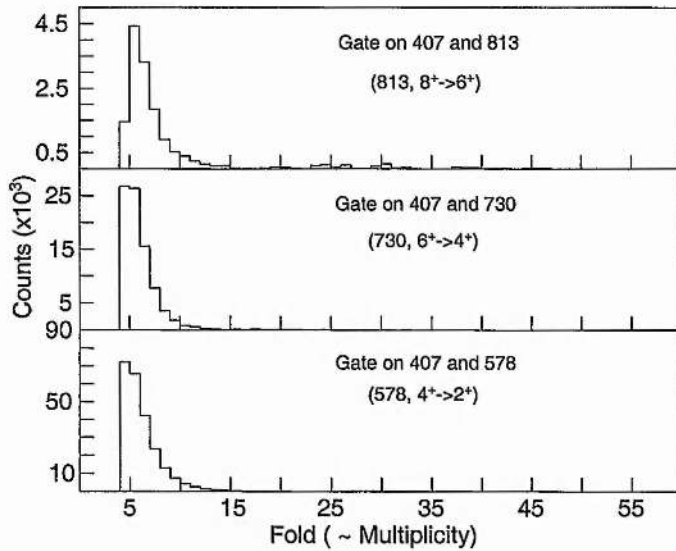


Figure 4.34: Fold distribution for different  $\gamma$ -ray transitions for the target nucleus,  $^{198}\text{Pt}$ . Low fold events clearly dominate, corresponding to Coulomb scattering. For the  $8^+ \rightarrow 6^+$  transition some events of higher fold start appearing, corresponding to some population from more inelastic processes.

set, was calculated as follows,

$$\langle F \rangle = \frac{\sum_i F_i I_i}{\sum_i I_i}$$

where  $I_i$  is the number of counts for a given fold  $F_i$ .

Before looking at the average fold angular distributions it is quite instructive to look at the fold distribution gated at different spins in the target nucleus,  $^{198}\text{Pt}$ . Figure 4.34 shows the fold distribution for various  $\gamma$  transitions up to the  $8^+$  state. In all cases, including the highest spin on which a gate can be set ( $8^+ \rightarrow 6^+$ ; 813keV), low fold events dominate, suggesting Coulomb scattering. For the  $8^+ \rightarrow 6^+$  transition some events associated with a higher fold start appearing, corresponding to inelastic processes.

Figure 4.35 shows the average fold distribution versus laboratory scattering recoil angle  $\theta$  for the beam  $^{136}\text{Xe}$  and the target  $^{198}\text{Pt}$ . Figure 4.35a shows, for  $^{136}\text{Xe}$ , a low-fold peak at forward angles. For  $^{198}\text{Pt}$  this peak is observed at larger angles. This peak most likely corresponds to Coulomb excitation, a process which produces

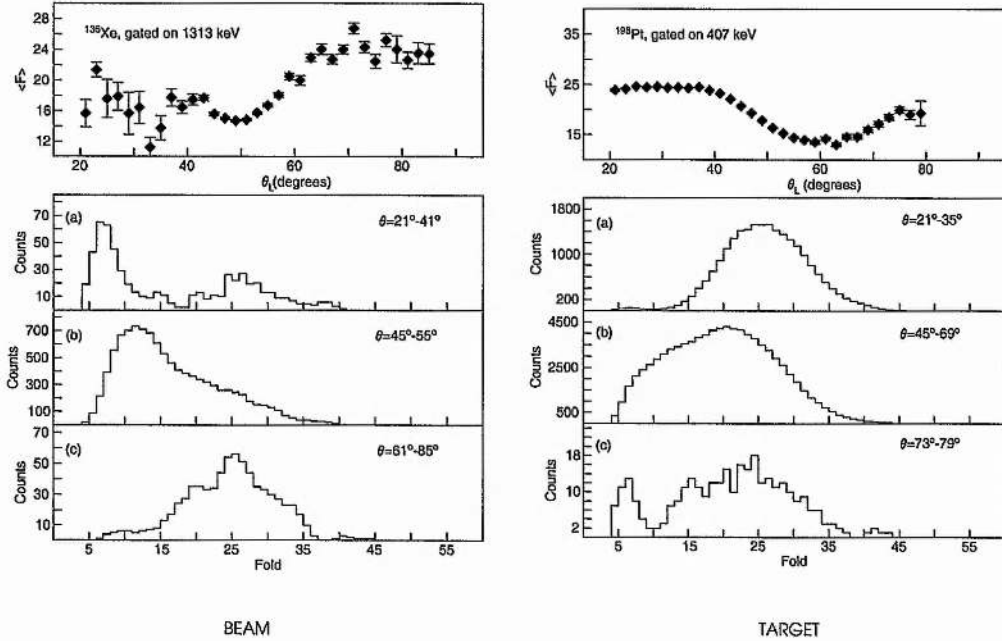


Figure 4.35: Average fold distribution versus laboratory scattering recoil angle  $\theta$  for the beam  $^{136}\text{Xe}$  (left) and the target  $^{198}\text{Pt}$  (right) nuclei. In the lower (a), (b), (c) spectra fold projections for various angular ranges is shown. These plots were made by gating on the delayed  $\gamma$  rays 1313 keV and 407 keV to select  $^{136}\text{Xe}$  and  $^{198}\text{Pt}$  respectively. Note that the estimated grazing angle of the reaction lies around  $50^\circ$ .

relatively low fold events. Figure 4.36 shows the average fold distribution versus laboratory scattering recoil angle  $\theta$  for  $^{136}\text{Ba}$ ,  $^{138}\text{Ba}$ ,  $^{125}\text{Sb}$  and  $^{138}\text{Ce}$ . Note that in all of the plots for BLFs at forward angles and at higher angles for TLFs, the statistics are much poorer. This is not a reaction mechanism effect but it is due to the lower efficiency of CHICO at these angular ranges as outlined in *Chapter 3*.

The  $\gamma$ -ray fold for an event gives a measure of the degree of inelasticity of the binary partner interaction. The greater the overlap and degree of transfer between the two fragments, the more angular momentum is transferred into the internal spins of the fragments [40]. The transfer of angular momentum in heavy ion collisions such as those described in this thesis can be studied in terms of the average fold versus

## Chapter 4. Results and Discussion

---

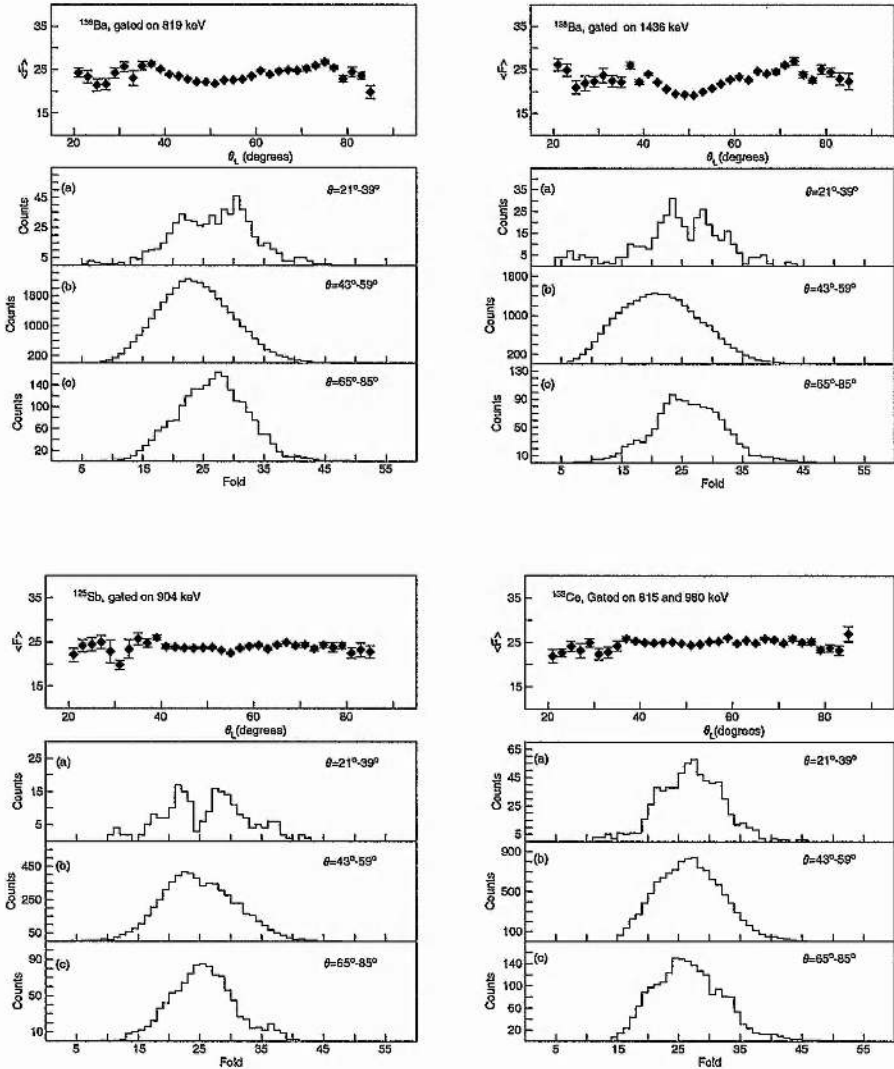


**Figure 4.36:** Average fold distribution versus laboratory scattering recoil angle  $\theta$  for  $^{136}\text{Ba}$  (top-left),  $^{138}\text{Ba}$  (top-right),  $^{125}\text{Sb}$  (bottom-left),  $^{138}\text{Ce}$  (bottom-right). In the lower (a), (b), (c) spectra a fold cut for various angular ranges is shown. These plots have been made gating on the delayed  $\gamma$  rays 819 keV, 1436 keV, 904 keV and (815, 980) keV to select  $^{136}\text{Ba}$ ,  $^{138}\text{Ba}$ ,  $^{125}\text{Sb}$  and  $^{138}\text{Ce}$  respectively. The number of minimum nucleons transfer to produce these nuclei in the reaction are: (+2p, +2n) onto the beam for  $^{136}\text{Ba}$ , (+2p) onto the beam for  $^{138}\text{Ba}$ , (-3p, -8n) from the beam for  $^{125}\text{Sb}$  and (+4p, -2n) from the beam for  $^{138}\text{Ce}$ .

the measured scattering angle of the recoils.

At the grazing angle the target and beam nuclei are expected to have peripheral contact and thus quasi-elastic events would be expected to dominate. Since such quasi-elastic reactions are expected to involve a relatively small transfer of angular momentum from the initial angular momentum into internal spins [42] the average multiplicity is expected to decrease in the vicinity of the grazing angle. This regime could be explained with the rolling mode. The transfer of angular momentum increases continuously with the degree of inelasticity [41], when the nuclei touch each other more solidly. If the contact time is long enough (*i.e.* deep inelastic collisions), the sticking limit ought to be reached [41].

The typical deduced  $\gamma$ -ray fold values of the order of 25, correspond to the *average* fold per event. It is worth noting that the fold distribution extends up to considerably higher values of 35 and greater, see Fig. 4.36. While some of this apparent increase simply reflects the response function of the GAMMASPHERE array, it is clear that significantly higher folds are populated in this mechanism, which bodes well for future high-spin studies using heavy-ion binary collisions.

# Chapter 5

## Conclusions and Future Work

This thesis is the result of the analysis of an experiment which was proposed to push our knowledge of neutron-rich nuclei. The reaction used to populate the neutron-rich nuclei of interest, was a deep-inelastic reaction between a thin self-supporting  $^{198}_{78}\text{Pt}$  target and an 850 MeV  $^{136}_{54}\text{Xe}$  beam. Nuclei around the beam and target masses have been studied. A contribution to the determination of angular momentum transfer in deep-inelastic reactions from a study of the fold angular distribution has also been presented in this thesis.

A large number of isomeric states have been identified in the beam and target-like regions. A number of previously unreported isomers populated in the target-like region have been observed in  $^{201}\text{Tl}$ ,  $^{195}\text{Au}$ ,  $^{198}\text{Pt}$ ,  $^{194}\text{Os}$ ,  $^{192}\text{Os}$ ,  $^{191}\text{Os}$  and  $^{184}\text{W}$ , while new isomers populated in the beam-like region include those in  $^{139}\text{La}$ ,  $^{136}\text{Ba}$ ,  $^{131}\text{I}$ ,  $^{133}\text{I}$  and  $^{127}\text{Sb}$ . The half-lives of these isomers have been reported.

An  $I^\pi = 10^+$  isomer has been reported for the first time in  $^{136}\text{Ba}$  at an excitation energy of 3357 keV. The assigned configuration is the two-neutron-hole  $(\nu h_{\frac{11}{2}})_{10^+}^{-2}$  arrangement, in good agreement with the shell model and pair-truncated shell model predictions and the systematics of the  $N = 80$  isotones. The increase in excitation energy of the  $10^+$  isomer and the decrease in the  $B(E2)$  values along the  $N = 80$  isotones can be understood qualitatively in terms of the single-particle excitation energy of the  $h_{\frac{11}{2}}$  neutron orbital. The identification of this  $10^+$  isomeric state

completes the systematics for the  $N = 80$  isotones from the  $Z = 50$  closed shell  $^{130}_{50}\text{Sn}$  to past the proton mid-shell at  $^{148}_{68}\text{Er}$ . Prompt decaying states above the isomer have also been identified and some limited multipolarity information obtained from  $\gamma$ -ray angular distributions. The barium isotopes from  $N = 70$  to 82 have been discussed in terms of the seniority scheme. It has been found that seniority is not a good quantum number to describe the  $B(E2)$  transition rates of barium isotopes unlike the situation in the tin isotopes ( $66 \leq N \leq 82$ ), which can be well described in the seniority scheme framework.

The  $^{184}\text{W}$  isotope has been studied and seniority-2 and -4 structures have been identified. Comparisons with blocked BCS Nilsson-type calculations suggest several candidates for the configurations of the newly observed states, the excitation energies of which are in close agreement with the measured values. A  $t_{1/2} = 188 \pm 38$  ns isomeric state at 3862 keV has been established and this fills the gap in the tungsten 4-quasiparticle isomer systematics from  $A=176$  to 186. The variation in the excitation energies of the yrast 4-quasiparticle isomeric states are well reproduced by blocked BCS calculations and suggest exciting possibilities for future work to study, for example,  $^{188}\text{W}$ , for which a highly favoured 4-quasiparticle state is predicted.

A tentative  $I^\pi = 12^+$  isomeric state has been identified in  $^{198}\text{Pt}$ . Block BCS calculations were not carried out for this nucleus since it is near spherical. The high-spin configuration of two rotation-aligned neutrons in  $i_{\frac{13}{2}}$  comes from the observation of  $I^\pi = 12^+$  nanosecond isomers in less neutron-rich platinum and mercury nuclei.

The study of complementary fragments has been used to quantify the *Relative Yield* of the binary partners. Specifically the osmium and platinum isotopes, whose binary partners are barium and xenon respectively, have been studied. The *Relative Yield* peaks for  $^{194}\text{Os}$ , but unfortunately heavier isotopes could not be investigated since they are unknown and they could not be identified in the present work. Looking at the complementary fragments of  $^{138}\text{Ba}$ , it was found that the 283 keV transition, which nicely fits into the expected range of energies for the  $2^+ \rightarrow 0^+$  in  $^{196}\text{Os}$ , was actually a transition in  $^{194}\text{Os}$ . No evidence for the  $^{196}\text{Os}$  isotope was found in the

current work.

The angular momentum transfer in this reaction has been investigated in terms of the average fold versus the scattering angle of the recoils. Some of these plots show a dip at the grazing angle which is understood in terms of quasi-elastic reactions dominating at those angles. The deep-inelastic reactions take over at angles away from the grazing angle. For nuclei far from the beam or the target, that can only be produced via deep-inelastic reactions no dip shows at the grazing angle.

In APPENDIX A of this thesis the work carried out with a highly segmented germanium prototype (36 segments) and the associated electronics for digitisation of the preamplifier signals have been described. Two different algorithms to extract the energy information are presented, the Moving Window Deconvolution (MWD) method and an exponential fitting of the signals. The MWD has been found to be stable, fast and it gives the best energy resolution, 3.5 keV for 1.332 MeV. A tracking algorithm showing results from simulated and experimental data is described. The results obtained for simulated and experimental data for 20 mm position resolution are shown. The P/T hardly improves when the single interaction events are not rejected, but it improves by approximately 70% if the single interaction events are rejected. The efficiency drops by approximately 30% when single events are rejected.

## Future Work

Although this experiment has contributed to improve our knowledge of neutron-rich nuclei, more effort has to be put into the study of neutron-rich nuclei far from stability at higher spins, since these nuclei show a wide and relevant range of nuclear structure phenomena such as triaxiality [147], *K*-isomerism [136] or prolate-oblate shape competition [145].

The use of heavier beams like U, Pb or Bi for multinucleon transfer reactions will lead to the population of higher spin states. For example the  $L_{max}$  put into the reaction for a  $^{208}_{82}\text{Pb}$  beam with an energy 25% above the Coulomb barrier impinging on a  $^{198}\text{Pt}$  target is 42% higher than for the reaction using a  $^{136}\text{Xe}$  beam, described in this thesis. In addition a higher mass beam, such as  $^{208}\text{Pb}$ , will lead

to a lower  $N/Z$  ratio. Therefore more neutron-rich nuclei, such as  $^{196}\text{Os}$ , are more likely to be populated than in the current work. Argonne National Laboratory with GAMMASPHERE and CHICO, could provide the infrastructure to perform such an experiment.

Another step forward in the study of exotic nuclei is the use of Radioactive Ion Beams, that will push even further the known boundary of neutron-rich nuclei. GANIL offers the experimental facilities, VAMOS and EXOGAM, to perform such experiments. These studies could be complemented by fragmentation stopped beams which could be carried out at GSI.

# Bibliography

- [1] A. Messiah, *Quantum Mechanics*, North-Holland, Amsterdam (1965).
- [2] M.G. Mayer *et al.*, Phys. Rev. **75**, 1969 (1949).
- [3] A. Poves and F. Nowacki, *Lecture Notes in Physics*, Springer, (2001).
- [4] K. Higashiyama, N. Yoshinaga and K. Tanabe, Phys. Rev. C **65**, 054317 (2002).
- [5] K. Higashiyama, N. Yoshinaga and K. Tanabe, Phys. Rev. C **67**, 044305 (2003).
- [6] F. Iachello and A. Arima, Phys. Lett. B **53**, 309 (1974).
- [7] R.F. Casten, *Nuclear Structure from a Simple Perspective*, Oxford Science Publications 2000.
- [8] J.J. Ressler *et al.*, Phys. Rev. Lett., submitted (2003).
- [9] M. Eisenberg and W. Greiner, *Microscopic Theory of the Nucleus*, North-Holland Publishing Company (1972).
- [10] W. Greiner, *Nuclear Models*, Springer-Verlag Berlin Heidelberg New York (1996).
- [11] S.G. Nilsson, *Dan. Mat.-Fys. Medd.* **29**, 16 (1995).
- [12] J. Bardeen, L.N. Cooper and J.R. Schrieffer, Phys. Rev. **108**, 1175 (1957).
- [13] B.R. Mottelsson and J.G. Valatin, Phys. Rev. Lett. **5**, 511 (1960).

## Bibliography

---

- [14] P. Ring and P. Schuck, *The Nuclear Many Body Problem*, Springer-Verlag, New York, Heidelberg, Berlin (1980).
- [15] C.J. Gallagher and S.A. Moszkowski, Phys. Rev. **111**, 1282, (1958).
- [16] K. Jain *et al.*, Phys. Lett. **B 322**, 27 (1994).
- [17] G.F. Knoll, *Radiation Detection and Measurement* (Wiley) Singapore (1989).
- [18] J.M. Blatt and V.F. Weisskopf, *Theoretical Nuclear Physics*, John Wiley and Sons Inc., New York (1952).
- [19] A. De Shalit and H. Feshbach, *Theoretical Nuclear Physics Vol 1: Nuclear Structure*, John Wiley and Sons Inc., New York (1974).
- [20] J. Kantele, *Heavy Ions and Nuclear Structure, vol 5, Nuclear Science Research Conferences Series*, B. Sikora and Z. Wilhem, Harwood, 391 (1984).
- [21] K.S. Krane, *Introductory Nuclear Physics*, John Wiley and Sons, New York (1998).
- [22] F. Rösel *et al.*, *Atomic Data and Nuclear Data Table* **21**, 91 (1978).
- [23] K. Siegbahn, *Alpha-, Beta-, and Gamma-Ray Spectroscopy*, North-Holland Publishing Company (1965).
- [24] E. Der Mateosian and A.W. Sunyar, *Atomic Data and Nuclear Data Table* **13**, 407 (1974).
- [25] P. Fröbrich and R. Lipperheide, *Theory of Nuclear Reactions*, Oxford, University Press (1996).
- [26] H. Freiesleben and J.V. Kratz, Phys. Rep. **106**, 1 (1984).
- [27] K. Van Bibber *et al.*, Phys. Rev. Lett. **38**, 334 (1977).
- [28] R. Albrecht *et al.*, Phys. Rev. Lett. **34**, 1400 (1975).

## Bibliography

---

- [29] L. Corradi *et al.*, Phys. Rev. **C 56**, 938 (1997).
- [30] L. Corradi *et al.*, Phys. Rev. **C 54**, 201 (1996).
- [31] L. Corradi *et al.*, Phys. Rev. **C 61**, 024609 (2000).
- [32] R. Broda *et al.*, Phys. Rev. Lett. **68**, 1671 (1992).
- [33] R. Broda, Eur. Phys. J. **13**, 1 (2002).
- [34] J.F. Cocks *et al.*, Phys. Rev. Lett. **78**, 2920 (1997).
- [35] S.J. Asztalos *et al.*, Phys. Rev. **C 60**, 044307 (1999).
- [36] I.Y. Lee *et al.*, Phys. Rev. **C 56**, 753 (1997).
- [37] W. Królas *et al.*, Nucl. Phys. **A 724**, 289 (2003).
- [38] C. Chandler *et al.*, Phys. Rev. **C 61**, 044309 (2000).
- [39] J.M. Daugas *et al.*, Phys. Lett. **B 476**, 213 (2000).
- [40] R. Bock *et al.*, Nukleonika, **22**, 1 (1977).
- [41] M. Lefort and Ch. Ngô, Ann. Phys. **3**, 5 (1978).
- [42] A. Olmi *et al.*, Phys. Rev. Lett. **41**, 688 (1978).
- [43] C.K. Gelbke *et al.*, Phys. Lett. **B 43**, 284 (1973).
- [44] H. Takai *et al.*, Phys. Rev. **C 38**, 1247 (1988).
- [45] D.A. Bromley, *Treatise on Heavy-Ion Science*, Plenum Press, New York (1984).
- [46] R. Bass, *Nuclear Reactions with Heavy Ions*, Springer-Verlag, New York (1980).
- [47] K. Debertin and R.G. Helmer, *Gamma and X-ray Spectrometry with Semiconductors Detectors*, North-Holland, Amsterdam (1988).
- [48] web page: [www.crystalsland.com/bgo.html](http://www.crystalsland.com/bgo.html).

## Bibliography

---

- [49] J.F. Sharpey-Schafer and J. Simpson, *Prog. Part. Nucl. Phys.*, **21**, 293 (1988).
- [50] T. Mukoyama *et al.*, *Nucl. Instr. and Meth.* **A134**, 125 (1976).
- [51] R.N. Hall *et al.*, *IEEE Tr. Nucl. Sci.* **21**, 260 (1974).
- [52] R. Wichner *et al.*, *IEEE Tr. Nucl. Sci.* **21**, 273 (1974).
- [53] M. Koenen *et al.*, *IEEE Tr. Nucl. Sci.* **42**, 653 (1995).
- [54] D.Bazzacco *et al.*, *GASP proposal, Padova 1990., Proc. Workshop on Large Gamma-ray Detector Arrays*, Chalk River, Canada, AECL-10163, 376 (1992).
- [55] J. Simpson, *Z. Phys.* **A358**, 139 (1997).
- [56] M.A. Deleplanque, R.M. Diamond (Eds.), *Gammasphere Proposal*, Lawrence Berkeley National Laboratory Report 5202 (1988).
- [57] J. Simpson *et al.*, *Heavy Ion Physics* **11**, 159 (2000).
- [58] G.J. Schmid *et al.*, *Nucl. Instr. Meth.* **A417**, 95 (1998).
- [59] T. Glasmacher, *Annu. Rev. Nucl. Part. Sci.* **48**, 1 (1998).
- [60] K. Vetter *et al.*, *Nucl. Instr. and Meth.* **A 452**, 223 (2000).
- [61] M.A. Deleplanque *et al.*, *Nucl. Instr. and Meth.* **A 430**, 292 (1999).
- [62] J. Eberth *et al.*, *Progress in Particle and Nuclear Physics* **46**, 389 (2001).
- [63] J.J. Valiente-Dobón *et al.*, *Nucl. Instr. and Meth.* **A 505**, 174 (2002).
- [64] C. J. Pearson *et al.*, *IEEE Trans. on Nucl. Sci.*, Vol. 49, No. 3, 1209 (2002).
- [65] M.W. Simon *et al.*, *Nucl. Instr. Meth.* **A 452**, 205 (2000).
- [66] R.B. Firestone and V.S. Shirley (Eds), *Table of Isotopes 8th ed.*, John Wiley and Sons (1996).

## Bibliography

---

- [67] L.C. Carraz *et al.*, Nucl. Phys. **A 158**, 403 (1970).
- [68] W. Gelletly *et al.*, Phys. Rev. **181**, 1682 (1969).
- [69] M. Jääskeläinen *et al.*, Nucl. Instr. Meth. **204**, 385 (1983).
- [70] D.C. Radford, Nucl. Inst. Meth. Phys. Res., **A 361**, 297 (1995)
- [71] W. Urban, *ANA software*, private communication, University of Manchester.
- [72] C.T. Zhang, *et al.*, Nucl. Phys. **A 628**, 386 (1998).
- [73] A. Kerek *et al.*, Nucl. Phys. **A 198**, 466 (1972).
- [74] A. Kerek *et al.*, Nucl. Phys. **A 172**, 603 (1971).
- [75] L.C. Carraz *et al.*, Nucl. Phys. **A 171**, 209 (1971).
- [76] M. Kortelahti *et al.*, Nucl. Phys. **A 376**, 1 (1982).
- [77] M. Pfützner *et al.*, Phys. Rev. **C 65**, 064604 (2002).
- [78] S.W. Yates *et al.*, Nucl. Phys. **A 222**, 301 (1974).
- [79] Zs. Podolyák *et al.*, Progress of Theoretical Physics, **146**, 467 (2002).
- [80] J.C. Cunnane *et al.*, Phys. Rev. **C 13**, 2197 (1976).
- [81] V. Kölschbach *et al.*, Nucl. Phys. **A 439**, 189 (1985).
- [82] B. Fogelberg *et al.*, Phys. Rev. Lett. **73**, 2413 (1994).
- [83] B. Fogelberg *et al.*, Nucl. Phys. **A 352**, 157 (1981).
- [84] J. Genevey *et al.*, Phys. Rev. **C 63**, 054315 (2001).
- [85] G. Lo Bianco, P. Paruzzi, K.P. Schmittgen, R. Reinhardt, A. Gelberg, K.O. Zell, P. von Brentano, N. Blasi, Nucl. Phys. **A 470**, 266 (1987).
- [86] J. C. Merdinger *et al.*, Nucl. Phys. **A 346**, 281 (1980).

## Bibliography

---

- [87] M. Lach *et al.*, Z. Phys. **A 319**, 235 (1984).
- [88] H. A. Roth *et al.*, Eur. Phys. J. **A 10**, 275 (2001).
- [89] S. Harissopulus *et al.*, Phys. Rev. **C 52**, 1796 (1995).
- [90] P. Raghavan, At. Data Nucl. Data Tables **42**, 189 (1989).
- [91] P. Das *et al.*, Phys. Rev. **C 53**, 1009 (1996).
- [92] J.H. Hamilton *et al.*, Phys. Rep. **264**, 215 (1996).
- [93] J.H. Hamilton *et al.*, Prog. Part. Nucl. Phys. **38**, 273 (1997).
- [94] W. Urban *et al.*, Nucl. Phys. **A 613**, 104 (1997).
- [95] M. Ohshima *et al.*, Hyperfine Interactions **7**, 103 (1979).
- [96] P.J. Rothschild *et al.*, Phys. Rev. **C 34**, 732 (1986).
- [97] E. Dragulescu, G. Semenescu and I. Iftimia, Pramana J. Phys. **53**, 447 (1999).
- [98] S. Juutinen *et al.*, Phys. Lett. **B 386**, 80 (1996).
- [99] P. Schuler *et al.*, Z. Phys. **A 317**, 313 (1984).
- [100] H. Prade *et al.*, Nucl. Phys. **A 472**, 381 (1987).
- [101] M. Meyer-Lévy and V. Lopac, Phys. Rev. **C 8**, 829 (1973)
- [102] A. Bohr and B.R. Mottelson, *Nuclear Structure Vol. 1*, Benjamin, New York (1975).
- [103] T.R. Fisher and P.D. Bond, Part. Nucl. **6**, 119 (1973).
- [104] C. Bargholtz *et al.*, Z. Phys. **260**, 1 (1973).
- [105] S. Z. Gui *et al.*, Z. Phys. **A 305**, 297 (1982).
- [106] E. Nolte *et al.*, Z. Phys. **A 306**, 211 (1982).

## Bibliography

---

- [107] S. Lunardi *et al.*, Z. Phys. **A** **328**, 487 (1987).
- [108] C.T. Zhang *et al.*, Phys. Rev. **C** **62**, 057305 (2000).
- [109] A. Dewald *et al.*, Phys. Rev. **C** **54**, R2119 (1996).
- [110] P. Petkov *et al.*, Phys. Rev. **C** **62**, 014314 (2000).
- [111] O. Stuch *et al.*, Phys. Rev. **C** **61**, 044325 (2000).
- [112] E.S. Paul *et al.*, Phys. Rev. **C** **40**, 1255 (1989).
- [113] C. Bell *et al.*, Bull. Ann. Phys. **27**, 1, DF10 (1982).
- [114] P. Moller *et al.*, Atom. Data and Nucl. Data Tables **59**, 185 (1995).
- [115] J. Glatz, K.E.G. Löbner and F. Oppermann, Z. Phys. **227**, 83 (1969).
- [116] P. Kleinheinz, P.J. Daly and R.F. Casten, **A** **208**, 93 (1973).
- [117] K.E.G. Löbner in, *The Electromagnetic Interaction in Nuclear Spectroscopy*, W.D. Hamilton (ed.), North-Holland (1975) Chapter 5.
- [118] K.C. Yeung, Ph.D Thesis, University of Surrey (1993) unpublished.
- [119] C. Wheldon *et al.*, Nucl. Phys. **A** **699**, 415 (2002).
- [120] C.Y. Wu *et al.*, Nucl. Phys. **A** **533**, 359 (1991).
- [121] B. Fornal *et al.*, Act. Phys. Pol. **B** **26**, 357 (1995).
- [122] J.F.C. Cocks *et al.*, J. Phys. **G** **26**, 23 (2000).
- [123] T. Shizuma *et al.*, Nucl. Phys. **A** **593**, 247 (1995).
- [124] C. Wheldon, Ph.D Thesis, University of Surrey (1999) unpublished.
- [125] T. Shizuma *et al.*, Phys. Rev. **C** **65**, 064310 (2002).
- [126] T. Shizuma *et al.*, Phys. Lett. **B** **442**, 53 (1998).

## Bibliography

---

- [127] A. Bohr and B.R. Mottelson, *Nuclear Structure Vol. 2*, Benjamin, New York (1975).
- [128] P. Alexander *et al.*, Phys. Rev. **B 133**, 284 (1964).
- [129] K. Jain *et al.*, Nucl. Phys. **A 591**, 61 (1995).
- [130] R. Bengtsson *et al.*, At. Data and Nucl. Data Tables **35**, 15 (1986).
- [131] A.K. Jain *et al.*, Rev. Mod. Phys. **62**, 393 (1990).
- [132] F.G. Kondev, Ph.D Thesis, Australian National University (1997) unpublished.
- [133] C. Wheldon *et al.*, Phys. Lett. **B 425**, 239 (1998) and references therein.
- [134] C. Wheldon *et al.*, Phys. Rev. **C 59**, R2334 (1999) and Nucl. Phys. **A 652**, 103 (1999).
- [135] C.S. Purry *et al.*, Nucl. Phys. **A 632**, 229 (1998).
- [136] Zs. Podolyák *et al.*, Phys. Lett. **B 491**, 225 (2000).
- [137] H.H. Bolotin *et al.* Nuc. Phys. **A 370**, 146 (1981).
- [138] J.F.W.Jansen *et al.*, Nucl. Phys. **A 115**, 321 (1968).
- [139] M. Caamaño *et al.*, private communication.
- [140] H. Toki *et al.*, Nucl. Phys. **A 279**, 1 (1977).
- [141] C. Günther *et al.*, Phys. Rev. **C 15**, 1298 (1977).
- [142] W.R. Phillips *et al.*, Eur. Phys. J. **A 3**, 205 (1998).
- [143] W. Urban *et al.*, Phys. Rev. **C 61**, 041301(R) (2000).
- [144] P.D. Bond *et al.*, Phys. Lett. **B 130**, 167 (1983).

## Bibliography

---

- [145] C. Wheldon *et al.*, Phys. Rev. **C 63**, 011304(R) (2000).
- [146] P.H. Regan *et al.*, Phys. Rev. **C**, in press (2003).
- [147] C.Y. Wu *et al.*, Nucl. Phys. **A 607**, 178 (1996).
- [148] L. Palafox, Doctoral Thesis, University of Hidelberg, (1996).
- [149] David A. Bell *Solid State Pulse Circuits*, 3rd ed, *Englewood Cliffs NJ; Prentice-Hall inc* 1988.
- [150] A. Georgiev and W. Gast, IEEE Transactions on Nucl. Sci., **Vol 40**, 770 (1993).
- [151] A. Georgiev *et al.*, IEEE Transactions on Nucl. Sci., **Vol 41**, 1116 (1994).
- [152] J. van der Marel *et al.*, Nucl. Instr. and Meth., **A437**, 538 (1999).
- [153] W.R. Nelson, H. Hirayama and D.W.O. Rogers, SLAC report No. 265 (1985).
- [154] web page:<http://ehssun.lbl.gov/egs/egs.html>
- [155] E. Gatti *et al.*, Nucl. Instr. and Meth., **A458**, 738 (2001).
- [156] Th. Kröll *et al.*, INFN-Legnaro National Laboratory, Annual Report, (1998).
- [157] L. Mihailescu, Doctoral Thesis, Forschungszentrum Jülich, (2000).
- [158] AGATA, *Technical Proposal for an Advanced GAMMA Tracking Array for the European Gamma Spectroscopy Community*, September 2001.

# Appendix A

## Gamma-Ray Tracking

### A.1 $6 \times 6$ Segmented Germanium Detector

#### A.1.1 Prototype Description

A prototype, highly segmented, coaxial hyper-pure n type germanium detector has been constructed by EURISYS mesures (*EGC 60-90 SEG36*), see Fig. A.1, with the aim of testing the applicability of  $\gamma$ -ray tracking and ultimately improving the sensitivity of nuclear spectroscopic studies. The crystal has an external diameter of 60 mm and the length is 90 mm. The outer *p-type* ion-implanted contact of the crystal is segmented into 6 segments in both the longitudinal and radial direction, the disks are 15 mm long. The inner contact is *n<sup>+</sup>* lithium diffused. This inner contact is not segmented and can be used to provide a total energy signal for the full crystal. The impurities are not homogeneneously distributed,  $0.67 \cdot 10^{10} \text{ at/cm}^3$  at the top coaxial part and  $2.4 \cdot 10^{10} \text{ at/cm}^3$  at the closed end part. A schematic labelled view of the detector is shown in Fig. A.2. The cryostat has 3.0 litre capacity and it keeps the crystal at Liquid Ni temperature for 36 hours.

The outer contact is grounded, each segment goes to ground through a DC coupled preamplifier, while the inner contact is positive polarized at 3500 V. The energy signal is collected through an AC coupled preamplifier. The signals from the

## Appendix A. Gamma-Ray Tracking

---



Figure A.1: EURISYS measures (EGC 60-90 SEG36) prototype.

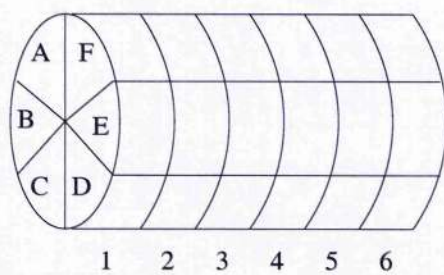


Figure A.2: Schematic view of the segmented germanium crystal. The letters label the different disk sections and the numbers label the longitudinal sections.

## Appendix A. Gamma-Ray Tracking

---

warm FETs are connected to 36 charge sensitive preamplifiers. The preamplifiers are based on University Cologne design [148]. They are placed in an aluminium housing which can be seen at the bottom of the dewar in Fig. A.1. The rise time performance is 29 ns. If the risetime is limited by the bandwidth of the circuit, they both are related [149],

$$Risetime = \frac{2.2}{2\pi Bandwidth} \quad (A.1)$$

thus the *Bandwidth* = 12 MHz for 29 ns risetime.

The signal from the preamplifiers goes into a *cM62* module where 3 *AD40* (Very-High-Speed Data Acquisition Module) are attached to it. The *AD40* module has two channels for signal digitisation. These modules have been provided by *OMNIBUS*. Each of the *cM62* modules, with only one *DSP* (Digital Signal Processor), comprises six channels for pulse signal digitalisation. The boards are controlled by a host computer. In the schematic block diagram A.3 two channels are shown. After passing through a *Low Distortion Input Amplifier*, the signal is digitised by a 12 bit, 40 MHz ADC and the digitised signal is sent to a *FIFO* (First In First Out), circular buffer. The signal from the inner contact is used as external trigger. A second computer allows on-line analysis using *MIDAS*, the data can be sent to a tape server.

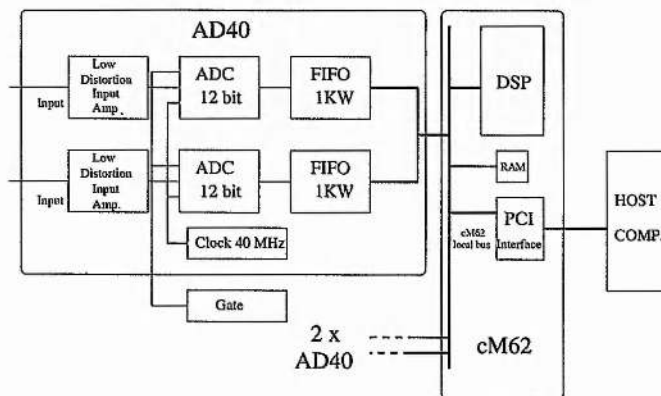


Figure A.3: Diagram of the electronics used for pulse processing, module *cM62* and *AD40*

### A.1.2 Measurement of Resolution and Risetimes

The energy resolution is an important characteristic of a germanium detector which gives a guide of the overall performance of the detector. In Fig. A.4 the energy resolution for two different energies (1332 keV from  $^{60}\text{Co}$  and 122 keV from  $^{57}\text{Co}$ ) are shown. The comparison of these two quantities will reflect the properties of the detector in terms of both the charge collection and noise contributions to the signal. All energy resolution measurements were performed with a shaping time amplifier ( $6 \mu\text{s}$ ). The energy resolution values obtained in our measurements met the manufacturer's energy resolutions.

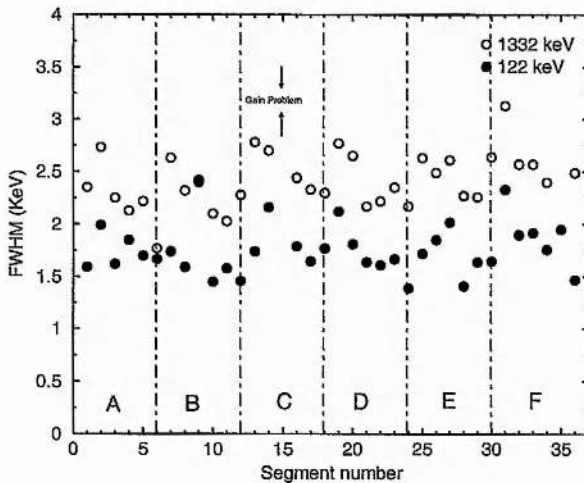


Figure A.4: Energy resolution for all the segments in the EURISYS  $6\times 6$  prototype. The full black points show the FWHM at 122 keV, the open points show the FWHM at 1332 keV. Note, the data points for segment C3 are missing due to problems with the preamplifier.

The energy resolution of the inner contact for 122 keV and 1332 keV were measured to be 3.60 keV and 4.10 keV respectively, which does not meet the manufacturer's measurements, which guarantees 3 keV resolution. It was found that the cross-talk between the inner contact and the segments was responsible of this poor resolution (although no cross-talk was found between segments). However, as the

## Appendix A. Gamma-Ray Tracking

---

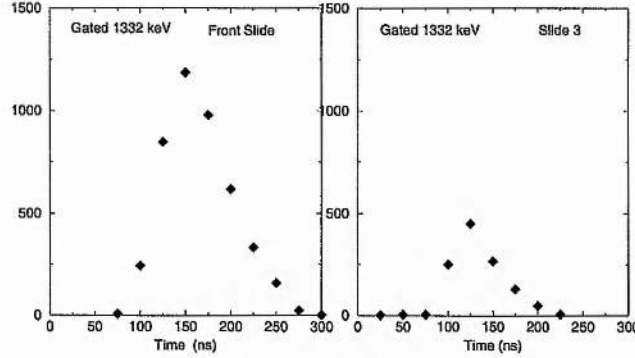


Figure A.5: Risetime distributions for the front slide (slide 1) and the slide 3, for 1332 keV  $\gamma$ -rays.

results in Fig. A.4 show, the resolution of the front segments is worse than the resolution of the coaxial segments [60]. The smaller size of the segment gives smaller capacitance with the aluminium can, decreasing the noise contribution.

Other test measurements were made, including, as shown in the Fig. A.5, a distribution of the rise time (T10%-T90%) for  $\gamma$ -ray energies of 1332 keV for two different slices. Inspection of these two plots show a normal distribution of risetimes.

Comparing both plots taken under the same conditions, one observes that the rise time distribution from the front slice is broader and the peak value ( $\sim 150$  ns) is higher than in slice 3 ( $\sim 125$  ns). This was expected and can be explained by recalling that the front edge is not coaxial, however the slide 3 is coaxial. The electric field is only well defined in the coaxial part of the detector. This is due to the geometry of the crystal, which is closed-ended coaxial. There are areas at the edges of the crystal where the electric field is not as strong as in the coaxial part and the charge collection takes longer.

### A.1.3 Net Charge and Mirror Charge Signals

The segmentation of a germanium crystal leads to a tracking detector. In the case of a segmented germanium detector not only the analysis of the pulse from the segment that is hit is feasible, but also the analysis of the induced signals from the

## Appendix A. Gamma-Ray Tracking

---

neighbouring segments. The resolution given by the segmentation of the crystal can be easily improved by analysing the net and mirror signals. A resolution up to a few mm can be obtained [60]. The radial position of the main interaction is determined by the pulse from the segment which is hit. The fall time of the pulse is given by the collection time of the electrons and holes, this is the time which gives the radial position. The rise time of the signal is given by the preamplifier.

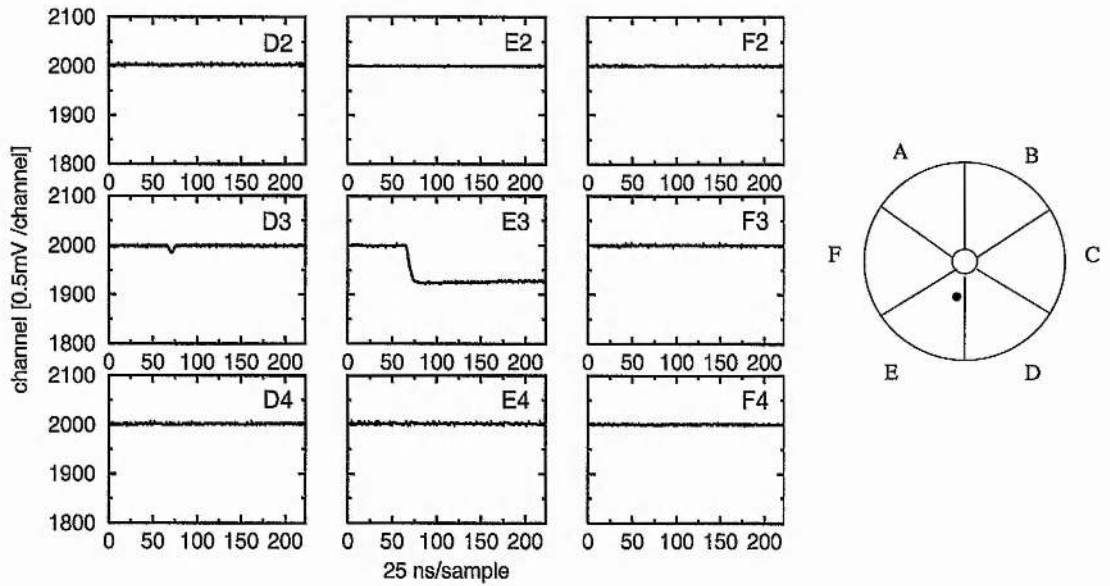


Figure A.6: Digitised signals for an event in segment E3 and a negative mirror charge in segment D3.

The azimuthal position is determined from the mirror charges induced in the neighbouring segments. The mirror charges are induced in the neighbouring contacts when the electrons and holes drift in the hit segment. The pulses from the hit segment and neighbouring segment are quite different and therefore easily distinguishable. In the neighbouring segment no net charge is collected. The mirror signal has a maximum while electrons and holes are moving in the segment where the interaction occurs, and it returns to zero when the net charges have been collected. The polarity of the mirror charges can be either positive or negative. It is negative if the main interaction occurs close to the inner contact, the pulse is mainly

## Appendix A. Gamma-Ray Tracking

---

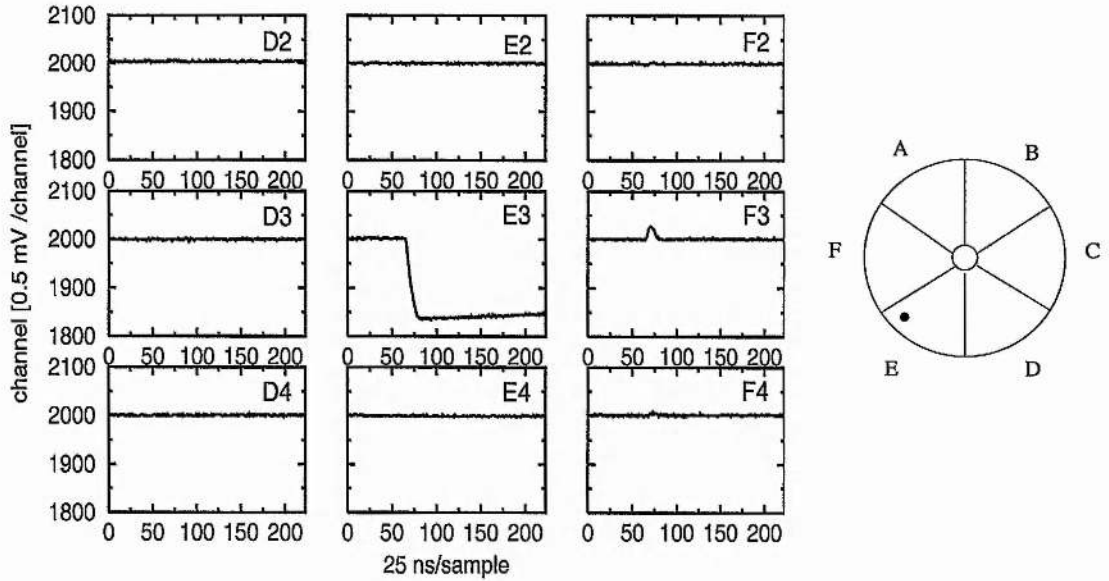


Figure A.7: Digitised signals for an event in segment E3 and a positive mirror charge in segment F3.

induced by drifting holes. It is positive if the interaction happens close to the outer contact, where the signal is mainly induced by drifting electrons. The amplitude of the mirror charges depends on the distance to the neighbouring segment of the main interaction and the radial position of this one.

Figures A.6 and A.7 show digitised signals from the  $6 \times 6$  Eurysis prototype with a non collimated  $^{60}\text{Co}$  source at a distance of 25 cm from the face of the detector. Each signal has 256 samples (one sample every 25 ns) covering around 5  $\mu\text{s}$  in total. Approximately 1.25  $\mu\text{s}$  of this time period is before the trigger point. Figure A.6 shows a net charge in E3, where a  $\gamma$ -ray interaction deposited approximately 200 keV and a negative mirror charge in D3, *i.e.* the main interaction occurred in segment E3 close to the inner contact nearby D3. However, Fig. A.7 shows a net charge in E3, where a  $\gamma$ -ray interaction deposited approximately 430 keV and a positive mirror charge in F3, *i.e.* the main interaction occurred in segment E3 close to the outer contact nearby F3.

### A.1.4 Energy Deposited in an Interaction: Moving Window Deconvolution Method (MWD)

The interaction energy provides vital information for tracking purposes. The digitised signals, using the previously described Data Acquisition system (40 MHz, 12 bit), were processed using the Moving Window Deconvolution method (MWD) [150, 151] to obtain the deposited energy with high resolution. The first step in the method is to reconstruct the original charge distribution originated by the radiation event. This reconstruction involves a simple and fast deconvolution as the main process.

The basic elements of the semiconductor system are a detector followed by a charge sensitive preamplifier. Any radiation event produces an amount of charge proportional to the absorbed energy. That charge results in a steplike waveform at the preamplifier output. The preamplifier output signal  $U_P(t)$  is described by a convolution between the charge distribution function  $g(t)$  and the preamplifier impulse response  $f(t)$

$$U_P(it_s) = \sum_{j=0}^{\infty} g(jt_s)f(it_s - jt_s) \quad (\text{A.2})$$

where  $t_s$  is the sampling interval,  $U_P(it_s)$  is the digital discrete-time representation of the function seen by the ADC, which includes the response of the preamplifier  $f(it_s)$  and the charge distribution  $g(jt_s)$ . Normalizing the time scale to  $t_s$  and considering that the output depends only on the present and past amount of charge deposited on the detector then (A.2) becomes,

$$U_P(i) = \sum_{j=z}^i g(j)f(i-j) \quad \text{for } i > z \quad (\text{A.3})$$

where  $i$  is the current instant which corresponds to the current sample  $U_P(i)$  and  $z$  is an arbitrary time reference.

A further reduction of the number of equations in Equation A.3 can be done if it is realised that the charge function is right-side limited, *i.e.* the charge distribution

## Appendix A. Gamma-Ray Tracking

---

under normal conditions is limited. For germanium detectors the charge distribution is not more than  $1 \mu\text{s}$ . Assuming that there are no charges associated with the single event outside of the observational interval, or window, with the normalized length of  $M$ , then the number of equations in A.3 can be reduced to  $M$ . Assuming that the impulse response of the analog part is known, the sets of Equations A.3 can be solved for the charge matrix  $g_{(z,z+M)}$ , which has  $M$  elements associated with the window  $(z, z + M)$  or equivalently  $(n - M, n)$ . After summing all the elements of the matrix, the total charge in the window is obtained,

$$G(n) = \sum_{i=z}^{z+M} g(i) = \sum_{i=n-M}^n g(i) \quad (\text{A.4})$$

$z$  is an arbitrary time reference. If we increase  $z$  by one after each solving the Equations A.3 and A.4, a continuous sequence of  $G(n)$  results can be obtained for each one, representing the total charge released in the window, where each window is shifted against the previous one by one sampling interval.

A preamplifier with a clean exponential decay is considered. Thus  $f(n) = k^n$ , where  $k = e^{-\alpha}$  and  $\alpha$  is the decay constant of the exponent. Applying  $f(n)$  to Equations A.3 and A.4 a recursive equation for the first window can be obtained,

$$G(i) = \sum_{j=z}^i g(j) = U(i) + (1 - k) \sum_{j=z}^{i-1} U(j) \\ \text{for } i \cap (z, z + M) \quad (\text{A.5})$$

where  $i$  reaches the right limit of the window, the total charge  $G(n = z + M)$  in the window  $(z, z + M)$  is extracted. Thus for any further window shifted by one sampling interval with respect to the previous one the total charge is given by,

$$G(n) = \sum_{j=n-M}^n g(j) = U(n) - U(n - M) + (1 - k) \sum_{j=n-M}^{n-1} U(j) \\ \text{for any } n > z + M \quad (\text{A.6})$$

Figure A.8 shows the results of two deconvoluted signals based on Equations A.5 and A.6. The pulse signal from the hit segment D3 gives a well-like deconvoluted

## Appendix A. Gamma-Ray Tracking

---

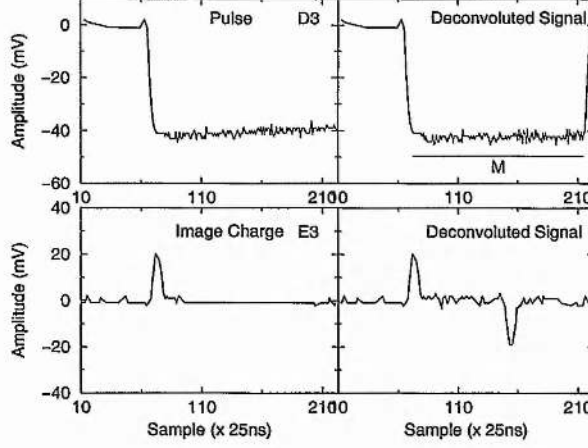


Figure A.8: Pulse signal from segment D3 with energy deposition by a  $\gamma$ -ray and the neighbouring image charge, segment E3. The deconvoluted calculated signals according to Equations (A.5) and (A.6) are shown on the right-hand side.

signal, with a flat bottom and width  $M$ . The average of those points gives the energy deposited at the interaction. The image charge from the neighbouring segment E3, gives a positive peak followed by a negative peak. However, the energy deposited information is given by the points between those peaks and the average of them is zero. Thus no charge has been deposited.

### A.1.5 MWD Results

The Moving Window Deconvolution method (MWD) [150, 151] has been used to obtain the energy spectra for  $^{60}\text{Co}$  and  $^{152}\text{Eu}$  sources. The method has been found to be very stable and fast. Good performance has been obtained for both sources at a distance of 25 cm from the front edge. The results are shown in Fig. A.9. A FWHM at 1.332 MeV of 3.5 keV was found for segment B1 (front edge), compared to the resolution obtained with a traditional analogue setup of 2.7 keV. The energy resolution for the same segment at 122 keV is 3.1 keV compared to 1.7 keV obtained with the traditional setup.

Other attempts have been done to calculate the energy deposited. An expo-

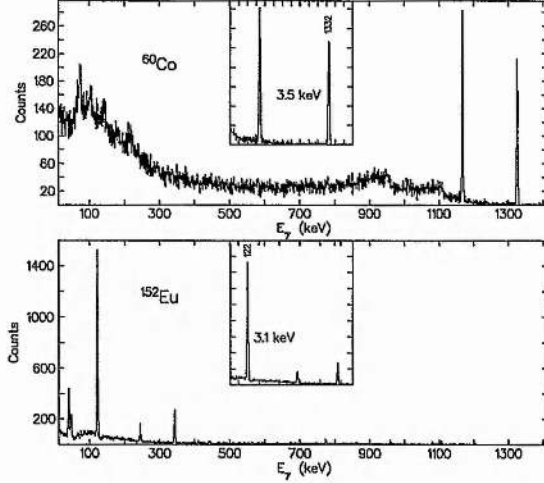


Figure A.9: Performance of the Moving Window Deconvolution MWD method for  $^{60}\text{Co}$  and  $^{152}\text{Eu}$  sources for segment B1 (front edge).

nential fitting of the signal has been performed, the results of which are shown in Fig. A.10. In this case, the energy resolution is poorer (4 keV at 1.3 MeV and 4.5 keV at 122 keV) than the MWD method. Furthermore this algorithm is slower than the MWD method, and thus difficult to incorporate for on-line signal processing.

## A.2 Reconstructing the $\gamma$ -Ray Path

### A.2.1 Introduction

When a  $\gamma$  ray interacts in a germanium detector, several energy depositions can occur before either the  $\gamma$  ray is totally absorbed or it is scattered out of the detector. In the case when more than one  $\gamma$  ray interacts in the detector simultaneously, the different  $\gamma$  rays have to be distinguished. This requires the reconstruction of the initial energy of the different  $\gamma$  rays, when in turn requires a well defined first interaction position for each photon. To achieve this, the use of a tracking algorithm is essential. The photoelectric and Compton probabilities and the Compton scattering formula are used. After the reconstruction of the track, the first interaction points will be used to deduce angular correlations, reduce doppler shift and perform where

## Appendix A. Gamma-Ray Tracking

---

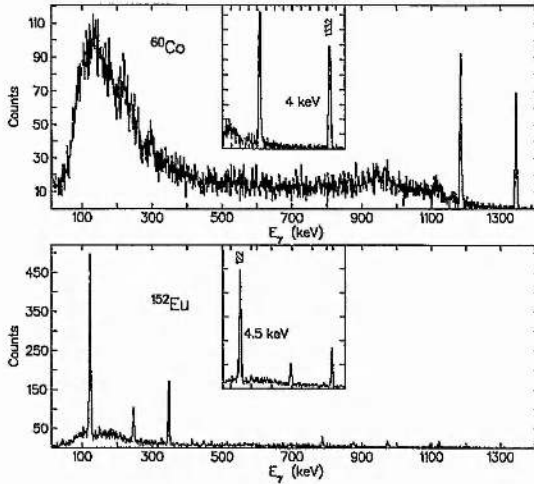


Figure A.10: Performance of an exponential fitting of the digitised signal for  $^{60}\text{Co}$  and  $^{152}\text{Eu}$  sources for segment B1 (front edge).

necessary Compton suppression. In the current work, the first approach has been to track a single  $\gamma$  ray in a germanium detector. The possibility of having more than one  $\gamma$  ray has been taken into account using the backtracking concept [152].

### A.2.2 Simulation of the Prototype

Monte Carlo simulations using EGS4 (Electron Gamma Shower) [153, 154] have been performed assuming a  $^{60}\text{Co}$  source at a distance of 25 cm from the front edge of the detector. The results obtained using the simulation combined with the tracking algorithm are then compared with real source data from a  $^{60}\text{Co}$  source. Figure A.11 shows simulated energy spectra for a  $^{60}\text{Co}$  source. It has been highlighted that only 1/3 of the  $\gamma$  rays which interact in the detector are ultimately photoelectrically absorbed, thus giving the total energy of the initial  $\gamma$  ray. For photons with energies above 150 keV, Compton scattering dominates. It is only when the  $\gamma$  ray has lost almost all of its energy when the photoelectric absorption cross-section becomes larger and the remaining  $\gamma$ -ray energy will be photoelectrically absorbed. The other 2/3 corresponds to  $\gamma$  rays that were not photoelectrically absorbed and scattered out of the detector. The simulated photopeak efficiency is found to be  $\sim 23\%$ .

## Appendix A. Gamma-Ray Tracking

---

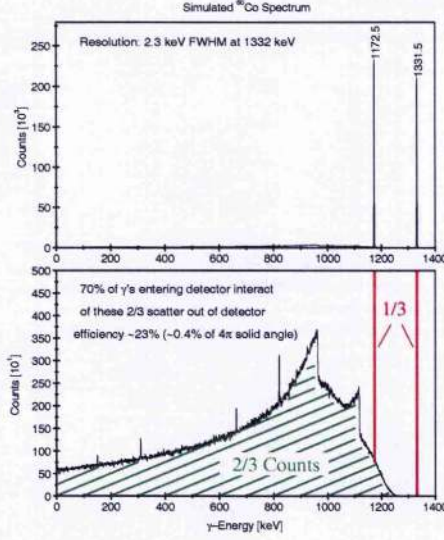


**Figure A.11:** Simulated spectra for a  $^{60}\text{Co}$  source (upper panel), detail of the Compton background (lower panel).

### A.2.3 Tracking Algorithm

The tracking algorithm attempts to *follow* the path of the  $\gamma$  ray from its emission point, 25 cm in distance from the front edge of the detector. To achieve the reconstruction of the  $\gamma$  ray track, the energy deposited in each interaction and the position of each Compton and photoelectric interaction must be determined. As shown previously, the energy deposited in each segment can be easily recovered using the MWD algorithm. However, for the moment, it is not possible to distinguish whether the energy deposited in the segment was due to only one or more interactions<sup>a</sup>.

Nevertheless, the probability of having more than one interaction in the same segment is not likely, as shown in Fig. A.12. For low energies the probability of having more than one interaction is unlikely due to the fact that the cross section is dominated by photoelectric absorption (e.g. for 100 keV photons, the probability is  $\sim 15\%$ ). When the energy of the incident  $\gamma$  ray increases, it becomes more likely to have more than one interaction and the Compton cross section starts dominating

---

<sup>a</sup>Simultaneous pulse localization in the same segment is treated in [155]

## Appendix A. Gamma-Ray Tracking

---

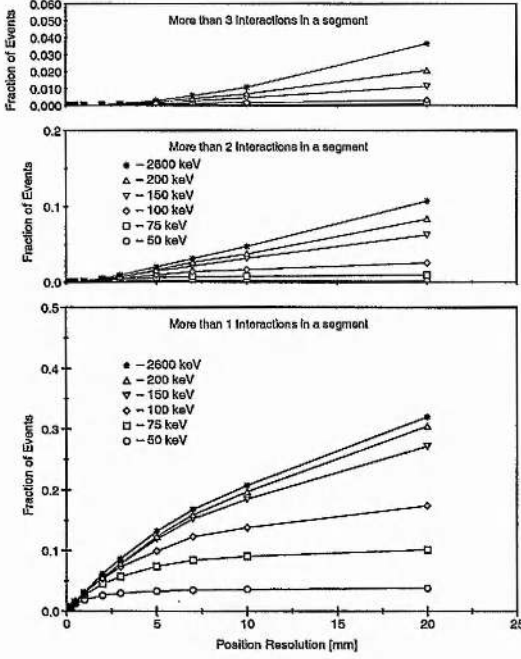


Figure A.12: For different position resolutions are shown the fraction of events which are not distinguishable, for more than one interaction in a segment (lower panel), more than two interactions (middle panel) or more than three interactions (upper panel). The 20 mm position resolution corresponds to the whole segment. Data obtained using EGS4 Monte Carlo simulations.

(e.g. for 2.6 MeV photons, the probability is  $\sim 30\%$ ).

The position information which can be obtained following a pulse shape analysis has an intrinsic constraint, which is the distance travelled by the electrons produced in the interaction. For typical nuclear energies, this distance is less than 1 mm as can be seen in Fig. A.13.

Each interaction point has certain associated uncertainty. This uncertainty depends on how good the pulse shape analysis method is in determining the interaction position<sup>b</sup>. It has been pointed out by other authors [158], using simulations, that

<sup>b</sup>Different algorithms have been developed to get the interaction position, based on methods of artificial intelligence, genetic algorithms (GA), artificial neural networks (ANN) [156] and Discrete Wavelet Transform (DWT) [157].

## Appendix A. Gamma-Ray Tracking

---

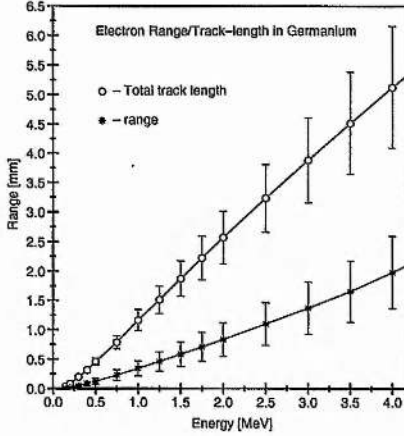


Figure A.13: Range and total track length of the electrons produced in the interaction of a  $\gamma$  ray in germanium. Data obtained using EGS4 Monte Carlo simulations.

a better spatial resolution of 5 mm has to be achieved in arrays like *AGATA* to improve the  $\varepsilon$  and  $P/T$  over current arrays. In this discussion it is assumed that only one  $\gamma$  ray interacts in the detector. Each individual interaction  $i$  has an associated energy deposited  $E_i$ , position  $(\rho_i, \Phi_i, z_i)$  and uncertainty  $\Delta r_i$ , which defines a sphere around the point of interaction. The source has a smaller uncertainty since its position is known accurately. It is assumed that the total energy  $E_{TOT}$  of the incident  $\gamma$ -ray is

$$E_{TOT} = \sum_{i=0}^N E_i \quad (\text{A.7})$$

where  $N$  is the total number of interactions.

The reconstruction of the track starts by choosing two initial points of interaction;  $(\rho_1, \Phi_1, z_1)$  with an uncertainty  $\Delta r_1$  and  $(\rho_2, \Phi_2, z_2)$  with an associated uncertainty  $\Delta r_2$ . The source position also provides information which is used by the algorithm. The two initial selected points are not decisive in the reconstruction of the track because all the points will be permuted and all possible tracks are checked. The algorithm calculates numerically the smallest ( $\Theta_i^{min}$ ) and the largest ( $\Theta_i^{max}$ ) possible angles for the first interaction, as shown in Fig. A.14.

The angles calculated are directly related by the Compton scattering formula,

## Appendix A. Gamma-Ray Tracking

---

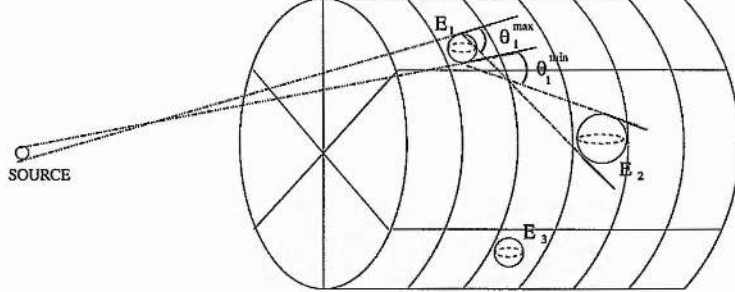


Figure A.14: Schematic representation of  $\Theta_i^{\min}$  and  $\Theta_i^{\max}$ , calculated numerically by the tracking algorithm for the first point of the  $\gamma$ -ray interaction. The different interaction points have an uncertainty that has been represented by spheres. The source is indicated outside of the detector.

with the possible energy deposited in each interaction. The minimum angle  $\Theta_i^{\min}$  gives the minimum energy ( $E_i^{\min}$ ) deposition that can take place meanwhile  $\Theta_i^{\max}$  yields the maximum energy ( $E_i^{\max}$ ) that can be deposited in the interaction  $i$ .

$$\begin{aligned} E_i^{\max} &= E_{TOT} - \frac{E_{TOT}}{1 + \frac{E_{TOT}}{m_0 c^2} (1 - \cos \Theta_i^{\max})} \\ E_i^{\min} &= E_{TOT} - \frac{E_{TOT}}{1 + \frac{E_{TOT}}{m_0 c^2} (1 - \cos \Theta_i^{\min})} \end{aligned} \quad (\text{A.8})$$

where  $m_0$  is the rest mass of an electron and  $c$  is the velocity of light ( $m_0 c^2 = 511$  keV).

The two energy limits are calculated, using Equation A.8, for the interaction  $i$ . The energy deposited is checked to see whether it fits in the range of energies given by  $E_i^{\max}$  and  $E_i^{\min}$ . In the case that it does, the next closest point will be chosen and the process is repeated. If this was not the energy deposition sequence followed by the  $\gamma$  ray, then the energy deposited would not fit within the energy limits and the point  $i$  is discarded, a new point is chosen and the process described above repeated. This process continues until no interaction point is left. A new starting point is chosen and the whole process is repeated. Eventually all the positions are calculated, *i.e.*  $N!$  possible tracks can be calculated for the  $N$  individual  $\gamma$ -ray interactions within the germanium crystal.

## Appendix A. Gamma-Ray Tracking

As a result of the tracking algorithm, it could happen that no track is found that follows the experimentally measured points. The interpretation in such a case is that the  $\gamma$  ray scattered out of the detector, since no track is consistent due to the incorrect incident energy ( $E_{TOT}$ ) being used. The event is discarded, effectively providing Compton suppression. Therefore, in general, a unique track should be possible after the complete permutation of the  $N$  interaction points, assuming the  $\gamma$  ray did not scatter out of the detector. However, in reality the uncertainties in position and energy play an important role and more than one track could be possible within the limits.

Although more than one track could be possible, the *free path* concept, see Equation 2.40, allows one to work out which of all the possible tracks is the most likely. The probability of interaction of a  $\gamma$  ray with energy  $E$  after a distance  $x$  is given by,

$$P(x) = 1/\lambda(E)e^{(-\lambda(E)/x)} = \mu(E)e^{(-1/\mu(E)x)} \quad (\text{A.9})$$

where  $\lambda$  is the *mean free path*. In order to calculate  $\lambda(E)$ , the photoabsorption, Compton and pair production cross-sections have to be known for all the energies in the track.

All the distances between the different points and the probabilities are calculated using Equation A.9. The total probability for the different possible tracks are obtained from Equation A.10 and the most probable one is chosen as the reconstructed  $\gamma$ -ray path.

$$P(x) = \prod_{i=1}^N P_i \quad (\text{A.10})$$

To calculate which of the possible tracks is most probable, the *Klein-Nishina formula* can be used, see Equation 2.35. However, for low energy ( $< 500$  keV) photons, the angular distribution of scattered photons is not sufficiently anisotropic (see the plot in Fig. 2.4) to be used to discriminate between the different tracks.

### A.2.4 Tracking Algorithm Results

#### Results from Simulated Data

The tracking algorithm was tested on Monte Carlo simulated  $^{60}\text{Co}$  source data. It was assumed that electronic pulse shape analysis will be capable of increasing the segmentation to 1620 segments, with an average size of 5 mm radius spheres. The segment size of the detector corresponds to the position resolution for  $\gamma$ -ray interactions.

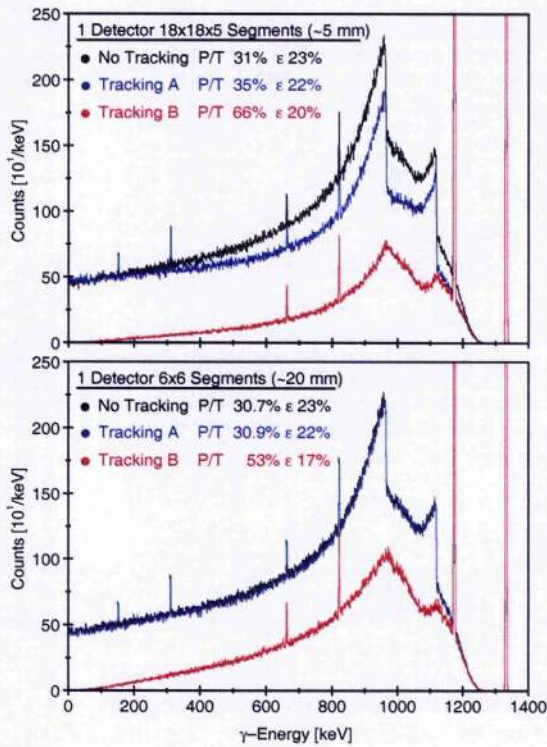


**Figure A.15:** Compton suppression performance of the tracking algorithm for a simulated  $^{60}\text{Co}$  source, for a position resolution of 5 mm (upper panel) and for a position resolution of 20 mm (lower panel).

Around 80% of the first interaction points of the tracks could be correctly identified, enabling an almost perfect Doppler correction. Around 50% of the tracks had all interactions correctly ordered. The performance of the algorithm for Compton

## Appendix A. Gamma-Ray Tracking

---

suppression and Doppler shift correction (identification of the position of the first interaction) was determined. It was found that, see Fig. A.15, the Peak-to-Total ratio, for 5 mm position resolution, improves from 31% to 66%, with only a 3% reduction in detection efficiency if the single interaction events are rejected (*Tracking B*). However, the  $P/T$  decreases to 35% if those events are not rejected (*Tracking A*). The performance of the algorithm for Compton suppression with a position resolution of 20 mm (corresponding to the physical dimension of an individual segment) is not as impressive. Nevertheless the Peak-to-Total ratio can improve from 31% up to 53%, with a 6% reduction in detection efficiency if the single interaction events are not considered.

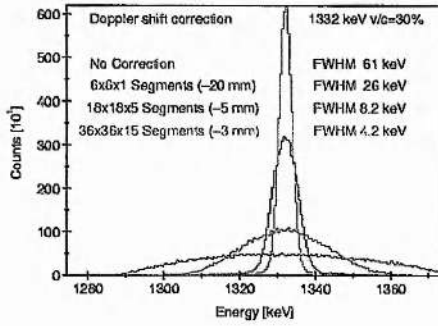


Figure A.16: Doppler correction performance of the tracking algorithm for a simulated  $^{60}\text{Co}$  source.

The effect of tracking on the Doppler correction has been determined for simulated events. For sources with a simulated velocity of  $v/c \sim 30\%$ , it was found (see Fig. A.16) that for  $\gamma$ -ray energies of 1.3 MeV, a FWHM of 8.2 keV can be obtained for 5 mm position resolution, compared to  $\sim 30$  keV corrected using a fixed correction point at the centre of the detector. The intrinsic energy resolution can be obtained, if a position resolution of 3 mm is achievable. A summary of the results obtained from the simulation can be seen in Table A.1.

Figure A.17 shows a plot of the efficiency and Peak-to-Total for different  $\gamma$ -ray energies for the  $6 \times 6$  segmented germanium detector. As before, this plot assumes only one  $\gamma$  ray per event. The efficiency reduces when the single interaction events

## Appendix A. Gamma-Ray Tracking

---

Table A.1: Summary of the results from simulated data for 5mm and 20mm resolution.

Simulated data (5 mm resolution)			
	No Tracking	Tracking A	Tracking B
$\varepsilon[\%]$	23	22	20
$P/T[\%]$	31	35	66
Doppler Correction [keV]	61	8.2	-
Simulated data (20 mm resolution)			
	No Tracking	Tracking A	Tracking B
$\varepsilon[\%]$	23	22	17
$P/T[\%]$	30.7	30.9	53
Doppler Correction [keV]	61	26	-

are rejected. This is especially true for low energy  $\gamma$  rays where photo-absorption is the main process. The Peak-to-Total improves significantly for energies above 600 keV. It improves drastically when single interaction events are rejected.

### Results from Experimental source Data

The tracking algorithm has been tested experimentally with source data. A  $^{60}\text{Co}$  source was placed at a distance of 25 cm from the front edge of the Eurysis  $6 \times 6$  detector. The energy deposited in each segment was extracted using the MWD method. The position resolution assumed was given by the segment (20 mm), and no pulse shape analysis was performed. The performance of the algorithm for Compton suppression was determined. The results obtained from  $^{60}\text{Co}$  source data (see Fig. A.18) are easily comparable with the results obtained from the simulated data, see Fig. A.15. The Peak-to-Total parameter drops from the value obtained for the simulated data from 30.7% to 6.2% obtained from the real data. This dramatic reduction can be explained by the fact that in the simulation background radiation is not taken into account.

## Appendix A. Gamma-Ray Tracking

---

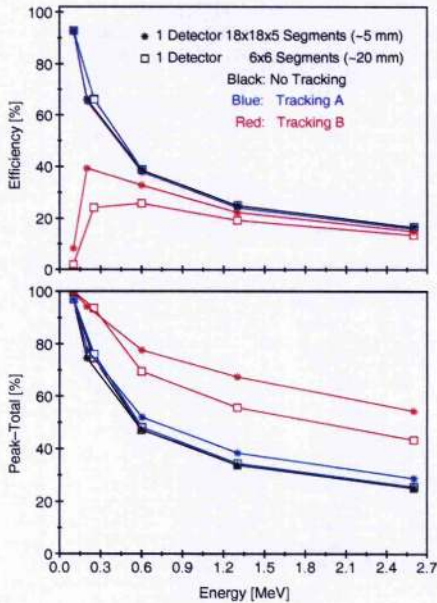


**Figure A.17:** Photopeak efficiency and Peak-to-Total for different energies as a result of tracking.

Nevertheless the improvement of the  $P/T$  after implementing the tracking algorithm is the main interest here. For *Tracking A* the Peak-to-Total hardly improves when the single interaction events are not rejected, but in both cases improves for *Tracking B* by approximately 70% if the single interaction events are rejected. The efficiency in both the source data or the simulated data drops by approximately 30% when single events are rejected, otherwise it remains the same. If pulse shape analysis is not feasible and a position better than 20 mm (segment) can not be achieved, the tracking algorithm method does not give any improvement for Compton suppression. Thus the spatial resolution has to be improved. A summary of the results obtained from the experimental source data can be seen in Table A.2.

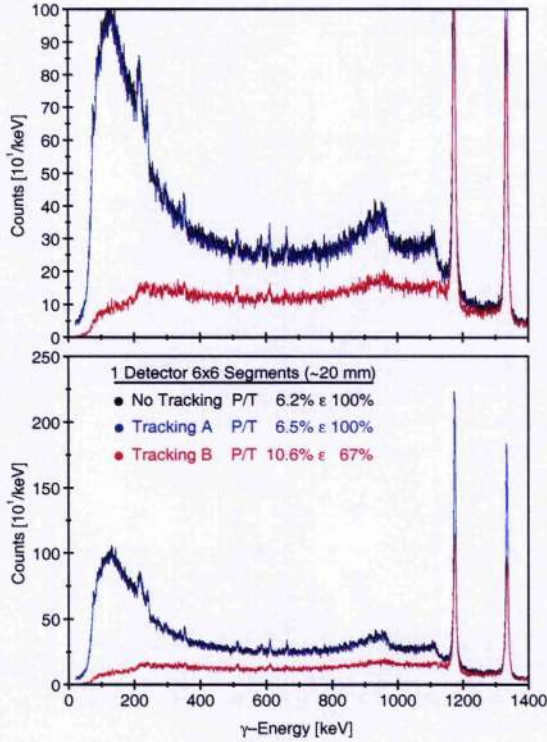


**Figure A.18:** Experimental Compton suppression performance of the tracking algorithm for source data, using a  $^{60}\text{Co}$  source at a distance of 25 cm to the front edge.

**Table A.2:** Summary of the results from experimental source data for 20mm resolution. Doppler correction is missing, since non in beam experiment has been performed.

Experimental Source data (20 mm resolution)			
	No Tracking	Tracking A	Tracking B
$\epsilon$ [%]	100	100	67
P/T[%]	6.2	6.5	10.6

## Appendix B

### Publications

1. "Study of  $^{136}\text{Ba}$  via deep inelastic collisions: identification of the  $(\nu h_{\frac{11}{2}})_{10+}^{-2}$  isomer"  
**J.J. Valiente-Dobón**, P.H. Regan, C. Wheldon, C.Y. Wu, N. Yoshinaga, K. Higashiyama, J.F. Smith, D. Cline, R.S. Chakrawarthy, R. Chapman, M. Cromaz, P. Fallon, S.J. Freeman, A. Görgen, W. Gelletly, A. Hayes, S.D. Langdown, I.Y. Lee, X. Liang, A.O. Macchiavelli, C.J. Pearson, Zs. Podolyák, R. Teng, D. Ward, D.D. Warner and A.D. Yamamoto, submitted to *Phy. Rev. C* (2003).
2. "Multi-quasiparticle states in  $^{184}\text{W}$  via multi-nucleon transfer"  
C. Wheldon, **J.J. Valiente-Dobón**, P.H. Regan, C.J. Pearson, C-Y. Wu, J.F. Smith, D. Cline, R.S. Chakrawarthy, R. Chapman, M. Cromaz, P. Fallon, S.J. Freeman, A. Görgen, W. Gelletly, A. Hayes, S.D. Langdown, I-Y. Lee, X. Liang, A.O. Macchiavelli, Zs. Podolyák, R. Teng, D. Ward, D.D. Warner and A.D. Yamamoto, submitted to *Eur. Phy. J. A* (2003).
3. "Binary-Reaction Spectroscopy of  $^{99,100}\text{Mo}$ : Intruder Alignment Systematics in  $N=57$  and  $N=58$  Isotones"  
P.H. Regan, A.D. Yamamoto, F.R. Xu, C-Y. Wu, A.O. Macchiavelli, D. Cline, J.F. Smith, S.J. Freeman, **J.J. Valiente-Dobón**, K. Andgren, R.S.

## Appendix B. Publications

- Chakrawarthy, M. Cromaz, P. Fallon, W. Gelletly, A. Görgen, A. Hayes, H. Hua, S.D. Langdown, I-Y. Lee, C.J. Pearson, Zs. Podolyák, R. Teng and C. Wheldon, in press, *Phy. Rev. C* (2003).
4. "Angular momentum population in the projectile fragmentation of  $^{238}\text{U}$  at 750 MeV/nucleon"  
K.A. Gladnishki, Zs. Podolyák, P.H. Regan, J. Gerl, M. Hellström, Y. Kopatch, S. Mandal, M. Górska, R.D. Page, H.J. Wollersheim, A. Banu, G. Benzoni, H. Boardman, M. La Commara, J. Ekman, C. Fahlander, H. Geissel, H. Grawe, E. Kaza, A. Korgul, M. Matos, M.N. Mineva, C.J. Pearson, C. Plettner, D. Rudolph, Ch. Scheidenberger, K-H. Schmidt, V. Shishkin, D. Sohler, K. Sümmerer, **J.J. Valiente-Dobón**, P.M. Walker, H. Weick, M. Winkler and O. Yordanov, to be submitted to *Phy. Rev. C* (2003).
5. "Production of Exotic Nuclear Isomers in Multi-Nucleon Transfer Reactions"  
P.H. Regan, **J.J. Valiente-Dobón**, C. Wheldon, C.Y. Wu, J.F. Smith, A.O. Macchiavelli, D. Cline, R.S. Chakrawarthy, R. Chapman, M. Cromaz, P. Fallon, S.J. Freeman, A. Görgen, W. Gelletly, A. Hayes, S.D. Langdown, I.Y. Lee, X. Liang, C.J. Pearson, Zs. Podolyák, R.Teng, D. Ward, D.D. Warner and A.D. Yamamoto, to be published in *Laser Phys.* (2003).
6. "Studies Around  $A \approx 100$  Using Binary Reactions"  
P.H. Regan, A.D. Yamamoto, C.Y. Wu, A.O. Macchiavelli, D. Cline, J.F. Smith, S.J. Freeman, **J.J. Valiente-Dobón**, R.S. Chakrawarthy, M. Cromaz, P. Fallon, A. Hayes, H. Hua, S.D. Langdown, I.Y. Lee, C.J. Pearson, Zs. Podolyák, R.Teng and C. Wheldon, to be published in AIP conference proceedings (2003).
7. "High-spin states populated in deep-inelastic reactions"  
S. Mohammadi, Zs. Podolyák, G. de angelis, M. Axiotis, D. Bazzacco, P.G. Bizzeti, F. Brandolini, R. Broda, D. Bucurescu, E. Farnea, W. Gelletly, A.

## Appendix B. Publications

---

- Gadea, M. Ionescu-Bujor, A. Iordachescu, Th. Kröll, S.D. Langdown, S. Lunardi, N. Marginean, T. Martinez, N.H. Medina, B. Quintana, P.H. Regan, B. Rubio, C.A. Ur, **J.J. Valiente-Dobón**, P.M. Walker and Y.H. Zhang, to be published in the Brazilian J. of Phys. (2003).
8. "Structure of neutron-rich nuclei from deep-inelastic reactions"  
Zs. Podolyák, S. Mohammadi, G. de angelis, Y.H. Zhang, M. Axiotis, D. Bazzacco, P.G. Bizzeti, F. Brandolini, R. Broda, D. Bucurescu, E. Farnea, W. Gelletly, A. Gadea, M. Ionescu-Bujor, A. Iordachescu, Th. Kröll, S.D. Langdown, S. Lunardi, N. Marginean, T. Martinez, N.H. Medina, B. Quintana, P.H. Regan, B. Rubio, C.A. Ur, **J.J. Valiente-Dobón** and P.M. Walker, to be published in Int. J. Mod. Phys. E (2003).
9. "Digital Gamma-Ray Tracking Algorithms in Segmented Germanium Detectors"  
C. J. Pearson, **J.J. Valiente-Dobón**, P.H. Regan, P.J. Sellin, E. Morton, P.J. Nolan, A. Boston, M. Descovich, J. Thornill, J. Cresswell, I. Lazarus and J. Simpson, *IEEE Trans. on Nucl. Sci.*, Vol. 49, No. 3, 1209 (2002).
10. "Performance of a 6x6 segmented germanium detector for  $\gamma$ -ray tracking"  
**J.J. Valiente-Dobón**, C.J. Pearson, P.H. Regan, P.J. Sellin, W. Gelletly, E. Morton, A. Boston, M. Descovich, P.J. Nolan, J. Simpson, I. Lazarus and D. Warner, *Nucl. Instr. and Meth. A* **505**, 174 (2002).
11. "Isomer Spectroscopy in the Neutron-Deficient Lead Region Following Projectile Fragmentation"  
K.A. Gladnishki, Zs. Podolyák, J. Gerl, M. Hellström, Y. Kopatch,, S. Mandal, M. Górska, P.H. Regan, H.J. Wollersheim, A. Banu, G. Benzoni, H. Boardman, M. La Commara, J. Ekman, C. Fahlander, H. Geissel, H. Grawe, E. Kaza, A. Korgul, M. Matos, M.N. Mineva, R.D. Page, C.J. Pearson, C. Plettner, D. Rudolph, Ch. Scheidenberger, V. Shishkin, D. Sohler, K. Sümmeler, **J.J.**

## Appendix B. Publications

---

**Valiente-Dobón**, H. Weick and M. Winkler, *Acta Phys. Pol. B* **34**, 2395 (2002).

## Appendix C

### Oral and Poster Presentations

1. Poster presentation “Study of  $^{136}\text{Ba}$  via a DIC”,  
*Gordon Conference*  
Colby-Sawyer college, New London, NH, USA, June (2003).
  
2. Oral presentation “Study of  $^{136}\text{Ba}$  via a DIC”,  
*Nuclear Structure Physics Near the Coulomb Barrier: Into the 21<sup>st</sup> Century*  
University of Yale, New Haven, USA, June (2003).
  
3. Oral presentation “Reaction Mechanism in a DIC”,  
*IoP Nuclear Physics Conference*  
Glasgow, U.K., April (2003).
  
4. Poster presentation, “Looking for the neutron-rich nucleus  $^{196}\text{Os}$ ”,  
*Nuclear Structure Theory workshop*  
Surrey University, Guildford, U.K., January (2003).

## Appendix C. Oral and Poster Presentations

---

5. Oral presentation, "Performance of a  $6 \times 6$  segmented germanium detector for  $\gamma$ -ray tracking",  
*Symposium on Radiation Measurements and Applications*  
University of Michigan, Ann Arbor, Michigan, USA, May (2002).
  
6. Oral presentation, "Performance of a  $6 \times 6$  segmented germanium detector for  $\gamma$ -ray tracking",  
*IoP Nuclear Physics Conference*  
Brighton, U.K., January (2002).
  
7. Oral presentation, "First test of a  $6 \times 6$  segmented germanium detector for  $\gamma$ -ray tracking"  
*International Summer School on Nuclear Physics*  
University of Bangor, Wales, U.K., September (2001).
  
8. Oral presentation, "Gamma-ray tracking concept",  
*IoP Nuclear Physics Conference*  
University of Bergen, Bergen, Norway, January (2001).